Thermo-Fluid Modeling and Robust Control of Modern Optic Fiber Drawing Processes

A Dissertation
Presented to
The Academic Faculty

By

Zhiyong Wei

In Partial Fulfillment of the Requirements for the Degree of
Doctor of Philosophy in Mechanical Engineering

Georgia Institute of Technology
April 2004

Thermo-Fluid Modeling and Robust Control of Modern Optic Fiber Drawing Processes

Approved by:

Dr. Kok-Meng Lee

Dr. Andrei G. Fedorov

Dr. David G. Taylor

Dr. William E. Singhose

Dr. Zhi Zhou

April 9, 2004

DEDICATION

To my parents Qing-xiang Zeng and Ming-Shan Wei,

And

my wife Cen Shi.

ACKNOWLEDGEMENTS

I would like to express my deepest appreciation to all those who have supported and assisted this thesis research. First, I would like to especially thank my advisor Dr. Kok-Meng Lee for bringing me this research project. I would not have fulfilled the accomplishments without his valuable advices and constant encouragement. I would also like to thank my thesis reading committee, Drs. Fedorov, Singhose, Taylor, and Zhou, for reviewing my proposal and dissertation, and providing their constructive remarks. I am fully indebted to Dr. Zhou for numerous discussions on the formulation and applications of the research works. His industrial expertise has helped me get the most valuable results. I also appreciate Dr. Fedorov's help for the valuable discussions on the radiation model. His radiation heat transfer class was really inspiring.

This project (E25-A78) has been funded by the Bell Laboratories/Optic Fiber Solutions (OFS) of Lucent Technologies in Norcross, Georgia. The technical inputs offered by the staff of OFS/Lucent Technologies, particularly Dr. Siu-Ping Hong, have greatly enhanced my understanding of the fiber drawing process. I really appreciate his help. In addition, my thanks also go to Drs. Harry Garner, Mahmood Tabaddor, Junjun Wu, Shunhe Xiong and Mr. John Raynell for supplying the manufacturing process information and some of the measurement data, particularly during my internship at Bell Labs in the summer of 2001. I would also like to take this opportunity to thank Dr. Serge W. Tchikanda for his helpful discussions in the research and for sharing the initial code for the furnace draw simulations.

Thanks to my many friends and colleagues in and around Georgia Tech and the school of Mechanical Engineering. They are Xuecheng Yin, Debao Zhou, Bao Mi, Hai

Ding, Qiang Li, Jiantao Zhen, Shijiang He, Jeffry Joni, Kwaku Eason, and many more. Their support and friendship during my graduate studies were greatly appreciated.

I would like to express my deepest appreciation and gratitude to my parents Qing-Xiang Zeng and Ming-Shan Wei for their love and support over all these years. Thanks to my sister Zhi-Hong Wei, her husband Jie Li and their lovely son Yi-Zhou Li.

Finally, my special thanks go to my beautiful wife, Cen Shi. Her love, support and encouragement make my life in Atlanta enjoyable and warm. Her understanding of my day and night hard working during the difficult times of the research was really a great support. I believe I will develop a successful career with her constant support.

TABLE OF CONTENTS

LIST OF TABLES

LIST OF FIGURES

LIST OF SYMBOLS AND ABBREVIATIONS

Symbols

C_p	Specific heat
D_f	Fiber diameter
$E_{b\lambda}$	Spectral blackbody emissive power
$E_{b,p}$	Blackbody emissive power on the post-chamber wall
$\widetilde{E}_b$	Apparent blackbody emissive power
$F_{i\text{-}j}$	Diffuse view factor from element *i* to element *j*
F_t	Draw tension
G	Jacobian of the grid transformation
H_λ	Spectral irradiation
H_p	Irradiation on post-chamber inner wall
$\widetilde{H}$	Apparent irradiation
I_λ	Spectral radiative intensity
$I_{b\lambda}$	Spectral blackbody radiation intensity
J_λ	Spectral radiosity
L	$L_f + L_p$
L_f	Furnace length
L_p	Post-chamber length
N	Total number of snapshots
R	Glass radius
R_f	Furnace radius
R_p	Preform radius
R_{ope}	Iris opening radius
$R_{post,i}$, $R_{post,o}$	Post-chamber wall inner and outer radii
T	Temperature
T_a	Radially lumped air temperature in the chamber
T_g	Glass temperature along the free surface
T_∞	Ambient temperature
T_{fur}	Furnace wall temperature
T_{post}	Post-chamber wall temperature
$\overline{T}$	Radially lumped temperature; stead state temperature
U_z	Friction velocity used in the turbulence model
$\widetilde{U}$, $\widetilde{V}$	Contravariant velocities
V_n, V_t	Normal and tangential components of the velocity at the free surface
$\overline{a}$, $\overline{v}$, $\overline{T}$	Steady state values of *a, v, T*
a' , v' , T'	Relative perturbations of *a, v, T*
a	Glass cross sectional area, πR^2
g	Gravitational acceleration

g^{11}, g^{12}	Grid metric tensors
h	Convective heat transfer coefficient
h'	Relative perturbation of h
k	Thermal conductivity
$\widetilde{k}$	Apparent conductivity of glass
n	Magnitude of the normal vector
$\mathbf{n}$	Unit normal vector
n_λ	Spectral index of refraction
n_g	Average index of refraction of the glass
n_r, n_z	Radial and axial components of the normal vector
p	Pressure
$q''_{rad,opa}$	Net radiation heat flux in the opaque band
q''_{rad}	Net radiation heat flux at the glass surface
q''_{conv}	Air convective heat flux at the glass surface
$q_{rad,p}$	Radiative heat flux at the post-chamber inner wall
$q_{conv,p}$	Convective heat flux at the post-chamber inner wall
q_{loss}	Heat loss through the post-chamber insulator
q'	Perturbation of the irradiation
$q^+_{\lambda,r}$, $q^+_{\lambda,z}$	One-way spectral radiative fluxes in the positive r and z directions
$\mathbf{q}_R$	Radiation heat flux
$\mathbf{r}$	Position vector; radial vector
r, z	Radial and axial coordinates
$\mathbf{s}$	Orientation vector
$\widetilde{t}$	Fictitious time
u, v	Radial and axial components of velocity
u_o, u_i, u_q	Control inputs of winding motor, feeding mechanism and furnace
w_o, w_i, w_q	Disturbances in the winding motor, the feeding mechanism and the furnace
u_n	Snapshot
v	Axial component of velocity
v_p, v_f	Glass Feed rate and draw speed
v_o	Dimensionless draw speed
v'_i, v'_o	Dimensionless perturbation of glass feed rate and draw speed
x_a, x_v, x_T	Spectral coefficients for the linear mapping of a', v', T'
κ_λ	Spectral absorption coefficient
$\widetilde{\kappa}_R$	Apparent absorption coefficient
α, γ, β	Direction cosines of the intensity orientation vector $\mathbf{s}$
θ	Local polar angle
ε	Emissivity
ρ	Density

μ	Dynamic viscosity
Φ	Dissipation function
ζ	Surface tension
κ	Surface curvature
λ	Wavelength
η, ξ	General curvilinear coordinates
ψ	Local azimuthal angle
μ_T	Eddy viscosity
Γ	Diffusivity
σ_{zz}	Axial normal stress
δ	Boundary layer thickness
$\widetilde{\varepsilon}$	Apparent emissivity
ϕ	Empirical eigenfunction
$\rho_\lambda^+,\ \rho_\lambda^-$	Reflectivities at the outer and inner surfaces, respectively
$\tau_o,\ \tau_i,\ \tau_q$	Time constants of winding motor, feeding mechanism and furnace
$\eta_r, \eta_z, \xi_r, \xi_z$	Grid metrics of the general tranformation
σ	Stefan-Boltzmann constant
Ω	Solid angle

Abbreviations

1-D	One-dimensional
2-D	Two-dimensional
RTE	Radiative transfer equation
FVM	Finite volume method
ROM	Reduced order model
ACM	Artificial compressibility method
PISO	Pressure-implicit with splitting of operators
K-L	Karhunen-Loeve

SUMMARY

Computational thermo-fluid models of a free surface flow under the dominant radiative transfer have been developed for the design and control of a modern optic fiber drawing process. Although modeling of the fiber drawing process has been of interest for the past three decades, most of the previous studies were limited to low draw speeds and small preforms. Large preforms drawn at high speeds have been used in the state-of-the-art fiber drawing systems to improve production efficiency and reduce cost. Several assumptions commonly made in previous studies have to be relaxed to address the new challenges. In this study, instead of using the Rosseland approximation, the radiative transfer equation (RTE) was solved directly for the radiation fluxes using the finite volume method (FVM). The complete two-dimensional free surface flow was simulated along with the coupling of the radiative transfer. Unlike most of the previous studies that only considered the furnace domain and that arbitrarily assumed the glass velocity at the exit, we included the post-chamber in the computation domain and predicted the fiber solidification location. Furthermore, the mixed convection of the air in the post-chamber was also considered, and was shown to have significant effects on the fiber solidification.

On the basis of the computational model, a reduced order model (ROM) was developed for a mixed H∞/LQG controller designed to regulate the fiber diameter under the effects of disturbances. In contrast to the empirical lumped-parameter models often used in traditional control designs, the ROM has been derived from physical principles. Optimal numerical eigenfunctions were obtained through the Karhunen-Loeve expansion using the computational model. The Galerkin's method was then applied to obtain the state space ROM. The numerical model was shown to be efficient and was verified

experimentally. The ROM characterizes the dynamics of the system accurately as compared with the computational model. The simulations using the full computational model showed that the closed-loop system is robust and superior to the open-loop system in the regulation of fiber diameter.

The modeling and control methods can be applied to the design optimization and parameter regulation of the high-speed large-preform draw processes as well as other manufacturing processes that involve similar thermal-fluid transports.

CHAPTER I

INTRODUCTION

1.1 Motivations and Background

A broad range of new and traditional material processing has posted some unique challenges in improving product quality, reducing cost, and controlling material properties. Among the materials are semiconductor and optical materials, composites, ceramics, biomaterials, advanced polymers, and specialized alloys. Thermal-fluid transports play an important role in the quality and characteristics of the final products during the manufacturing processes. As direct measurement of the temperature/velocity fields and other critical distributed variables is often impossible under the harsh environment of the manufacturing systems, the design of the facilities and processes has been accomplished by extensive trial-and-error methods. The ability to predict the distributed variables offers a means to analyze the underlying physical characteristics, explain the experimental observations, and optimize the facility and process designs. Once verified, the numerical prediction of the distributed variables can be utilized in deriving reduced order models for control system design and optimization. The performance of the open-loop and/or close-loop systems under different designs and operating conditions can be easily evaluated using the experimentally verified numerical models. This methodology is cost-effective in the design of complex manufacturing systems where the prototyping cost is high and the direct measurement is extremely difficult.

One challenging problem among the above mentioned manufacturing processes is the modeling of the free surface flow under the dominant radiation transfer in the participating media. The viscosity of the material is sensitive to temperature changes, and may vary by several orders of magnitude during the process. The free surface has complex boundary conditions which may require the numerical solution of another fluid transport. Since several coupled transports are involved in the problem, a robust and efficient computation algorithm is needed to solve the problem. The computational model can be used in the process design and analysis, but is rather cumbersome for use in the controller design and implementation. A practical reduced-order model that captures the essential characteristics of the system is in need when the system needs an optimal controller to regulate critical parameters. The challenge of the reduced order modeling of this kind of systems lies in the fact that the system involves a number of distributed state variables and the variables are coupled with each other.

One typical example of the above mentioned system is the optic fiber drawing process. The manufacturing of optic fibers has already had a history of more than 3 decades. To meet the growing demands in city-to-city, metropolitan, and the direct-fiber or last-mile access networking applications, fiber manufacturers (competing for the lucrative market shares) are seeking methods to draw fibers at high speeds from large preforms (glass rods) in order to improve production efficiency, fiber quality, and save manufacturing cost. The design of these modern fiber drawing systems need a high fidelity model to predict variable distributions, and a reduced order model for the controller design for the regulation of critical parameters. The design methodology and the numerical modeling method developed in this research are directly applied to the

modern fiber drawing system, and also can be used for the design of other manufacturing processes that involve similar complex thermal-fluid transports.

Figure 1-1 shows the schematic of a typical fiber draw tower. The tower usually includes three sequential sections: heating and cooling, coating and curing, and winding. Optical fibers are usually manufactured from fused silica glass rods of one or more meters long and several centimeters in diameter, which are called preforms in industry. In the first section, the preform is slowly moved into a cylindrical furnace and heated above the glass melting temperature. Fiber is steadily drawn from the preform at the bottom of the furnace by a high tension force at a draw speed in the order of 10m/s. The fiber is cooled down to the ambient temperature by moving through the ambient air or specially designed cooling tube. In the second section, the fiber is coated with an organic material and cured in the UV ovens. The last section is at the end of the tower, the coated fiber is wound on spools through a precision winding mechanism.

The most critical part of the drawing process is at the first section where a post-chamber is usually added at the bottom of the furnace as shown in Figure 1-2. The success of a stable high speed drawing depends on the design of the furnace/post-chamber. The optical quality of the fiber and the uniformity of the fiber diameter are directly affected by the thermal-fluid transport in this section. Hence, this study concentrates on the modeling in the furnace/post-chamber domain.

The furnace uses induction heating and maintains a temperature above the glass melting point (about 1853K for fused silica). Under the dominant radiation heat transfer, the preform becomes soft and melts to form a neck-down profile. Unlike the conventional furnace draw process, the diameter of the melting glass at the exit of the

furnace is usually still larger than that of the fiber. Since the glass must be cooled gradually before the solidification to reduce optical losses in the final product, the post-chamber is insulated so that the air inside the chamber has a relative higher temperature than the ambient and the glass cooling rate is reduced. There is a small opening at the bottom of the post-chamber for the passing of fiber. Driven by buoyancy force, the ambient air may enter the chamber through the iris opening and exit the furnace at the top ring opening. The speed of the glass flow in most part of the post-chamber increases drastically (as high as 50 times) from the glass speed at the furnace exit. A boundary layer of air starts to develop along the continuously moving glass cylinder. Since the fiber diameter is only 125μm, the glass diameter convergence usually takes a long distance, and the post-chamber is usually much longer than the furnace in the modern fiber draw system.

The modeling works at Georgia Tech is in collaboration with OFS/Lucent Technologies at Norcross, Georgia, which has the second largest optical fiber manufacturing facilities in the world. Lee and Zhou (1997) initiated the research as an optimal control problem. The objective was to apply multi-input-multi-output (MIMO) control strategy to ease the burden of a single control variable in the regulation of fiber diameter and tension. Tchikanda (2001) extended the problem into the computational modeling of the drawing process. He formulated the thermal-fluid transports in the furnace in a two-dimensional (2-D) axisymmetric framework, and then discretized the governing equations in a curvilinear coordinate system and obtained the preliminary numerical solutions. Finally, he developed a state space control model by linearizing a discretized quasi one-dimensional (1-D) thermal-fluid model using the finite difference

method. The linearization was around the steady state solution of the 2-D numerical model.

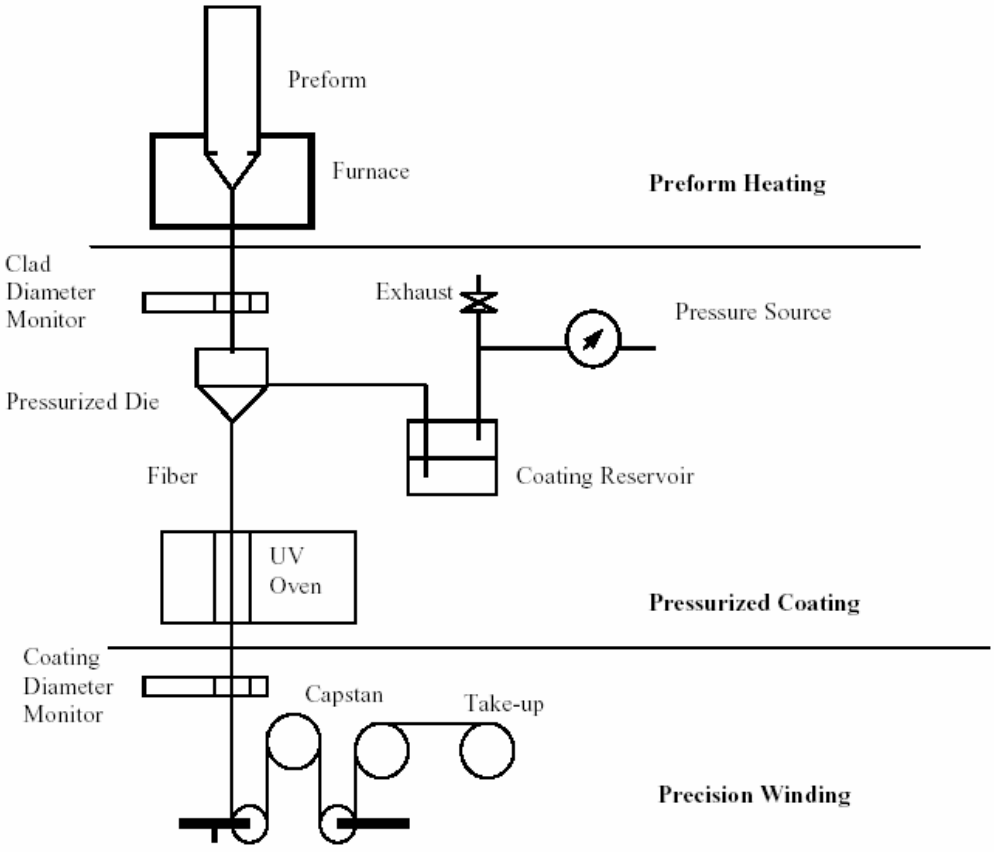

Figure 1-1 Schematic of typical fiber draw tower. Reprinted from Lee and Zhou (1997)

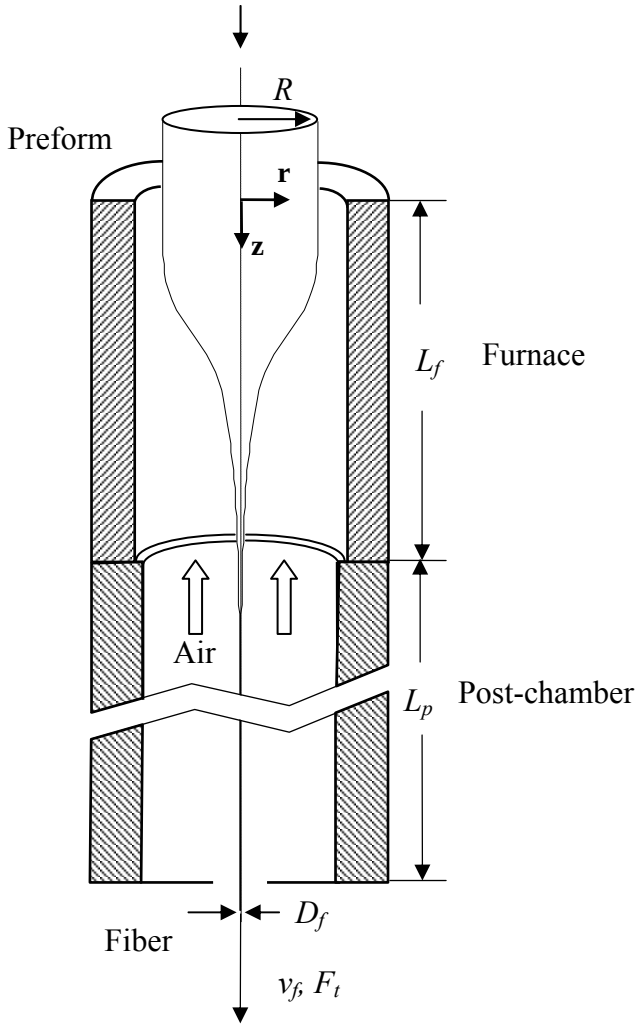

Figure 1-2 Schematic of fiber drawing in furnace and post-chamber

1.2 Problem Description and Objectives

As the second effort in Georgia Tech on the study of the fiber drawing process, this research focuses on improving the modeling and control of the thermal fluid transports in the system as shown in Figure 1-2. Both the glass diameter and the velocity undergo large variations by several orders of magnitude. The highly viscous free surface flow forms a neck-down profile in the furnace. Since the viscosity of the fused silica is

close to an exponential function of temperature, the viscous flow is strongly coupled with the thermal transport within the glass.

The glass temperature distribution in the furnace is governed by the radiation heat transfer. The dominant heating source of the glass is the radiation emission from the furnace wall at a high temperature. The accurate solution of the glass temperature field depends on the reliable radiative transfer computation. The radiation heat flux from the furnace is partly absorbed and reflected at the glass surface, while most part of the radiative flux is transferred through the semitransparent glass media. Volumetric absorption and emission exist throughout the glass domain. There are a number of challenges in the computation of the radiative transfer:

- The radiation intensity is not only wavelength dependent, but also depends on the location and the orientation variables.
- The boundary condition at the glass free surface is complicated since the surface irradiations can not be directly obtained.
- The view factor is difficult to calculate due to the arbitrary geometry.

The convective heat flux from the air around the glass surface is negligible in the furnace domain, but is significant in the post-chamber due to the high surface area to volume ratio and the high moving speed of the glass. Hence, the glass temperature distribution in the post-chamber is governed by the mixed convection of the air, which involves the boundary layer flow around continuously moving fiber and the natural convection in the open-ended chamber. The challenge in the numerical simulation of the mixed convection is that most part of the boundary layer flow in the post-chamber is

around a high speed moving glass with a diameter of much less than 1mm. The buoyancy force and the drag force are in the opposite direction. There exist sharp temperature and velocity gradients within the boundary layer.

Diameter uniformity of the fiber is one of the most important quality factors. The uniformity affects the joint and splice loss, optical transmission characteristics, and the refractive index profile. During the drawing process, the fiber diameter may undergo significant fluctuation due to different sources of disturbances:

- air convection fluctuation,
- furnace heat flux disturbance,
- winding motor vibration, and
- preform diameter variation.

Feedback control is usually used to compensate the effects of the disturbances and reduce the fluctuation of the fiber diameter. Most control systems currently in use are not based on physical models. The tuning of the controller structure and gains has to rely on the extensive experiments. The controllers designed in this way are less than optimal due to difficulties in making practical measurements in the furnace domain. As the fiber drawing process upgrades at a fast pace in the industry, an optimal control design based on a low order physical model has a more general application and is able to reach the same objective with smaller control effort. A reduced order model, which has a well balance between the accuracy and the computation efficiency, is required to reach the goal.

In order to address the above mentioned challenges, we set up the following objectives in this research:

(1) Develop high fidelity computational models to simulate the radiative transfer and the free surface flow in the glass domain and the mixed convection in the air domain. The modern fiber drawing process is considered in the modeling and simulations.

(2) Develop a reduced order model which characterizes the dominant dynamics of the thermal-fluid system with a minimum number of lumped state variables.

(3) Develop a robust, optimal controller to regulate the fiber diameter subject to the disturbances.

1.3 Literature Review

In the following review, prior works on simulation and control design of fiber drawing systems are discussed first, and then the recently developed techniques which can be used to improve the prior works are presented.

1.3.1 Numerical Modeling

Modeling of the fiber drawing process has been of interest for the past two decades. During the late 1970's and the 1980's, various aspects of the optical fiber draw problems were studied by a number of researchers. Among these, Paek and Runk (1978) investigated experimentally and numerically the physical behavior during the furnace fiber drawing. Using a simple radiation model and assuming a smooth changing heat transfer coefficient and surface emissivity, they obtained an approximation of the necking shape. Myers (1989) proposed a more realistic calculation of the surface radiation exchange. He neglected the advection and the gravity terms in the momentum equation, and the conduction, the radiative transfer and the surface convective heat transfer in the

energy equation. Other examples include Homsy and Walker (1979), and Vasiljev *et al.* (1989). Since the early fiber manufacturing used small preforms (diameters 1~2cm) and low draw speed (around 1m/s), one-dimensional (1-D) models were usually used in the early studies.

Two-dimensional (2-D) models have been used in more recent studies. Among these, Lee and Jaluria (1997) and Choudhury and Jaluria (1998) assumed a free surface profile in the calculation to solve for the velocity and temperature field. Based on the radially lumped axial velocity and the axial force balance, Choudhury et al. (1999) obtained a correction scheme to generate the neck-down profile while solving the 2-D heat transfer and fluid flow. Small-diameter (about 2cm) preforms drawn at a relatively slow speed of 3 m/s was considered in their simulations. Xiao and Kaminski (1997) solved the two-dimensional conjugate problem of the glass and gas flow with free interface using commercial finite element code FIDAP. They studied a 5cm diameter preform and it was shown that the glass velocity distribution is close to 1-D while the glass temperature has a 2-D distribution. They found difficulties to obtain the convergence (that is sensitive to the deformation mesh) as the number of radiative macro surfaces increases. More recently, Yin and Jaluria (2000) and Cheng and Jaluria (2002) investigated the effects of process parameters on high-speed fiber drawing (up to 20m/s). However, both these studies assumed that the glass was drawn into the specified fiber diameter of 125μm at the furnace exit as in most of the previous studies. Their results, however, show that the computed glass temperatures were well above the glass melting point at the furnace exit. This may imply that the glass cools to form solid fiber after leaving the furnace and thus, the actual diameter (and hence the speed) of the glass at the

furnace exit are essentially unknown. Tchikanda (2001) solved the 2-D thermo-fluid problem for large preforms and high draw speeds. He used artificial compressibility method (ACM) to solve the governing equations for the glass flow using primitive variables, while used the vorticity and stream functions for solving the gas flow.

Radiation transfer is the dominant mode of heat transfer in the fiber draw process. The simplest approach, perhaps, has been to assume the participating medium is optically thick (or commonly known as the Rosseland's approximation) such that the radiative energy contributions from the boundary and the far away portions of the medium can be neglected. Rosseland's optically thick approximation reduces the total radiative flux to a simple temperature diffusion term; an effective radiative conductivity can then be used. Most of the previous studies on the modeling of optic fiber drawing have used this approach to reduce the overall problem to a more tractable form. Homsy and Walker (1979) found that the Rosseland's assumption would fail at the surface, but no method was suggested to correct for the errors. An alternative approach is to solve the radiative transfer and the energy equations simultaneously using numerical methods. Lee and Viskanta (1999) investigated combined conduction and radiation in a one-dimensional glass layer. By comparing the discrete ordinate method and the Rosseland approximation method, Lee and Viskanta (1999) concluded that the diffusion approximation greatly underpredicts the temperature and heat flux when the thickness or the opacity of the layer is small. In a different study, Yin and Jaluria (1997) employed a zonal method to investigate the radiative exchange within the neck-down profile of a glass preform for an assumed radial temperature profile. Their simulation results suggested that Rosseland's

approximation underestimates the heat flux only when the radial temperature variation within the preform is substantial as compared with the zonal method.

Recently, the finite volume method (FVM) has been used in modeling semitransparent, emitting and absorbing medium. The method has a flexibility to lay out the spatial and angular grids and can solve the radiative transfer equation (RTE) numerically without any assumption. Chai, *et al.* (1994) presented the procedure of the FVM and tested the method with benchmark problems of two- and three-dimensional enclosures with participating media. The results demonstrated that the method is accurate and efficient when compared with the exact solution or discrete ordinates method (DOM). Liu, *et al.* (1997) compared the FVM and the DOM on benchmark problems in body-fitted coordinates of Cartesian geometry. Their results from both methods show reasonably good agreements and in some cases, the FVM outperforms the DOM. Baek and Kim (1997) presented the FVM in an axisymmetric cylindrical geometry and obtained accurate solution for benchmark problems. Most of the studies in these problems have relatively simple boundary conditions, either a bounding opaque wall or an environment with a uniform temperature.

The solution to the radiative transfer equation requires an appropriate model to describe the spectral absorption coefficient of the glass medium. Myers (1989) introduced a two-step band model to describe the spectral absorption coefficients of a fused silica glass, which has been commonly used in the prediction of radiative transfer in optical fiber drawing processes. Myers' band model neglects the absorption at short wavelengths ($\lambda<3.0\mu m$), which has a relatively small value about 0.001~0.3 cm^{-1} for semitransparent glasses. However, the spectral intensity of a blackbody radiation given

by Planck's function (see for example Modest, 1993) suggests that more than 60% of radiative energy concentrates in the band $0.2\mu m \le \lambda < 2.8\mu m$ near the melting temperature range of glass (1500K~2500K). The effects of radiation absorption could be considerable in this short-wavelength band, although the absorption coefficient is small. Since the values for the spectral absorption coefficient of fused-silica glass at temperatures near the softening point were not known, Myers' two-step band model has been based on data taken at room temperature. Recent experiments (Endrys 1999; Nijnatten, *et al.,* 1999) on typical glasses suggested that the absorption coefficient in the $2.8\mu m \le \lambda < 4.8\mu m$ band near the melting temperature is generally 10~25% lower than that at a room temperature of 25°C.

1.3.2 Reduced Order Modeling and Control Design

Motivated by the need to improve product quality and process yield, numerous investigations have been taken on the diameter control of the fiber drawing process. From the late 1960's to the early 1980's, significant efforts were directed towards the stability study of fiber drawing process. Most of the studies were for textile fibers and assumed an isothermal model (for example, Matovich and Pearson, 1969; Donnelly and Weinberger, 1975; and Schultz *et al.*, 1984). The studies usually showed that the open-loop system become unstable when the ratio of the draw speed to the feed rate exceeds some critical value. In contrast to these results, Pearson *et al.* (1976) and Mhaskar and Shah (1977) showed that the process is unconditional stable for Newtonian material when the fibers freeze before reaching the windup spool. In a later study that also considered the energy equation, Geyling and Homsy (1980) showed that the system stability depends

on the draw ratio, the convective cooling coefficient and the apparent radiative cooling coefficient.

Most of the previous control designs for fiber drawing systems were based on empirical lumped parameter models that were less than optimal due to difficulties in making practical measurements in the furnace domain. Nakahara, *et al.* (1978) studied the effects of different thermal and mechanical drawing conditions on the quality and tensile strength of the fibers. They concluded that temperature variation in the furnace is the major factor affecting the high frequency fiber diameter fluctuations, and that low frequency fluctuations are caused by longitudinal variations in the preform diameter. They suggested a feedback control of drawing speed to reduce low frequency diameter variations. Smithgall (1979) reduced the standard deviation of fiber diameter from 0.8μm down to 0.3μm by using optimal control of drawing speed for a nominal speed of 1m/s. Imoto, *et al.* (1989) used control of both gas flow and drawing speed to reduce diameter variation of the fiber. Faster fluctuations in diameter are suppressed by adjusting the gas flow rate, and slower ones are controlled by changing the drawing speed. Using a distributed system model, Mulpur and Thompson (1993) utilized a modified modal control strategy to stabilize the closed-loop system under high draw ratio. In a later research (Mulpur and Thompson, 1996), they applied model reference control (MRC) and quasi-nonlinear control (QNC) technique on the diameter control. Since they still assumed an isothermal model that showed the open-loop system was unstable when the draw ratio exceeded some critical value, their control objective was to stabilize the process.

In order to improve manufacturing efficiency and save costs, much larger preforms and higher draw speeds have been used in the state-of-the-art fiber drawing systems. This imposes a challenge that the draw ratio is up to two orders of magnitude higher than that considered in the previous studies. Furthermore, the glass undergoes large temperature variations inside the furnace and the post-chamber, which consequently affects the glass velocity and diameter through strongly temperature dependent viscosity. Hence, the isothermal assumption is no longer valid for these systems. In order to develop a general method of control design for the systems, a reduced order model based on rigorous physical principles should be used. The reduced order model is required to catch the dominant dynamics of the transports with the minimum order.

Fiber drawing process is described by nonlinear parabolic PDE's which include convection and diffusion terms. Tchikanda and Lee (2002) developed a linear state-space model for the draw process, by discretizing a quasi 1-D CFD model using the finite-difference method resulting in a high fidelity model (147-order). The main feature of parabolic PDE's is that their dominant dynamic behavior is usually characterized by a finite (typically small) number of degrees of freedom (Temam, 1988). This implies that the dominant dynamic behavior of such systems can be approximately described by finite-dimensional ODE's. The Karhunen-Loeve (K-L) expansion (Loeve, 1955; Sirovich, 1987) followed by the Galerkin's procedure has been shown to be a promising method to obtain an accurate ODE model with the minimum order. In this method, detailed transient simulations of PDE system are carried out to obtain a set of empirical eigenfunctions corresponding to the most dominant eigenmodes of the system through the K-L expansion. The empirical eigenfunctions are then used as the basis functions in

the Galerkin's procedure to obtain the reduced order ODE's. As the eigenfunctions represent the dominant physical characteristics of the system, the resulted ODE's have the minimum order for the required accuracy (Sirovich and Park, 1990). This reduced order modeling method has been demonstrated by a number of researchers in thermal-fluid systems (for example, Park and Cho, 1996; Banerjee, *et al.*, 1998; Theodoropoulou, *et al.*, 1998; and Park and Lee, 2000). However, most of them only dealt with single distributed state variable systems.

1.4 Summary of Results

The contributions made in this dissertation are briefly summarized as follows:

(1) Two numerical models have been developed for predicting the free surface flow coupled with the radiation transfer in the modern optic fiber drawing process, where large preforms and high draw speeds have been used. The first is a complete 2-D model for the furnace domain. The second is a semi 2-D model for both the furnace and post-chamber domain. Robust and efficient computation schemes are also developed to solve the nonlinear governing equations. The numerical method is shown to be superior to the previous ones in terms of the grid number, the computational cost, and the simulation parameters.

(2) Unlike most of the previous studies which only consider the furnace domain, we do not assume the glass diameter or speed at the exit of the furnace and consider both the furnace and the post-chamber in solving the conjugate problem. The problem considered here involves temperature coupled free surface glass flow and the mixed convection of the air. Due to large temperature variations and the high

draw speed, we account for the temperature dependency of the air properties and the turbulence effect in the boundary layer flow around the continuously moving fiber. The free surface profile of the glass and the glass solidification location are predicted in the simulations, which has not been studied by the previous researchers.

(3) Instead of using the Rosseland's approximation that was taken in the previous studies, we solve the RTE directly using the FVM for the radiation intensities in the simulation of the modern fiber drawing process. The solution does not assume that the glass is optically thick or neglects the glass absorption at the short-wavelength band. Furthermore, unlike prior works by others (Jamaluddin and Smith, 1988; Lee and Viskanta, 1997), which used grid face areas in the discretized RTE in orthogonal cylindrical coordinates system, we present the fully conservative form of the 2-D RTE in both curvilinear and cylindrical coordinates systems so that the numerical scheme can be used for arbitrary axisymmetric cylindrical geometries.

(4) We extend the application of the pressure-implicit with splitting of operators (PISO) algorithm that was developed by Issa (1985) to the solution of Navier-Stokes equations in a curvilinear coordinate system and on a staggered grid. We develop a 9-grid-point pressure correction equation and obtain stable solutions. Few similar solutions have been demonstrated in the literature.

(5) Unlike previous studies (Paek and Runk, 1978; Choudhury, et al., 1999) where comparisons were made against experimental data obtained for a small-diameter preform (1 cm) drawn at a slow speed (1 m/s), we compare our prediction

against experimentally measured neck-down profile drawn at 25 m/s. The post-chamber wall temperature and fiber temperature are also measured for verifying the calculation.

(6) This research presents a method to apply the K-L expansion with the Galerkin scheme in the reduced order modeling of multi-variable distributed systems with nonlinear and coupled dynamics such as the fiber drawing process. This extends the previous works on the application of the K-L expansion on single variable systems.

(7) We extend the previous works on the feedback control design of the fiber drawing system using an isothermal model. Mixed robust (H∞)/optimal (LQG) controller is designed on the basis of the reduced order model which considers the coupling between the thermal and fluid transports. The close-loop control is demonstrated to be robust and superior to the open-loop system.

(8) The different levels of models presented in this study can be applied to the design optimization and control of the high-speed draw process with large diameter preforms as well as other manufacturing processes that involve similar thermal-fluid transports.

1.5 Organization of This Dissertation

The remainder of this dissertation is organized as follows. Chapter II presents the models of the radiation transfer in the glass media and the radiation exchange in the furnace chamber. The finite-volume method (FVM) is then applied to solve the radiative transfer equation (RTE) which is put in a general curvilinear form. The 2-D fluid and

energy equations along with the boundary conditions for both the glass and the air domains are presented in Chapter III. The equations are discretized on staggered grids and the suitable numerical schemes are applied to solve the equations. A semi 2-D model is also developed for the efficient steady state free surface computation. Chapter IV presents the reduced order modeling and robust control design. A quasi 1-D fluid dynamic model is presented first. The PDE model is linearized around the steady state solution obtained from the 2-D model developed in the previous chapters. The K-L expansion followed by the Galerkin's procedure is then used to obtain the reduced order state space control model. Finally, a mixed H_∞/LQG controller is designed for the regulation of the fiber diameter and tension force. The results of this research are presented in Chapter V. The numerical models are validated by experimental methods first. The 2-D numerical solutions of the temperature and velocity fields are then presented and analyzed. The semi 2-D model is validated by comparing with the complete 2-D model, and is used to predict the fiber solidification location in the post-chamber. Finally, the reduced order model is compared with the CFD model, and the close-loop system performance is evaluated using the verified semi 2-D CFD model. The conclusions of this research and the recommendations for the future works are provided in the last chapter.

CHAPTER II

MODELING AND SOLUTION OF RADIATION TRANSFER

2.1 Overview

Radiation transfer is the dominant mode of heat transfer in the fiber draw process since the furnace temperature is as high as 2400K. As the melting glass flow is strongly coupled with the temperature field through the temperature dependent viscosity, accurate computation of radiation transfer within the glass is critical to the prediction of the glass temperature, velocity and the free surface profile. In this chapter, we present the radiative transfer equation (RTE) along with the boundary conditions. The RTE is solved using the computational strategy – finite volume method (FVM). An enclosure analysis for obtaining the surface radiation intensities and the numerical method for calculating the view factors are also presented.

2.2 Radiation Model

The following assumptions are made in solving the radiative transfer problem in the fiber drawing process:

(1) The glass is semitransparent to radiation in the spectral range $0 < \lambda < 5\mu m$ and is almost opaque beyond $5\mu m$. The scattering of radiation in glass can be neglected (Viskanta, 1975).

(2) An average value of the refractive index of the glass is used and its variation in the temperature range considered in our study is neglected.

(3) The furnace walls are gray and diffuse.

(4) The inner and outer surfaces at the glass interface are treated as diffuse for the radiation reflection and transmission. This assumption is based on the fact that the surface of the melting preform may undergo wavy hydrodynamic instabilities with the magnitude in the order of radiation wavelengths.

The radiative transfer in a spectrally absorbing-emitting medium is modeled using the following RTE:

$$\mathbf{s}\cdot\nabla I_\lambda(\mathbf{r},\mathbf{s}) = \kappa_\lambda\left[n_\lambda^2 I_{b\lambda}(T) - I_\lambda(\mathbf{r},\mathbf{s})\right] \tag{2-1}$$

where the spectral radiative intensity $I_\lambda(\mathbf{r},\mathbf{s})$ is a function of the position vector $\mathbf{r}$, orientation vector $\mathbf{s}$, and wavelength λ; $I_{b\lambda}(T)$ is the spectral intensity of a blackbody radiation given by Planck's function; κ_λ is the spectral absorption coefficient; and n_λ is the spectral index of refraction.

The divergence of the radiation heat flux can be obtained by integrating Equation (2-1) over the whole solid angle ($\Omega = 4\pi$) and over the whole spectra, which yields

$$\nabla\cdot\mathbf{q}_R = \int_0^\infty\left[4\pi\kappa_\lambda n_\lambda^2 I_{b\lambda}(T) - \kappa_\lambda\int_{\Omega=4\pi} I_\lambda(\mathbf{r},\mathbf{s})d\Omega\right]d\lambda \tag{2-2}$$

By solving the RTE for $I_\lambda(\mathbf{r},\mathbf{s})$ and calculating $I_{b\lambda}(T)$ for a given temperature field, $\nabla\cdot q_R$ is readily calculated using the above equation. The spectral radiative heat flux on any surface can be calculated from

$$\mathbf{q}_\lambda = \int_{\Omega=4\pi} I_\lambda(\mathbf{r},\mathbf{s})\mathbf{n}\cdot\mathbf{s}d\Omega \tag{2-3}$$

where **n** is the normal vector of the surface. The corresponding total radiative heat flux is then given by

$$\mathbf{q} = \int_0^\infty \mathbf{q}_\lambda d\lambda \tag{2-4}$$

The radiative transfer is axisymmetric in the cylindrical coordinate system. In the local orientation and global spatial coordinate systems as shown in Figure 2-1, the RTE can be written in the following form:

$$\frac{\alpha}{r}\frac{\partial(rI_\lambda)}{\partial r} - \frac{1}{r}\frac{\partial(\gamma I_\lambda)}{\partial \psi} + \beta\frac{\partial I_\lambda}{\partial z} = \kappa_\lambda\left[n_\lambda^2 I_{b\lambda}(T) - I_\lambda\right] \tag{2-5}$$

where α, γ and β are the direction cosines of **s** as shown in Figure 2-1; and

$$\alpha = \sin\theta\cos\psi \tag{2-6}$$

$$\gamma = \sin\theta\sin\psi \tag{2-7}$$

$$\beta = \cos\theta \tag{2-8}$$

Since the glass free surface has an arbitrary neck-down shape where the radius varies dramatically along the axial direction, the RTE given by Equation (2-5) is transformed in a curvilinear coordinate system (η, ξ) where the free surface is along a line of constant η value. The following equation is obtained:

$$\frac{\partial\left[rG(\alpha\eta_r + \beta\eta_z)I_\lambda\right]}{\partial\eta} + \frac{\partial\left[rG(\alpha\xi_r + \beta\xi_z)I_\lambda\right]}{\partial\xi} - G\frac{\partial(\gamma I_\lambda)}{\partial\psi} = \kappa_\lambda rG\left[n_\lambda^2 I_{b\lambda}(T) - I_\lambda\right] \tag{2-9}$$

where (η_r, η_z) and (ξ_r, ξ_z) are the grid metrics that are first derivatives of η and ξ in terms of r and z; and G is the *Jacobian* of the transformation that is given by

$$G = \frac{\partial(\eta, \xi)}{\partial(r, z)} = \begin{vmatrix} \eta_r & \eta_z \\ \xi_r & \xi_z \end{vmatrix} \tag{2-10}$$

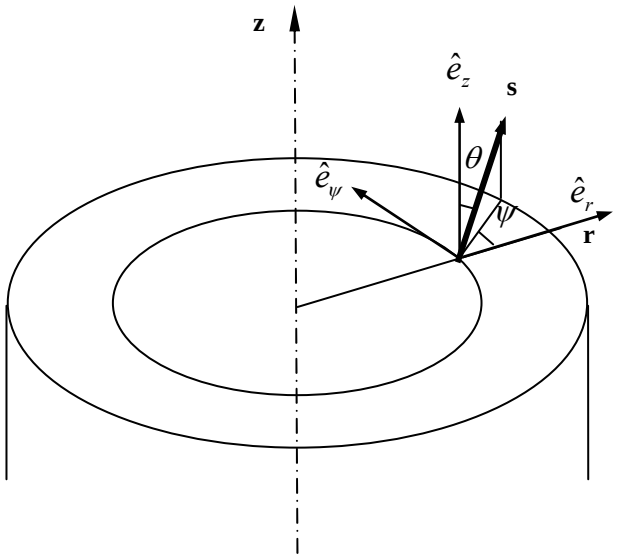

Figure 2-1 Local orientation vector in the axisymmetric cylindrical coordinates system

2.3 Boundary Conditions and Enclosure Analysis

The solution of the RTE requires the information of intensities along all the bounding interfaces of the glass media. Since the free surface is not bounded by an opaque wall, the incident intensities are from all the furnace walls and other surfaces that the glass can "see". The intensities should be determined from an enclosure analysis where the radiosities in the enclosure formed by the free interface, furnace and post-chamber walls, and the openings are calculated. The radiative transfer in the glass and the enclosure analysis are coupled by the intensities along the free interface.

2.3.1 Symmetry of the Glass

Along the axis of the glass cylinder, the following boundary condition is given due to the symmetry of the glass as shown in Figure 2-2:

$$\text{at } r = 0 \qquad I_\lambda = I_\lambda^{'} \quad \text{for } \beta = \beta^{'},\ \alpha = -\alpha^{'} \tag{2-11}$$

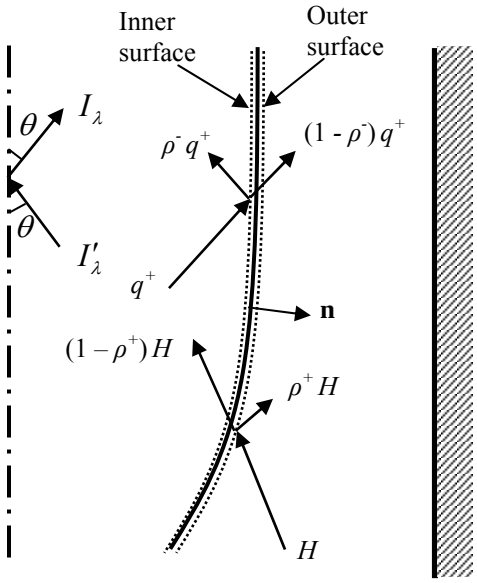

Figure 2-2 Radiation boundary conditions along the centerline and the free surface in the semitransparent band ($0 < \lambda < 5\mu m$)

2.3.2 Top and Bottom Boundaries

Since the temperature of the glass and the ambient environment outside the furnace is much lower than those within the furnace, we can neglect the intensities whose sources are from the outside of the furnace and the post-chamber. Hence,

$$\text{at } z = 0 \qquad I_\lambda \approx 0 \quad \text{for} \quad \beta > 0 \tag{2-12}$$

at $z = L_f + L_p$ $\qquad I_\lambda \approx 0$ for $\beta < 0$ (2-13)

2.3.3 Free Interface Boundary

As shown in Figure 2-2, for a diffuse interface, the radiation intensity at the inner glass surface pointing inward consists two parts:

at $r = R(z)$, $\mathbf{s}\cdot\mathbf{n} < 0$, and $0 < \lambda < 5\mu m$

$$I_\lambda(\mathbf{r},\mathbf{s}) = \frac{\left(1-\rho_\lambda^+\right)H_\lambda + \rho_\lambda^-\left(q_{\lambda,r}^+\mathbf{r} + q_{\lambda,z}^+\mathbf{z}\right)\cdot\mathbf{n}}{\pi} \tag{2-14}$$

where ρ_λ^+ and ρ_λ^- are the reflectivities at the outer and inner surfaces, respectively; $q_{\lambda,r}^+$, $q_{\lambda,z}^+$ are the one-way spectral fluxes in the glass in the positive r and z directions, respectively; $\mathbf{n}$ is the unit normal vector at the free interface pointing outward; and H_λ is the irradiation on the outer surface.

2.3.4 Enclosure Analysis

In order to obtain the irradiation H_λ required by Equation (2-14), the radiosities of the furnace and post-chamber walls must be determined. For this, we consider the enclosure formed by the glass outer surface, the furnace and post-chamber walls and the top and the bottom disk openings. As shown in Figure 2-2, the radiosities on the glass outer surface in the semitransparent band are given by

at $r = R(z)$, $\mathbf{s}\cdot\mathbf{n} > 0$, and $0 < \lambda < 5\mu m$

$$J_\lambda = \left(1-\rho_\lambda^-\right)\left(q_{\lambda,r}^+\mathbf{r} + q_{\lambda,z}^+\mathbf{z}\right)\cdot\mathbf{n} + \rho_\lambda^+ H_\lambda \tag{2-15}$$

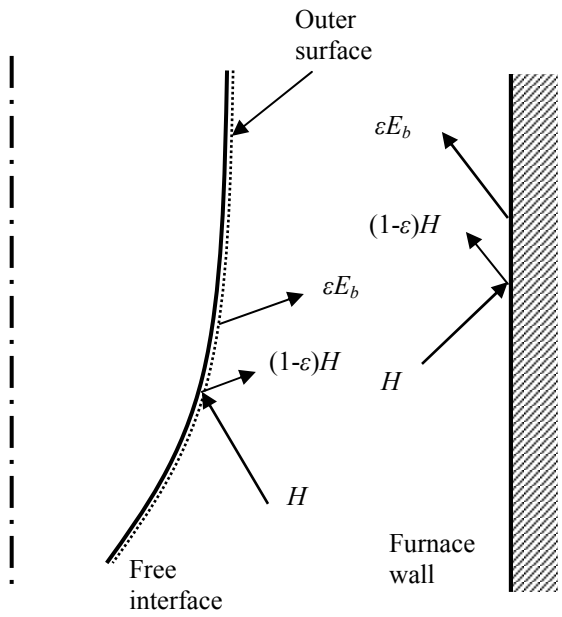

Figure 2-3 Surface radiation exchange in the opaque band ($\lambda > 5\mu m$)

As shown in Figure 2-3, the radiosities on the glass outer surface and the furnace wall in the opaque band are given by

(a) at $r = R(z)$, $\mathbf{s} \cdot \mathbf{n} > 0$, and $\lambda > 5\mu m$;
(b) at $r = R_f$, and $0 < \lambda < \infty$

$$J_\lambda = \varepsilon E_{b\lambda} + (1-\varepsilon) H_\lambda \tag{2-16}$$

where ε is the emissivity of the surface; and $E_{b\lambda}$ is the blackbody emissive power.

The temperature of the furnace wall is determined experimentally by a thermometer. The method is presented in detail in Appendix A. The furnace blackbody emissive power $E_{b\lambda}$ can be obtained using the Planck's function.

Since the view of the thermometer cannot reach further beyond the furnace, the temperature distribution of the post-chamber T_p(z) is calculated by balancing the heat flux at the inner wall:

$$q_{rad,p} + q_{conv,p} + q_{loss} = 0 \tag{2-17}$$

where the radiative heat flux $q_{rad,p}$, the air convective heat flux at the inner wall $q_{conv,p}$, and the heat flux lost through the insulating wall q_{loss} are given by

$$q_{rad,p} = \varepsilon_p \left[E_{b,p}(T_p) - H_p \right] \tag{2-18}$$

$$q_{conv,p} = k_a \left. \frac{\partial T_a}{\partial r} \right|_{r=R_{post,i}} \tag{2-19}$$

$$q_{loss} = \frac{T_p - T_\infty}{\frac{R_{post,i}}{k_{wall}} \ln\left(\frac{R_{post,o}}{R_{post,i}} \right) + \frac{R_{post,i}}{R_{post,o} h_o}} \tag{2-20}$$

where $R_{post,i}$ and $R_{post,o}$ are the post-chamber wall inner and outer radii, respectively; ε_p, $E_{b,p}$ and H_p are the emissivity, block-body emissive power and irradiation at the post-chamber inner wall, respectively; k_a and T_a are the thermal conductivity and temperature of the air inside the post-chamber, respectively; k_{wall} is the average thermal conductivity of the insulation layer; T_∞ is the ambient air temperature; and h_o is the average heat transfer coefficient at the post-chamber outer wall. It can be derived that the radiosity on an opaque surface can be given by

$$J_\lambda = E_{b\lambda} - \left(\frac{1}{\varepsilon} - 1 \right) q_{rad,\lambda} \tag{2-21}$$

where $q_{rad,\lambda}$ is the spectral radiative heat flux at the surface. Combining Equation (2-17) with the above equation, we obtain the radiosity at the post-chamber wall:

$$J_\lambda = E_{b\lambda} + \left(\frac{1}{\varepsilon_p} - 1\right)\left(q_{conv,p} + q_{loss}\right)a \tag{2-22}$$

where a is the fraction of the total radiative flux at each wavelength band.

The enclosure is divided into K small ring elements, and thus the irradiations can be expressed as

$$H_{\lambda,i} = \sum_{j=1}^{K} J_{\lambda,j} F_{i-j} \tag{2-23}$$

where F_{i-j} is the diffuse view factor from surface element i to j. Substituting Equation (2-22) into Equation (2-23) for those surface elements on the post-chamber wall yields

$$H_{\lambda,i} = \sum_{j=1}^{K-M} J_{\lambda,j} F_{i-j} + \sum_{j=K-M+1}^{K} \left[E_{b\lambda} + \left(\frac{1}{\varepsilon_p} - 1\right)\left(q_{conv,p} + q_{loss}\right)a \right]_j F_{i-j} \tag{2-24}$$

where M is the number of the surface elements on the post-chamber wall. Substituting Equations (2-24) into Equations (2-15), (2-16) and (2-18) and applying the resulting equations on each corresponding surface element, a system of linear equations is obtained. The K unknown variables of the linear equations are the radiosities J_λ on the free interface and the furnace wall, and the blackbody emissive power $E_{b\lambda}$ on the post-chamber wall, which can be easily solved by matrix inversion. Once the radiosities and the blackbody emissive power for each wavelength band are solved, the irradiations can be determined from Equation (2-24). The temperature of the post-chamber wall can also

be obtained from the total blackbody emissive power. Since the calculation of q_{loss} requires the temperature of the post-chamber, iteration is needed for the temperature.

Since q_λ^+ in Equation (2-15) has to be obtained from the radiation intensities from within the glass media, and the irradiations H_λ are needed in evaluating the radiative transfer boundary condition given by Equation (2-14), the enclosure analysis is coupled with the solution of the radiative transfer in the glass.

2.3.5 Computation of View Factors

In the enclosure analysis and the calculation of the radiation boundary condition at the free surface, view factors between any two ring elements of the enclosure are important geometry parameters for the computation of irradiations given by Equation (2-23). There are four groups of view factors in the enclosure: 1) from the free surface to the furnace wall; 2) from the furnace wall to the free surface; 3) from the furnace wall to the furnace wall; 4) from the free surface to the free surface. Since most part of the free surface is convex, the last group of view factors is close to zero and can be neglected. The close-form solution of the first group of view factors can be found in Myers (1989). The second group of view factors can be obtained by the law of reciprocity:

$$F_{dA_f - dA_g} = \frac{dA_g}{dA_f} F_{dA_g - dA_f} \tag{2-25}$$

where dA_g and dA_f are the areas of the glass surface and the furnace wall elements, respectively; $F_{i\text{-}j}$ is the view factor from the element i to the element j.

Since the furnace wall is concave, the view factors between the elements of the furnace wall should be considered. The glass cylinder inside the furnace partly blocks

the view from one ring element to another on the furnace wall. As shown in Figure 2-4, the arbitrary point a_1 on the ring element dA_1 can only see part of another ring element dA_2 between point a_2 and a_3. The shadowed area in dA_2 is blocked by the glass and cannot be seen by a_1. Line a_1a_2 and a_1a_3 are tangential to the glass cylinder with the interception point b_1 and b_2.

The system in Figure 2-4 with all the critical points is projected onto the x-y plane as shown in Figure 2-5, where a_4 is an arbitrary point on the ring element dA_2 that can be seen by a_1. The unit normal vectors at point a_1 and a_4 as shown in the figure can be given by

$$\hat{n}_1 = \hat{j} \tag{2-26}$$

$$\hat{n}_2 = -\sin\varphi\,\hat{i} + \cos\varphi\,\hat{j} \quad 0 < \varphi < \varphi_{\max} \tag{2-27}$$

where φ is the include angle between the two unit normal vectors. The location vectors corresponding to point a_1 and a_4 in the coordinate system shown in Figure 2-4 can be given by

$$\mathbf{r}_{a1} = -R_f\,\hat{j} + z_1\hat{k} \tag{2-28}$$

$$\mathbf{r}_{a4} = R_f \sin\varphi\,\hat{i} - R_f \cos\varphi\,\hat{j} + z_2\hat{k} \tag{2-29}$$

where z_1 and z_2 are the axial coordinates of a_1 and a_4, respectively. The vector connecting a_1 and a_4 can then be given by

$$\mathbf{s} = \mathbf{r}_{a4} - \mathbf{r}_{a1} = R_f \sin\varphi\,\hat{i} + \left(R_f - R_f\cos\varphi\right)\hat{j} + \left(z_2 - z_1\right)\hat{k} \tag{2-30}$$

The view factor from the ring element dA_1 to dA_2 can be calculated by

$$F_{dA_1-dA_2} = \frac{2dz_2 R_f}{\pi}\int_0^{\varphi_{\max}} \frac{(\hat{n}_1\cdot\mathbf{s})(\hat{n}_2\cdot\mathbf{s})}{s^4}d\varphi$$
$$= \frac{2dz_2}{\pi R_f}\int_0^{\varphi_{\max}} \frac{(1-\cos\varphi)^2 d\varphi}{\left[2(1-\cos\varphi)+\left(\frac{z_2-z_1}{R_f}\right)^2\right]^2} \quad (2\text{-}31)$$

where dz_2 is the width of the ring element dA_2.

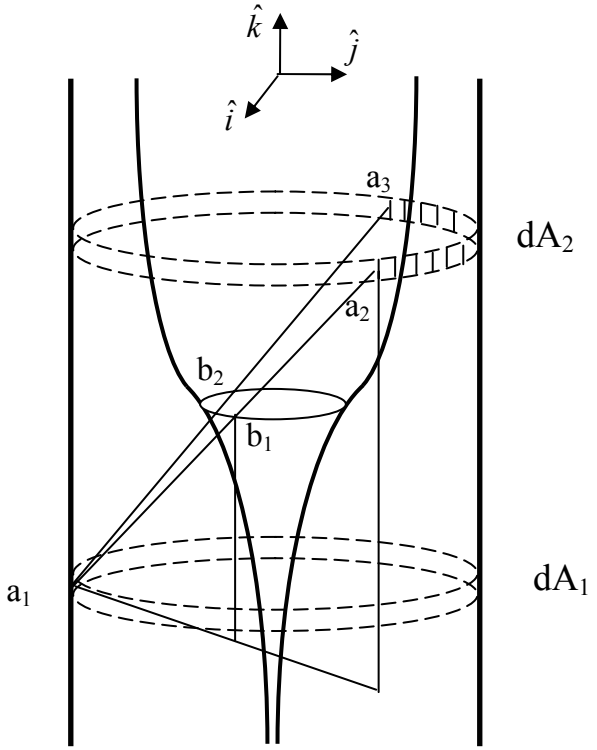

Figure 2-4 Schematic for the view factor between two furnace ring elements

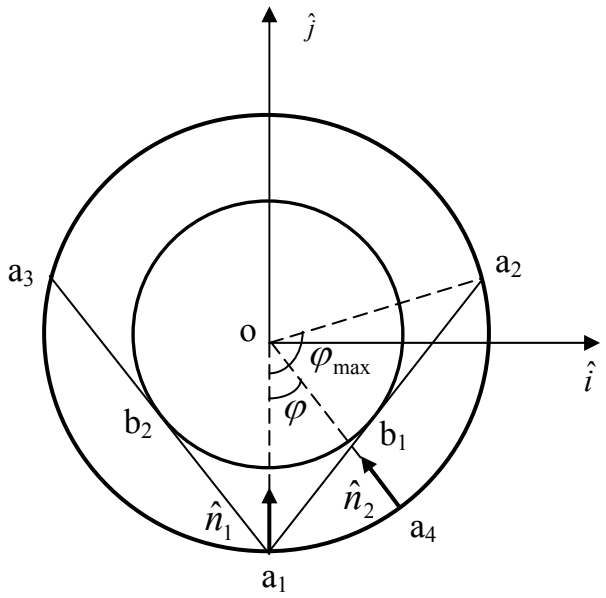

Figure 2-5 Projection of the system in Figure 2-4 on the x-y plane

In order to calculate the above view factor, we need to obtain the angular integration limit $\varphi_{\max}$. Since the diameter of the glass cylinder changes arbitrarily, the diameter of the tangential circle passing through point b_1 and b_2 (inner circle in Figure 2-5) has to be found by the following numerical searching scheme. Figure 2-6 illustrates the searching method. The angle φ_0 decreases from π toward 0 incrementally with a small constant angular interval. Point a_2 moves along the circle (with the furnace diameter) as φ_0 decreases. At each value of φ_0, b_1 moves from a_1 to a_2 along the line connecting the two points. Using the geometry relationship shown in Figure 2-6, we have the following expression:

$$d_1 = \left|a_1 a_2\right| = 2R_f \sin\left(\frac{\varphi_0}{2}\right) \tag{2-32}$$

$$d_2 = |a_1 b_1| = R_f \sin\left(\frac{\varphi_0}{2}\right) - R_f \cos\left(\frac{\varphi_0}{2}\right)\tan\left(\frac{\varphi_0}{2} - \varphi\right) \tag{2-33}$$

$$r_3 = |ob_1| = \frac{R_f \cos(\varphi_0 / 2)}{\cos(\varphi_0 / 2 - \varphi)} \tag{2-34}$$

where d_1, d_2 and r_3 are defined in the above equations. As illustrated in Figure 2-4, the following relationship can be identified:

$$\frac{z_3 - z_1}{z_2 - z_1} = \frac{d_2}{d_1} \tag{2-35}$$

where z_1, z_2 and z_3 are axial coordinates of point a_1, a_2 and b_1, respectively. z_3 can be easily solved by substituting Equation (2-32) and (2-33) into Equation (2-35). The radius of the glass cylinder at the axial coordinate z_3 can be obtained from the free surface profile $R(z)$. If there exists a location of b_1 on line a_1a_2 such that $r_3 < R(z_3)$, then line a_1a_2 must cut through the glass cylinder. As φ_0 decreases from π towards 0 by small intervals, the first value of φ_0 that makes $r_3 \geq R(z_3)$ hold for any location of b_1 on line a_1a_2 is the value for $\varphi_{\max}$. Usually $\varphi_{\max}$ is close to π, so this numerical searching does not take too much computation time.

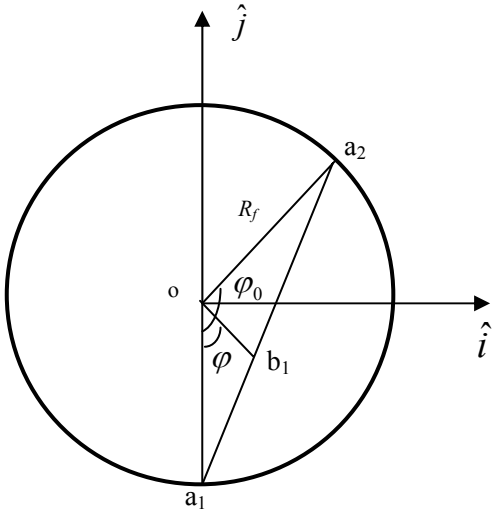

Figure 2-6 Schematic for numerical searching of $\varphi_{\max}$

2.4 FVM for the solution of RTE

In this study, the finite volume method (FVM) is used to solve Equation (2-9). The 2-D spatial domain is divided into finite control volumes, each of which has a local orientation coordinate system as shown in Figure 2-1. The whole solid angle space in each local coordinate system is further divided into finite control angles as shown in Figure 2-7 (only one control angle is shown). The RTE is solved along each direction of the control angle at each spatial control volume. The main difference between the popular discrete ordinate method (DOM) and FVM is that in DOM, it is assumed that not only the magnitude but also the direction of intensity is constant within the control angle, but in FVM, the direction of intensity may vary. This makes FVM more accurate than DOM in a numerical point of view. The other advantage of FVM is that the control angles can be arbitrarily specified pertaining to each problem dealt with.

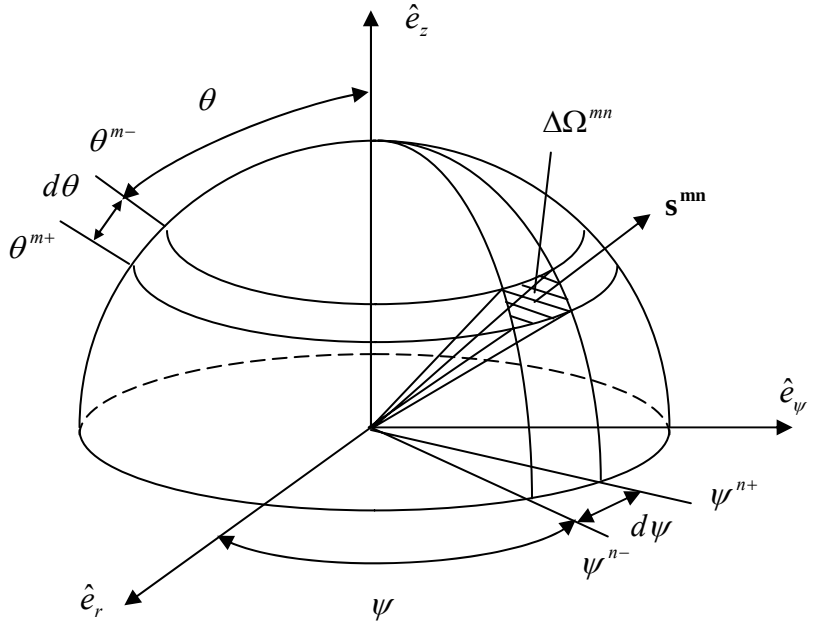

Figure 2-7 Representative control solid angle in the local coordinate system

The same 2-D spatial control volumes used in solving the fluid dynamic equations can also be used in the solution of the RTE. In the local orientation system at each spatial control volume, the radiative transfer is symmetric about the r-z plane. Hence, we only need to calculate the radiation intensities in a hemisphere of the solid angle space ($0 < \psi < \pi$, $0 < \theta < \pi$). The polar angular space of π is divided into M discrete angles with a constant interval of $d\theta$. The azimuthal angular space of π is divided into N discrete angles with a constant interval of $d\psi$. The hemisphere is then divided into $M \times N$ control solid angles. Figure 2-8 shows the projection on the r-z plane of the hemisphere that is divided into 4×4 control solid angles.

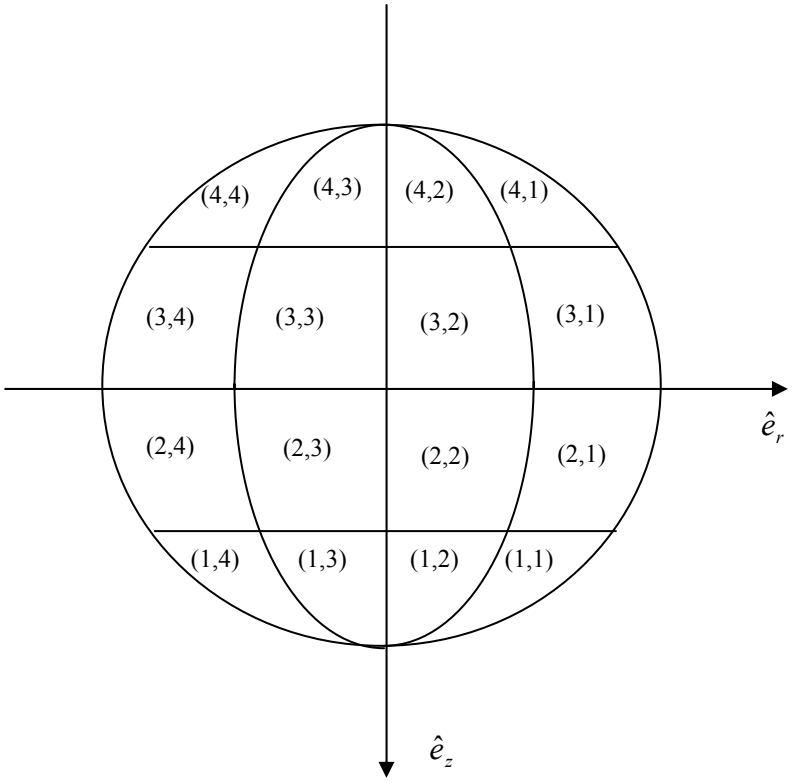

Figure 2-8 Projection of the hemisphere divided into 4×4 control angles

In the following equations, the superscripts m and n denote the orientation at the m^{th} polar angle interval and the n^{th} azimuthal angle interval, respectively (m = 1, 2, ..., M; n = 1, 2, …, N). For convenience, the subscript λ is dropped from now on, but it should be kept in mind that the intensities and the median radiation properties are all spectral values and are evaluated in different bands of the spectrum.

Following the artifice of Carlson and Lathrop (1968), the angular derivative term in Equation (2-9) is approximated as

$$\frac{\partial}{\partial \psi}\left(\gamma^{mn} I^{mn}\right) = \frac{a^{m,n+1/2} I^{m,n+1/2} - a^{m,n-1/2} I^{m,n-1/2}}{\Delta\Omega^{mn}} \tag{2-36}$$

where the discrete control (solid) angle as shown in Figure 2-7 is given by

$$\Delta\Omega^{mn} = \int_{\psi^{n-}}^{\psi^{n+}} \int_{\theta^{m-}}^{\theta^{m+}} \sin\theta d\theta d\psi \tag{2-37}$$

and $a^{m,n\pm1/2}$ are the coefficients for the intensities on the faces of the control angle and will be determined after the discretization of the RTE.

After the substitution of Equation (2-36), Equation (2-9) is spatially discretized by central difference and integrated over a control angle $\Delta\Omega^{mn}$, assuming that the magnitude of intensity is constant within the control angle, but allowing its direction to vary. The following equation is obtained:

$$\begin{aligned} \sum_{i=e,s} I_i^{mn} D_i^{mn} - \sum_{i=w,n} I_i^{mn} D_i^{mn} - G\left(a^{m,n+1/2} I_P^{m,n+1/2} - a^{m,n-1/2} I_P^{m,n-1/2}\right) \\ = r\kappa G\left(I_b - I_P^{mn}\right)\Delta\Omega^{mn} \end{aligned} \tag{2-38}$$

where *e, n, w* and *s* denote the east, north, west and south faces of the control volume, and the subscript "*p*" denotes the center node of the control volume. The face intensity weight D_i^{mn} in the above equation is given by

$$\begin{aligned} D_i^{mn} &= r_i \int_{\Delta\Omega^{mn}} \mathbf{A}_i \cdot \mathbf{s} d\Omega \\ &= \begin{cases} r_i G_i \left(\eta_{ri} D_{cr}^{mn} + \eta_{zi} D_{cz}^{mn} \right) & for\ i = e, w \\ r_i G_i \left(\xi_{ri} D_{cr}^{mn} + \xi_{zi} D_{cz}^{mn} \right) & for\ i = s, n \end{cases} \end{aligned} \tag{2-39}$$

where $\mathbf{A}_i$ is vector whose magnitude is equal to the control volume face area and whose direction is normal to the control volume face, and

$$D_{cr}^{mn} = \int_{\psi^{n-}}^{\psi^{n+}} \int_{\theta^{m-}}^{\theta^{m+}} (\sin\theta\cos\psi) \sin\theta \, d\theta d\psi \tag{2-40}$$

$$D_{cz}^{mn} = \int_{\psi^{n-}}^{\psi^{n+}} \int_{\theta^{m-}}^{\theta^{m+}} \cos\theta \sin\theta \, d\theta d\psi \tag{2-41}$$

Equation (2-38) can be interpreted as the conservation of radiative energy. The left hand side of the equation is the net change of the radiative flux through the control volume; the right hand side is the volumetrically emitted radiative power minus the absorbed radiative power. Since $a^{mn\pm 1/2}$ are the geometric coefficients for the intensities on the faces of the control angle, they do not depend on the intensities. The following recursive relation can be obtained by assuming all the facial and nodal intensities in Equation (2-38) are equal to the blackbody emission intensity I_b:

$$a^{m,n+1/2} - a^{m,n-1/2} = \frac{1}{G} \left(\sum_{i=e,n} D_i^{mn} - \sum_{i=w,s} D_i^{mn} \right) = D_{cr}^{mn} \tag{2-42}$$

subject to the boundary condition $a^{m,N+1/2} = 0$.

Since $I_{e,w,s,n}^{mn}$ and $I_P^{m,n\pm1/2}$ appear in Equation (2-38), supplementary relationships between these intensities and the nodal intensity I_P^{mn} are required to solve the discretized equation. In order to ensure positive intensity solution (there are no physical negative intensities), the following step scheme is used to relate the facial and edge intensities to the nodal intensity:

$$I_e^{mn} D_e^{mn} = I_P^{mn} \max\left(D_e^{mn},0\right) - I_E^{mn} \max\left(-D_e^{mn},0\right) \tag{2-43}$$

$$I_w^{mn} D_w^{mn} = I_W^{mn} \max\left(D_w^{mn},0\right) - I_P^{mn} \max\left(-D_w^{mn},0\right) \tag{2-44}$$

$$I_s^{mn} D_s^{mn} = I_P^{mn} \max\left(D_s^{mn},0\right) - I_S^{mn} \max\left(-D_s^{mn},0\right) \tag{2-45}$$

$$I_n^{mn} D_n^{mn} = I_N^{mn} \max\left(D_n^{mn},0\right) - I_P^{mn} \max\left(-D_n^{mn},0\right) \tag{2-46}$$

$$I_P^{m,n-1/2} = I_P^{mn} \tag{2-47}$$

where the subscripts E, W, S and N denote the adjacent eastern, western, southern and northern nodal values.

Substituting Equation (2-43) ~ (2-47) into Equation (2-38) and rearranging the resulting equation for I_P^{mn} yields

$$g_P^{mn} I_P^{mn} = \sum_{i=E,W,S,N} g_i^{mn} I_i^{mn} + h_a^{mn} I_P^{m,n+1} + h_b^{mn} I_b \tag{2-48}$$

where the coefficients are given by

$$\begin{aligned} g_P^{mn} = {} & \max\left(D_e^{mn},0\right) + \max\left(-D_w^{mn},0\right) + \max\left(D_s^{mn},0\right) + \max\left(-D_n^{mn},0\right) \\ & + a^{m,n-1/2} G + r\kappa G \Delta\Omega^{mn} \end{aligned} \tag{2-49}$$

$$g_i^{mn} = \max\left(-D_j^{mn},0\right) \quad i = E,S;\ j = e,s \tag{2-50}$$

$$g_i^{mn} = \max\left(D_j^{mn}, 0\right) \quad i = W, N;\ j = w, n \tag{2-51}$$

$$h_a^{mn} = a^{m,n+1/2} G \tag{2-52}$$

$$h_b^{mn} = r\kappa G \Delta\Omega^{mn} \tag{2-53}$$

when $n = N$, arbitrary value can be assigned to $I_P^{m,N+1}$ since its coefficient $h_a^{m,N}$ is zero.

Using the parameters defined in Equation (2-39), (2-40) and (2-41), the one-way radiative flux required in the calculation of the free surface boundary conditions in Equation (2-14) and (2-15) can be obtained by

$$\begin{aligned}\left(q_r^+ \mathbf{r} + q_z^+ \mathbf{z}\right) \cdot \mathbf{n} &= \int_{\Omega=2\pi, \mathbf{n}\cdot\mathbf{s}>0} I_P (\mathbf{n}\cdot\mathbf{s}) d\Omega \\ &= 2 \sum_{D_e^{mn}>0} I_P^{mn} \left(n_r D_{cr}^{mn} + n_z D_{cz}^{mn}\right)\end{aligned} \tag{2-54}$$

where n_r and n_z are the radial and axial components of the normal vector along the free surface. Note that the number of terms included in the above summation which satisfy $D_e^{mn} > 0$ may vary since the direction of the surface normal changes dramatically along the free interface.

The solution of the radiative transfer in the glass media and the enclosure analysis are carried out separately. Due to the coupled boundary condition along the free interface, an iteration and an initial estimation of the radiosities (intensities) at the inner surface of the free interface ($\mathbf{s}\cdot\mathbf{n} < 0$) are required. Initial estimation of the post-chamber temperature is also required as discussed in Section 2.3.4. I_p is computed using Equation (2-48) along all the discrete solid angle directions and at all the control volumes by sweeping the domain in four groups of directions as shown in Figure 2-9. Given the

initial estimation or the intermediate values of the intensities at the free surface and the top and the bottom boundaries, the sweep starts from the bottom-right and top-right corners then proceeds into the domain until each control volume are visited once for each sweep. The symmetric boundary condition given by Equation (2-11) is then used to obtain the boundary intensities along the centerline pointing into the computation domain. The sweep now starts from the bottom-left and top-left corners and proceeds into the domain. The positive one-way flux along the free surface can now be calculated using Equation (2-54). The K linear equations for the radiosities and the emissive power in the outer enclosure analysis are then solved. The results are substituted into Equation (2-24) to obtain the irradiation on the free interface. The post-chamber wall temperature can be updated using the blackbody emissive power. The radiosities (intensities) on the inner surface of the free interface can be updated using Equation (2-14). The updated radiosities are then compared with the values in the last iteration. If the norm of the difference is larger than a specified small number, the calculation starts over again until the radiosities at the inner surface of the free interface and the post-chamber temperature do not change by a considerable amount.

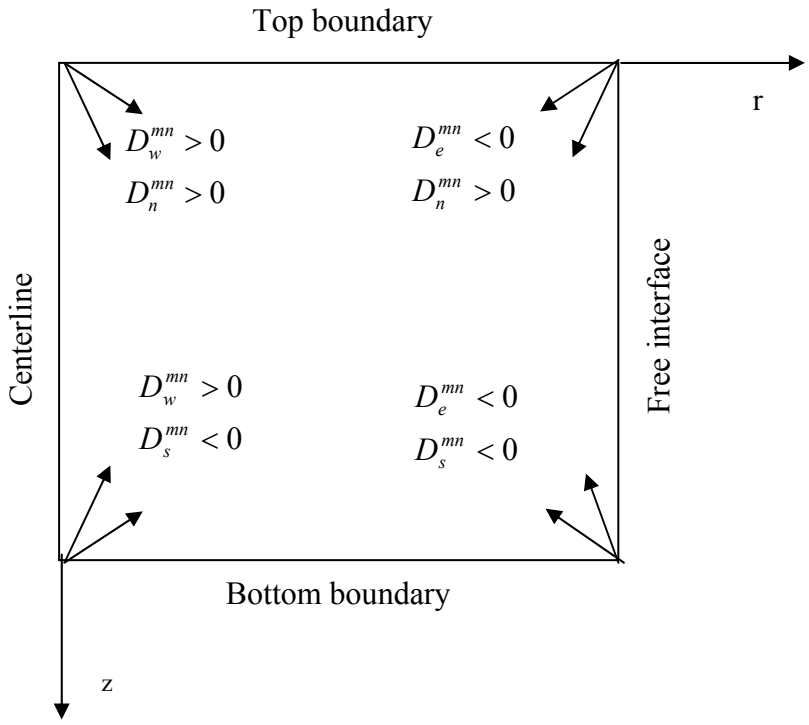

Figure 2-9 Four groups of intensity directions in the sweeps

CHAPTER III

THERMO-FLUID MODELING AND NUMERICAL SOLUTION

3.1 Overview

In this chapter, the mathematical models of the thermo-fluid transport in the fiber drawing process are presented. At first, the 2-D dimensionless governing equations for both the glass flow and the air convection are presented in Section 3.2. It is followed by the formulation of the boundary conditions in Section 3.3. In Section 3.4, a semi 2-D model is developed by deriving a 1-D free surface correction scheme for efficient steady state free surface computation. Section 3.5 presents the numerical solution of the models. The governing equations and boundary conditions are transformed in a curvilinear coordinate system and discretized on a staggered grid. The Navier-Stokes equations are solved by the ACM scheme for the glass domain, while by the PISO scheme for the air domain. Finally, the computation procedures for the complete conjugate problem are developed.

3.2 Mathematical Models

The following assumptions and considerations are made in the modeling of the thermo-fluid transports in both the glass and air domain:

(1) Both the glass flow and the air convection are axisymmetric in the cylindrical coordinate system.

(2) The glass flow is Newtonian and incompressible. On the other hand, the air flow is compressible due to the variation of density caused by the large temperature difference between the furnace and the ambient. The buoyancy force is considered, but *Bossinesq* approximation is not used.

(3) The temperature dependency of physical properties of both the glass and the air (viscosity, thermal conductivity, specific heat, etc.) are considered.

(4) The viscous dissipation in the glass is considered, but neglected in the air.

(5) The turbulence in the air boundary layer around the continuous moving fiber is accounted for by using simple empirical algebraic turbulence model.

The general 2-D governing equations for the conservation of mass, momentum and energy are given in the cylindrical coordinates system (Schlichting, 2000):

$$\frac{\partial \rho}{\partial t} + \frac{1}{r}\frac{\partial}{\partial r}(r\rho u) + \frac{\partial}{\partial z}(\rho v) = 0 \tag{3-1}$$

$$\rho\frac{\partial u}{\partial t} + \rho u\frac{\partial u}{\partial r} + \rho v\frac{\partial u}{\partial z} = -\frac{\partial p}{\partial r} + \frac{1}{r}\frac{\partial}{\partial r}\left(2\mu r\frac{\partial u}{\partial r}\right) - 2\mu\frac{u}{r^2} + \frac{\partial}{\partial z}\left[\mu\left(\frac{\partial u}{\partial z} + \frac{\partial v}{\partial r}\right)\right] \tag{3-2}$$

$$\rho\frac{\partial v}{\partial t} + \rho u\frac{\partial v}{\partial r} + \rho v\frac{\partial v}{\partial z} = -\frac{\partial p}{\partial z} + \frac{1}{r}\frac{\partial}{\partial r}\left[\mu r\left(\frac{\partial u}{\partial z} + \frac{\partial v}{\partial r}\right)\right] + \frac{\partial}{\partial z}\left(2\mu\frac{\partial v}{\partial z}\right) + \rho g \tag{3-3}$$

$$\rho C_p\left(\frac{\partial T}{\partial t} + u\frac{\partial T}{\partial r} + v\frac{\partial T}{\partial z}\right) = \frac{1}{r}\frac{\partial}{\partial r}\left(kr\frac{\partial T}{\partial r}\right) + \frac{\partial}{\partial z}\left(k\frac{\partial T}{\partial z}\right) - \nabla\cdot\mathbf{q}_R + \mu\Phi \tag{3-4}$$

where p, u, v and T are the pressure, the radial and axial components of velocity, and the temperature, respectively; ρ, μ, k, C_p are the density, the viscosity, the thermal conductivity and the specific heat, respectively; g is the gravitational acceleration; $\mathbf{q}_R$ is

the radiative heat flux in the participating glass media, the solution of which has been described in Chapter II. The dissipation function Φ is given by

$$\Phi = 2\left[\left(\frac{\partial u}{\partial r}\right)^2 + \left(\frac{u}{r}\right)^2 + \left(\frac{\partial v}{\partial z}\right)^2\right] + \left(\frac{\partial u}{\partial z} + \frac{\partial v}{\partial r}\right)^2 \tag{3-5}$$

The source terms of the radiative transfer and the viscous dissipation in the energy equation are dropped for the air domain.

3.2.1 Dimensionless Form in the Glass Domain

All the variables in the glass domain are nondimensionalized to the following characteristic quantities as follows:

$$r^* = \frac{r}{R_p}, \quad z^* = \frac{z}{R_p}, \quad t^* = \frac{t}{R_p / v_f},$$

$$u^* = \frac{u}{v_f}, \quad v^* = \frac{v}{v_f}, \quad p^* = \frac{p}{\rho v_f{}^2}, \quad T^* = \frac{T}{T_m}, \tag{3-6}$$

$$\left(\nabla \cdot \mathbf{q}_R\right)^* = \frac{\nabla \cdot \mathbf{q}_R}{\rho C p_m T_m v_f / R_p}, \ \mu^* = \frac{\mu}{\mu_m}, \ k^* = \frac{k}{k_m}, \ C_p^* = \frac{C_p}{C_{pm}}$$

where R_p is the preform radius; v_f is the draw speed; T_m is the glass melting point; C_{pm}, μ_m, and k_m are the thermal capacity, viscosity, and thermal conductivity of the glass at the melting point.

Using the above defined dimensionless variables, Equations (3-1) to (3-4) for the incompressible glass flow can be written as

$$\frac{1}{r^*}\frac{\partial}{\partial r^*}\left(r^* u^*\right) + \frac{\partial v^*}{\partial z^*} = 0 \tag{3-7}$$

$$\frac{\partial u^*}{\partial t^*} + u^* \frac{\partial u^*}{\partial r^*} + v^* \frac{\partial u^*}{\partial z^*} = -\frac{\partial p^*}{\partial r^*} + \frac{1}{\mathrm{Re}}\left\{\frac{1}{r^*}\frac{\partial}{\partial r^*}\left(2\mu^* r^* \frac{\partial u^*}{\partial r^*}\right) - 2\mu^* \frac{u^*}{r^{*2}} + \frac{\partial}{\partial z^*}\left[\mu^*\left(\frac{\partial u^*}{\partial z^*} + \frac{\partial v^*}{\partial r^*}\right)\right]\right\} \tag{3-8}$$

$$\frac{\partial v^*}{\partial t^*} + u^* \frac{\partial v^*}{\partial r^*} + v^* \frac{\partial v^*}{\partial z^*} = -\frac{\partial p^*}{\partial z^*} + \frac{1}{\mathrm{Re}}\left\{\frac{1}{r^*}\frac{\partial}{\partial r^*}\left[\mu^* r^*\left(\frac{\partial u^*}{\partial z^*} + \frac{\partial v^*}{\partial r^*}\right)\right] + \frac{\partial}{\partial z^*}\left(2\mu^* \frac{\partial v^*}{\partial z^*}\right)\right\} + \frac{1}{Fr} \tag{3-9}$$

$$C_p^*\left(\frac{\partial T^*}{\partial t^*} + u^* \frac{\partial T^*}{\partial r^*} + v^* \frac{\partial T^*}{\partial z^*}\right) = \frac{1}{Pe}\left[\frac{1}{r^*}\frac{\partial}{\partial r^*}\left(k^* r^* \frac{\partial T^*}{\partial r^*}\right) + \frac{\partial}{\partial z^*}\left(k^* \frac{\partial T^*}{\partial z^*}\right)\right] - \left(\nabla \cdot \mathbf{q}_R\right)^* + \frac{Ec}{\mathrm{Re}}\mu^* \Phi^* \tag{3-10}$$

where the dimensionless groups, *Reynolds*, *Froude, Peclet*, and *Eckert* numbers, are defined by

$$\mathrm{Re} = \frac{\rho v_f R_p}{\mu_m},\ Fr = \frac{v_f^{\,2}}{g R_p},\ Pe = \frac{v_f R_p}{\alpha_m},\ \text{and } Ec = \frac{v_f^{\,2}}{C_{pm} T_m} \tag{3-11}$$

where α_m is the thermal diffusivity at the melting temperature.

3.2.2 Dimensionless Form in the Air Domain

Similarly, all the variables in the air domain are nondimensionalized to the following characteristic quantities as follows:

$$r^* = \frac{r}{R_p},\quad z^* = \frac{z}{R_p},\quad t^* = \frac{t}{R_p/\widetilde{v}},\quad \widetilde{v} = \frac{\alpha_\infty}{R_p},$$
$$u^* = \frac{u}{\widetilde{v}},\quad v^* = \frac{v}{\widetilde{v}},\quad p^* = \frac{p - p_\infty}{\rho_\infty \widetilde{v}^{\,2}},\quad T^* = \frac{T - T_\infty}{T_m - T_\infty}, \tag{3-12}$$

$$\mu^* = \frac{\mu}{\mu_\infty}, \quad k^* = \frac{k}{k_\infty}, \quad C_p{}^* = \frac{C_p}{C_{p\infty}}, \quad \rho^* = \frac{\rho}{\rho_\infty}$$

where $\tilde{v}$ is a reference velocity, and the subscript "∞" denotes the value at the ambient temperature. Using the above defined dimensionless variables, Equations (3-1) to (3-4) for the air domain can be written as

$$\frac{\partial \rho^*}{\partial t^*} + \frac{1}{r^*}\frac{\partial}{\partial r^*}\left(r^* \rho^* u^*\right) + \frac{\partial}{\partial z^*}\left(\rho^* v^*\right) = 0 \tag{3-13}$$

$$\begin{aligned}\rho^*\left(\frac{\partial u^*}{\partial t^*} + u^*\frac{\partial u^*}{\partial r^*} + v^*\frac{\partial u^*}{\partial z^*}\right) = -\frac{\partial p^*}{\partial r^*} + \mathrm{Pr}\left\{\frac{1}{r^*}\frac{\partial}{\partial r^*}\left(2\mu^* r^*\frac{\partial u^*}{\partial r^*}\right)\right. \\ \left. - 2\mu^*\frac{u^*}{r^{*2}} + \frac{\partial}{\partial z^*}\left[\mu^*\left(\frac{\partial u^*}{\partial z^*} + \frac{\partial v^*}{\partial r^*}\right)\right]\right\}\end{aligned} \tag{3-14}$$

$$\begin{aligned}\rho^*\left(\frac{\partial v^*}{\partial t^*} + u^*\frac{\partial v^*}{\partial r^*} + v^*\frac{\partial v^*}{\partial z^*}\right) = -\frac{\partial p^*}{\partial z^*} + \mathrm{Pr}\left\{\frac{1}{r^*}\frac{\partial}{\partial r^*}\left[\mu^* r^*\left(\frac{\partial u^*}{\partial z^*} + \frac{\partial v^*}{\partial r^*}\right)\right]\right. \\ \left. + \frac{\partial}{\partial z^*}\left(2\mu^*\frac{\partial v^*}{\partial z^*}\right)\right\} + \frac{\rho^*}{Fr}\end{aligned} \tag{3-15}$$

$$\rho^* C_p{}^*\left(\frac{\partial T^*}{\partial t^*} + u^*\frac{\partial T^*}{\partial r^*} + v^*\frac{\partial T^*}{\partial z^*}\right) = \frac{1}{r^*}\frac{\partial}{\partial r^*}\left(k^* r^*\frac{\partial T^*}{\partial r^*}\right) + \frac{\partial}{\partial z^*}\left(k^*\frac{\partial T^*}{\partial z^*}\right) \tag{3-16}$$

where the *Prantle* and *Froude* numbers are given by

$$\mathrm{Pr} = \frac{\nu_\infty}{\alpha_\infty}, \; Fr = \frac{\tilde{v}^2}{gR_p} \tag{3-17}$$

As the turbulence effects of the air convection around the moving fiber are considered, the μ and k of the air in the above equations include the eddy viscosity and conductivity, the calculation of which is described in Appendix C.

3.3 Boundary Conditions

In this section, the boundary conditions for both the glass domain and the air domain are developed.

3.3.1 Glass Domain

The melting glass media has a free moving boundary at the surface. The following boundary conditions (given in dimensionless form) should be satisfied along the interface between the glass and the air, denoted by the subscripts "g" and "a", respectively.

Force balance along the normal **n**

$$p_g^* - p_a^* + \frac{1}{\mathrm{Re}\,Ca}\zeta^*\kappa^* = \frac{1}{\mathrm{Re}}\left[2\mu_g^*\left.\frac{\partial V_n^*}{\partial n^*}\right|_g - 2\mu_a^*\left.\frac{\partial V_n^*}{\partial n^*}\right|_a\right] \tag{3-18}$$

Balance of tangential force

$$\mu_g^*\left.\frac{\partial V_t^*}{\partial n^*}\right|_g = \mu_a^*\left.\frac{\partial V_t^*}{\partial n^*}\right|_a \approx 0 \tag{3-19}$$

Heat flux continuity

$$-k_g^*\left.\frac{\partial T^*}{\partial n^*}\right|_g = \frac{1}{q_{m1}}\left(q''_{rad,opa} + q''_{conv}\right) \tag{3-20}$$

Kinematic condition

$$\frac{\partial R^*}{\partial t^*} + v^*\frac{\partial R^*}{\partial z^*} - u^* = 0 \tag{3-21}$$

where ζ is the surface tension and κ is the surface curvature; V_n and V_t are the normal and tangential components of the velocity at the interface; the Capillary number is given by $Ca = \mu_m v_f / \zeta_m$; $q_{rad,opa}$ is the net radiation heat flux in the opaque band and q_{conv} is the convective heat flux from the air; q_{m1} is given by $q_{m1} = k_m T_m / R_p$; the radius R of the glass is a function of z. The surface tension, the pressure variation and the normal stress

of the air in Equation (3-18) can be neglected since their magnitudes are several orders smaller than the other terms. The air pressure can be used as a reference and set to 0. Equation (3-18) and (3-19) are used as the boundary conditions for the two momentum equations; Equation (3-20) is used as the boundary condition for the energy equation; and Equation (3-21) is used to determine the free surface radius.

Since the system is axisymmetric, we have along the centerline,

$$\text{at } r = 0, \qquad u^* = 0,\ \frac{\partial v^*}{\partial r^*} = 0,\ \frac{\partial T^*}{\partial r^*} = 0 \tag{3-22}$$

At the furnace inlet,

$$\text{at } z = 0, \qquad u^* = 0, v^* = \frac{v_p}{v_f}, \frac{\partial^2 T^*}{\partial z^{*2}} = 0, R^* = 1 \tag{3-23}$$

where v_p is the feed rate. The glass temperature is extrapolated at the furnace inlet since no significant differences were found in the simulations when more detailed temperature boundary condition was modeled by extending the computational domain.

There are two cases of computation domain: (1) furnace only; and (2) furnace and post-chamber. In both cases, the glass temperature at the bottom boundary is extrapolated from the interior as the downstream temperature of the glass outside the domain does not have considerable effect on the upstream temperature of the glass.

$$\text{at } z = L \qquad \frac{\partial u^*}{\partial z^*} = 0,\ \frac{\partial^2 T^*}{\partial z^{*2}} = 0 \tag{3-24}$$

where $L = L_f$ in case (1), and $L = L_f + L_p$ in case (2). In case (1), the glass axial velocity at the exit is actually unknown since the glass solidifies far below the furnace. Instead of assuming an arbitrary value for the velocity or radius, we use a Neumann boundary

condition that can be obtained from the elongation model for the draw tension. In case (2), the axial velocity at the exit should be equal to the draw speed since the glass should solidify within the post-chamber. Hence,

at $z = L$

Case (1)
$$\frac{dv^*}{dz^*} = \frac{F_t^*}{3\mu^* \pi R^{*2}\left(z = L_f\right)} \tag{3-25}$$

Case (2)
$$v^* = 1 \tag{3-26}$$

where F_t is the draw tension of the glass at the furnace exit. The value of F_t can be measured and controlled immediately after the post-chamber. Since the glass diameter is very small after it exits the furnace, its inertia and gravitational effects between the furnace exit and the tension measuring point are negligible.

3.3.2 Air Domain

No-slip boundary conditions are assumed along the free interface, the furnace and post-chamber walls for the air.

at $r = R(z)$
$$u^* = u_g^*, \quad v^* = v_g^*, \quad T^* = T_g^* \tag{3-27}$$

at $r = R_{\text{fur}}$
$$u^* = v^* = 0, \quad T^* = \begin{cases} T_{fur}^* & z < L_f \\ T_{post}^* & z > L_f \end{cases} \tag{3-28}$$

where u_g^*, v_g^* and T_g^* are the radial, axial velocity components and the temperature along the glass free surface, respectively; T_{fur}^* , T_{post}^* are the furnace and post-chamber temperature, respectively; and R_{fur} is the furnace radius.

The top ring opening of the furnace is the exit of the buoyancy driven open-ended channel flow of the air. The velocity and the temperature at the edge can be extrapolated

from the interior values when the downstream values have small effects on the upstream ones. The pressure at the exit is equal to the ambient value.

$$\text{at } z = 0 \qquad \frac{\partial u^*}{\partial z^*} = \frac{\partial v^*}{\partial z^*} = \frac{\partial T^*}{\partial z^*} = 0, \quad p^* = 0 \tag{3-29}$$

At the bottom of the computation domain, two regions exist along the radial direction. No-slip boundary conditions are used for the iris region.

$$\text{at } z = L \text{ and } r > R_{\text{ope}} \qquad u^* = v^* = 0, \quad T^* = T^*_{iris} \tag{3-30}$$

where the iris temperature T^*_{iris} can be approximated as the ambient temperature, or can be calculated by balancing the heat flux; R_{ope} is the radius of the iris opening. At the small opening region, the *Bernoulli* equation is used to determine the pressure at the inlet cells at the iris opening.

$$\text{at } z = L \text{ and } r < R_{\text{ope}} \qquad p^* = -\frac{1}{2}\rho^* \bar{v}^{*2} \tag{3-31}$$

where

$$\bar{v}^* = \frac{2\int_{R_f}^{R_{ope}} v^* r dr}{{R_{ope}}^2 - R^2} \tag{3-32}$$

Again, the velocity components at the edge are extrapolated from the interior values. For the air flowing into the chamber, its temperature is equal to the ambient value; while for the air inside the boundary layer around the moving fiber, the temperature at the edge is also extrapolated from the interior value.

$$\text{at } z = L \text{ and } r < R_{\text{ope}} \qquad \frac{\partial u^*}{\partial z^*} = \frac{\partial v^*}{\partial z^*} = 0, \quad \begin{cases} \partial \mathrm{T}^*/\partial \mathrm{z}^* = 0 & (v > 0) \\ T^* = 0 & (v < 0) \end{cases} \tag{3-33}$$

3.4 Semi 2-D Model for Free Surface flow

Although the complete 2-D fluid dynamic model is used for most simulations in this study, the results have shown that the highly viscous glass flow has a close 1-D distribution in the axial direction. Any radial variation of the axial velocity is greatly reduced by the strong shear stress due to the large glass viscosity. In order to obtain an efficient computation algorithm, a 1-D glass flow model is developed for the prediction of the free surface. The temperature field is still solved using the 2-D model presented in the previous sections. The viscosity for the 1-D flow model is calculated using the radially lumped temperature from the 2-D temperature solution. This simplified semi 2-D model can greatly reduce the computational cost while maintains the accuracy for the prediction of the fiber solidification location when the long post-chamber has to be included in the computation domain.

The 1-D steady state flow model for the free surface flow can be derived using the mass conservation and the vertical force balance as follows:

$$\frac{d}{dz}\left(v^{*}\pi R^{*2}\right)=0 \tag{3-34}$$

$$\frac{d}{dz^{*}}\left(\pi R^{*2}v^{*2}\right)=\frac{d}{dz^{*}}\left(\sigma_{zz}^{*}\pi R^{*2}\right)+\frac{1}{Fr}\pi R^{*2} \tag{3-35}$$

where σ_{zz} is the axial normal stress. The surface tension force is neglected in Equation (3-35) since it has been verified in the 2-D solution that the surface tension is several orders of magnitude smaller than the viscous stress. The viscous force of the air on the glass surface is also neglected. For a Newtonian fluid, the normal stress is given by

$$\sigma_{zz}^{*} = -p^{*} + \frac{2\mu^{*}}{\mathrm{Re}}\frac{dv^{*}}{dz^{*}} \tag{3-36}$$

The pressure in the glass can be obtained from the normal force balance condition at the free surface given by Equation (3-18). The elongational model for the normal stress is derived as follows.

The unit normal vector along the free surface pointing outward is given by

$$\hat{n} = n_r\hat{i} + n_z\hat{j} = \frac{1}{\sqrt{1+R'^2}}\hat{i} - \frac{R'}{\sqrt{1+R'^2}}\hat{j} \tag{3-37}$$

where $\hat{i}$ and $\hat{j}$ are the unit vector along the radial and axial coordinate directions, respectively; the prime denotes the derivative with respect to z. The normal component of velocity along the free surface can be written as

$$\begin{aligned} V_n^{*} &= \vec{V}^{*}\cdot\hat{n} \\ &= \left(u^{*}\hat{i} + v^{*}\hat{j}\right)\cdot\left(n_r\hat{i} + n_z\hat{j}\right) \\ &= u^{*}n_r + v^{*}n_z \end{aligned} \tag{3-38}$$

Using the above expression, the derivative of V_n^{*} with respect to n^{*} can be written as

$$\begin{aligned} \frac{\partial V_n^{*}}{\partial n^{*}} &= \nabla V_n^{*}\cdot\hat{n} \\ &= \left(\frac{\partial V_n^{*}}{\partial r^{*}}\hat{i} + \frac{\partial V_n^{*}}{\partial z^{*}}\hat{j}\right)\cdot\left(n_r\hat{i} + n_z\hat{j}\right) \\ &= n_r^2\frac{\partial u^{*}}{\partial r^{*}} + n_r n_z\frac{\partial u^{*}}{\partial z^{*}} + n_z^2\frac{dv^{*}}{dz^{*}} + n_z\frac{dn_r}{dz^{*}}u^{*} + n_z\frac{dn_z}{dz^{*}}v^{*} \end{aligned} \tag{3-39}$$

Along the free surface, the steady state kinematic condition is given by

$$u^{*} = v^{*}R' \tag{3-40}$$

The derivative of Equation (3-40) with respect to z is given by

$$\frac{\partial u^*}{\partial z^*} = v^* R'' + \frac{dv^*}{dz^*} R' \tag{3-41}$$

Using the 2-D continuity equation $\partial u^* / \partial r^* + u^* / r^* + \partial v^* / \partial z^* = 0$ at the free surface and Equation (3-40), we obtain

$$\frac{\partial u^*}{\partial r^*} = -\frac{v^* R'}{R^*} - \frac{dv^*}{dz^*} \tag{3-42}$$

Substituting Equations (3-37) and (3-40) to (3-42) into Equation (3-39) and assuming R' is small (the maximum value of R' in our simulation is around 0.23, the square of which is 0.053<<1), we obtain the following equation upon simplification:

$$\begin{aligned} \frac{\partial V_n^*}{\partial n^*} &= \frac{1}{1+R'^2}\left(-\frac{R'}{R^*}v^* - \frac{dv^*}{dz^*}\right) \\ &\approx -\frac{R'}{R^*}v^* - \frac{dv^*}{dz^*} \end{aligned} \tag{3-43}$$

Expanding Equation (3-34) we obtain

$$\frac{R'}{R^*}v^* = -\frac{1}{2}\frac{dv^*}{dz^*} \tag{3-44}$$

Thus, the 1st term in the right-hand-side of Equation (3-18) becomes

$$\frac{\partial V_n^*}{\partial n^*} \approx -\frac{1}{2}\frac{dv^*}{dz^*} \tag{3-45}$$

Dropping the negligible terms, Equation (3-18) can be simplified to

$$p^* = \frac{2\mu^*}{\mathrm{Re}}\frac{\partial V_n^*}{\partial n^*} \tag{3-46}$$

Substituting Equation (3-45) into the above equation yields

$$p^* = -\frac{\mu^*}{\mathrm{Re}}\frac{dv^*}{dz^*} \tag{3-47}$$

Finally, substituting the above expression for the glass pressure into Equation (3-36) yields the following simple elongational model

$$\sigma_{zz}^* = \frac{3\mu^*}{\mathrm{Re}}\frac{dv^*}{dz^*} \tag{3-48}$$

From the mass conservation or Equation (3-34), we have the following relationship:

$$v^* = \frac{v_p^*}{R^{*2}} \tag{3-49}$$

Substituting Equation (3-49) and Equation (3-48) into the inertia and viscous terms of Equation (3-35), respectively, and then integrating the resulting equation twice with respect to z, we yield the following expression for v:

$$\begin{aligned} v^*\left(z^*\right) = v_p^* &- \frac{\mathrm{Re}}{Fr}\int_0^{z^*}\frac{1}{3\mu^* R^{*2}}\left(\int_0^{z^*} R^{*2}dz^*\right)dz^* \\ &- \mathrm{Re}\int_0^{z}\frac{1}{3\mu^* R^{*2}}\left(\int_0^{z^*}\frac{2v_p^{*2}}{R^{*3}}dR^*\right)dz^* + \int_0^{z^*}\frac{C_2}{3\mu^* R^{*2}}dz^* + C_1 \end{aligned} \tag{3-50}$$

where the two integration constants C_1 and C_2 can be determined by the velocity boundary conditions given by

$$\text{at } z = 0 \qquad v^* = v_p^* \tag{3-51}$$

$$\text{at } z = L_f + L_p \qquad v^* = 1 \tag{3-52}$$

where the glass velocity at the exit is equal to the draw speed since the fiber solidifies within the post-chamber. Substituting Equation (3-51) and (3-52) into Equation (3-50), we obtain

$$C_1 = 0 \tag{3-53}$$

$$C_2 = \frac{1}{\int_0^{L^*} \left(\mu^* R^{*2}\right)^{-1} dz^*} \left[1 - v_p^* + \frac{\mathrm{Re}}{3Fr} \int_0^{L^*} \frac{1}{\mu^* R^{*2}} \left(\int_0^{z^*} R^{*2} dz^* \right) dz^* + \frac{\mathrm{Re}\, v_p^{*2}}{3} \int_0^{L^*} \frac{1}{\mu^* R^{*2}} \left(1 - \frac{1}{R^{*2}} \right) dz^* \right] \tag{3-54}$$

Given the axial velocity distribution $v^*(z^*)$ obtained from Equation (3-50), we can easily obtain the glass free surface profile using Equation (3-49) by

$$R^*\left(z^*\right) = \sqrt{\frac{v_p^*}{v^*\left(z^*\right)}} \tag{3-55}$$

Since the calculation of $v^*(z^*)$ in Equation (3-50) requires the information of $R^*(z^*)$, both $v^*(z^*)$ and $R^*(z^*)$ are solved iteratively.

3.5 Numerical Solution of the Thermo-Fluid Model

Since the free interface has an arbitrary neck-down profile, the governing equations and boundary conditions in Section 3.2 and 3.3 need to be transformed in a curvilinear coordinate system (η, ξ). For convenience, the asterisks will be omitted from the dimensionless equations from now on. The transformed equations are given in Appendix D.

3.5.1 Discretization of the Governing Equations

In order to obtain a general form of discretization of the governing equations, the momentum and energy equations for both the glass and air domains can be cast into a general form of unsteady convection-diffusion equation:

$$\begin{aligned} & a\left[\frac{\partial}{\partial t}\left(\frac{\phi}{J}\right)+\frac{\partial}{\partial \eta}\left(\widetilde{U}\phi\right)+\frac{\partial}{\partial \xi}\left(\widetilde{V}\phi\right)\right] \\ & = F\left[\frac{\partial}{\partial \eta}\left(\Gamma^{11}\frac{\partial \phi}{\partial \eta}+\Gamma^{12}\frac{\partial \phi}{\partial \xi}\right)+\frac{\partial}{\partial \xi}\left(\Gamma^{12}\frac{\partial \phi}{\partial \eta}+\Gamma^{22}\frac{\partial \phi}{\partial \xi}\right)\right] \\ & + S - b\left[\frac{\partial}{\partial \eta}\left(Mp\right)+\frac{\partial}{\partial \xi}\left(Lp\right)\right] \end{aligned} \tag{3-56}$$

where ϕ represents the variables of u, v or T;

S is the source term of the equation;

and F, $\widetilde{U},\widetilde{V},\Gamma^{ij}$, M, L, a and b can be easily identified from the governing equations and given as follows:

$$F=\begin{cases} \dfrac{1}{\mathrm{Re}} & \text{glass momentum} \\ \dfrac{1}{Pe} & \text{glass energy} \\ \mathrm{Pr} & \text{air momentum} \\ 1 & \text{air energy}; \end{cases} \tag{3-57}$$

$$\widetilde{U}=\frac{U+\eta_t}{J};\ \widetilde{V}=\frac{V+\xi_t}{J}; \tag{3-58}$$

$$\Gamma^{ij}=\frac{\Gamma}{J}g^{ij}; \tag{3-59}$$

$$M = \begin{cases} \dfrac{\eta_r}{J} & \text{radial momentum equation} \\ \dfrac{\eta_z}{J} & \text{axial momentum equation ;} \end{cases} \tag{3-60}$$

$$L = \begin{cases} \dfrac{\xi_r}{J} & \text{radial momentum equation} \\ \dfrac{\xi_z}{J} & \text{axial momentum equation ;} \end{cases} \tag{3-61}$$

$$a = \begin{cases} 1 & \text{glass momentum equation} \\ C_p & \text{glass energy equation} \\ \rho & \text{air momentum equation} \\ \rho C_p & \text{air energy equation ;} \end{cases} \tag{3-62}$$

$$b = \begin{cases} 1 & \text{momentum equation} \\ 0 & \text{energy equation ;} \end{cases} \tag{3-63}$$

and where Γ is the diffusivity coefficient, which is μ for the momentum equation; k for the energy equation.

The finite difference method is used to discretize all the terms in Equation (3-56). The computational stencil is shown in Figure 3-1. The shaded block is the control volume whose center node is denoted by P. All the neighboring grid nodes are denoted by the upper case letters which represent the position relative to the central node. The faces of the shaded control volume are denoted by the lower case letters.

Time derivative term

The 1st order time derivative term can be discretized by 2nd order accurate one-sided difference scheme

$$\frac{\partial}{\partial t}\left(\frac{\phi}{J}\right)=\frac{1.5(\phi/J)^{n+1}-2(\phi/J)^{n}+0.5(\phi/J)^{n-1}}{\Delta t} \tag{3-64}$$

where n+1, n and n-1 denote the next, current and last time step, respectively; and Δt is the simulation time step.

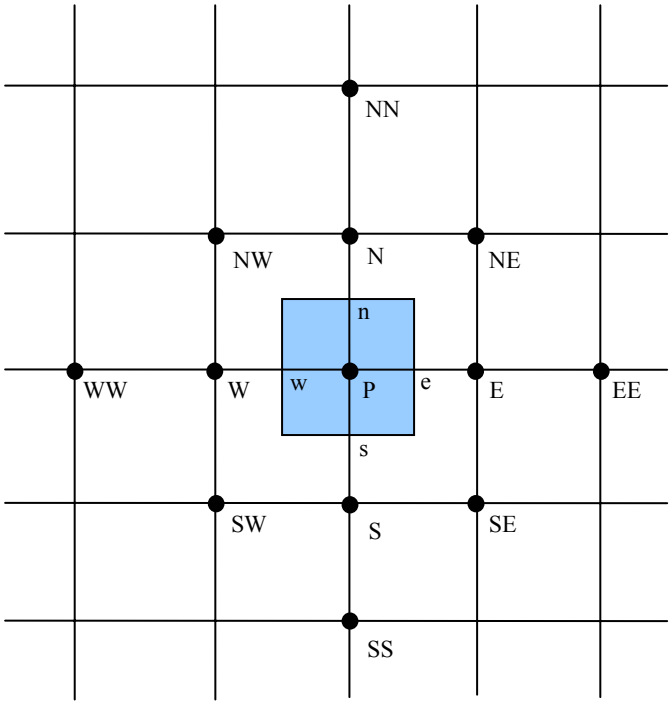

Figure 3-1 Computational stencil

Convective term

The coefficients for the variables at the neighboring grid points should be kept positive in order to guarantee the robustness of the numerical solution. To achieve this while keeping the second order accuracy, the second order upwind scheme is used to discretize the convective terms as follows:

$$\frac{\partial}{\partial \eta}\left(\widetilde{U}\phi\right)+\frac{\partial}{\partial \xi}\left(\widetilde{V}\phi\right)\approx \widetilde{U}_e\phi_e-\widetilde{U}_w\phi_w+\widetilde{V}_s\phi_s-\widetilde{V}_n\phi_n \tag{3-65}$$

where

$$\widetilde{U}_e\phi_e=\left[\phi_P+0.5\left(\phi_P-\phi_W\right)\right]\max(\widetilde{U}_e,0)-\left[\phi_E+0.5\left(\phi_E-\phi_{EE}\right)\right]\max(-\widetilde{U}_e,0) \tag{3-66}$$

$$\widetilde{U}_w\phi_w=\left[\phi_W+0.5\left(\phi_W-\phi_{WW}\right)\right]\max(\widetilde{U}_w,0)-\left[\phi_P+0.5\left(\phi_P-\phi_E\right)\right]\max(-\widetilde{U}_w,0) \tag{3-67}$$

$$\widetilde{U}_s\phi_s=\left[\phi_P+0.5\left(\phi_P-\phi_N\right)\right]\max(\widetilde{V}_s,0)-\left[\phi_S+0.5\left(\phi_S-\phi_{SS}\right)\right]\max(-\widetilde{V}_s,0) \tag{3-68}$$

$$\widetilde{U}_n\phi_n=\left[\phi_N+0.5\left(\phi_N-\phi_{NN}\right)\right]\max(\widetilde{V}_n,0)-\left[\phi_P+0.5\left(\phi_P-\phi_S\right)\right]\max(-\widetilde{V}_n,0) \tag{3-69}$$

In the above equations, the variables at the control volume faces are extrapolated from the neighboring two nodes on one side instead of interpolating from two adjacent nodes on both sides. This is how the coefficients of neighboring grid variables are guaranteed positive and the second order accuracy is also maintained in the discretization.

Diffusion term

The diffusion term and the pressure term can be discretized by the second order central difference scheme.

$$\frac{\partial}{\partial \eta}\left(\Gamma^{11}\frac{\partial \phi}{\partial \eta}+\Gamma^{12}\frac{\partial \phi}{\partial \xi}\right)+\frac{\partial}{\partial \xi}\left(\Gamma^{12}\frac{\partial \phi}{\partial \eta}+\Gamma^{22}\frac{\partial \phi}{\partial \xi}\right)=\sum_i D_i\phi_i \tag{3-70}$$

where i = *NW, N, NE, W, P, E, SW, S, SE;*

$$\frac{\partial}{\partial \eta}\left(Mp\right)+\frac{\partial}{\partial \xi}\left(Np\right)=\left(M_e p_e-M_w p_w\right)+\left(N_s p_s-N_n p_n\right) \tag{3-71}$$

where the coefficients D_i are given by

$$D_{NW} = 0.25\left(\Gamma_w^{12} + \Gamma_n{}^{12}\right) \tag{3-72}$$

$$D_N = 0.25\left(\Gamma_w^{12} - \Gamma_e{}^{12}\right) + \Gamma_n^{22} \tag{3-73}$$

$$D_{NE} = -0.25\left(\Gamma_e^{12} + \Gamma_n{}^{12}\right) \tag{3-74}$$

$$D_W = \Gamma_w^{11} + 0.25\left(\Gamma_n^{12} - \Gamma_s{}^{12}\right) \tag{3-75}$$

$$D_P = -\left(\Gamma_w^{11} + \Gamma_e{}^{11} + \Gamma_n^{22} + \Gamma_s^{22}\right) \tag{3-76}$$

$$D_E = \Gamma_e^{11} + 0.25\left(\Gamma_s^{12} - \Gamma_n{}^{12}\right) \tag{3-77}$$

$$D_{SW} = -0.25\left(\Gamma_w^{12} + \Gamma_s{}^{12}\right) \tag{3-78}$$

$$D_S = 0.25\left(\Gamma_e^{12} - \Gamma_w{}^{12}\right) + \Gamma_s^{22} \tag{3-79}$$

$$D_{SE} = 0.25\left(\Gamma_e^{12} + \Gamma_s{}^{12}\right) \tag{3-80}$$

All the parameters at the grid faces in the above equations can be interpolated from the two adjacent nodes.

Discretized equation

Substituting all the above discretized terms into Equation (3-56), we obtain the following 5-grid-point semi implicit discrete form of the equation:

$$A_P \phi_P{}^{n+1} = \sum_{i=N,W,E,S} A_i \phi_i^{n+1} + B^n \tag{3-81}$$

where

$$A_P = a\left[\frac{1.5}{J_P \Delta t} + \max\left(\widetilde{U}_e, 0\right) + \max\left(-\widetilde{U}_w, 0\right) + \max\left(\widetilde{V}_s, 0\right) + \max\left(-\widetilde{V}_n, 0\right)\right] - F \cdot D_p \tag{3-82}$$

$$A_N = E \cdot D_N + a \cdot \max\left(\widetilde{V}_n, 0\right) \tag{3-83}$$

$$A_W = E \cdot D_W + a \cdot \max\left(\widetilde{U}_w, 0\right) \tag{3-84}$$

$$A_E = E \cdot D_E + a \cdot \max\left(-\widetilde{U}_e, 0\right) \tag{3-85}$$

$$A_S = E \cdot D_S + a \cdot \max\left(-\widetilde{V}_s, 0\right) \tag{3-86}$$

$$B^n = S^n + S_c{}^n + S_d^n + S_t^n - b\left[\frac{\partial}{\partial \eta}(Mp) + \frac{\partial}{\partial \xi}(Np)\right] \tag{3-87}$$

$$\begin{aligned} S_c = & -0.5a\left[\left(\phi_P - \phi_W\right)\max\left(\widetilde{U}_e, 0\right) - \left(\phi_E - \phi_{EE}\right)\max\left(-\widetilde{U}_e, 0\right)\right] \\ & - 0.5a\left[-\left(\phi_W - \phi_{WW}\right)\max\left(\widetilde{U}_w, 0\right) + \left(\phi_P - \phi_E\right)\max\left(-\widetilde{U}_w, 0\right)\right] \\ & - 0.5a\left[\left(\phi_P - \phi_N\right)\max\left(\widetilde{V}_s, 0\right) - \left(\phi_S - \phi_{SS}\right)\max\left(-\widetilde{V}_s, 0\right)\right] \\ & - 0.5a\left[-\left(\phi_N - \phi_{NN}\right)\max\left(\widetilde{V}_n, 0\right) + \left(\phi_P - \phi_S\right)\max\left(-\widetilde{V}_n, 0\right)\right] \end{aligned} \tag{3-88}$$

$$S_d = E\left(D_{NW}\phi_{NW} + D_{NE}\phi_{NE} + D_{SW}\phi_{SW} + D_{SE}\phi_{SE}\right) \tag{3-89}$$

$$S_t = a\left(\frac{2\phi_P^n}{J_P^n \Delta t} - \frac{0.5\phi_P^{n-1}}{J_P^{n-1}\Delta t}\right) \tag{3-90}$$

The source terms S_c and S_d are taken from the discretized convection term and the diffusion term, respectively. In this way, we have a compact 5-grid-point equation system and the coefficients of the four neighboring grid variables are positive. The discretized equation is in a semi-implicit form since the source term and the pressure term are evaluated at the previous time step. The equation is also nonlinear since the coefficients of the variables are dependent on the variables.

3.5.2 Grid Scheme and Discretization of the Free Surface Boundary Conditions

Due to the following advantages, staggered grids are used in the numerical solution of the governing equations:

- It guarantees the strict energy conservation in the finite volume discretization so that smaller grid number can be used.
- The fluctuations in the solution (especially at the free surface) due to the central differencing of the first derivative terms are avoided.
- There is no need for the explicit boundary condition for pressure at the free surface.

In the staggered grid system, temperature, pressure and all the physical properties are defined at the center node of each cell, while velocity components u and v are defined at the cell faces, whose control volumes are half a grid staggered from those of p and T as shown in Figure 3-2. The staggered grid scheme, though it requires tedious interpolations of variables, is shown to be robust and efficient.

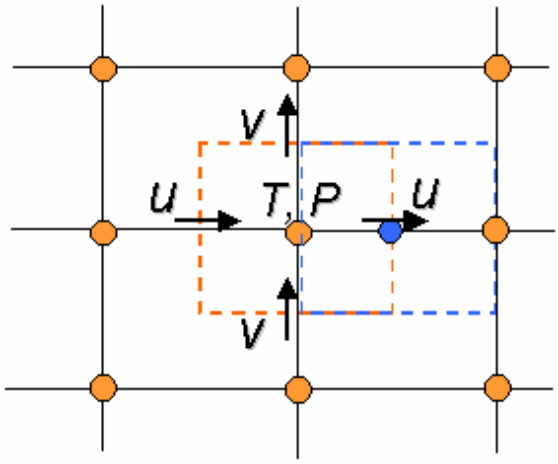

Figure 3-2 Staggered grid

In order to implement the free surface boundary conditions given by Equations (D-16) and (D-17) using the staggered grid, appropriate discretization and manipulation are required to ensure stable and robust convergence in the computation. Along the free surface, the faces of the boundary grids are aligned with the surface as shown in Figure 3-3. We define *u* at the surface and *v* half a grid away from the boundary. The first derivatives of the velocity components in Equations (D-16) and (D-17) need to be evaluated along the free surface. In order to maintain the 2nd order accuracy in the differencing, the glass domain is extended outward by half a grid size, and a fictitious *v* component is defined on the new boundary as shown in Figure 3-4 in dashed lines. The 2nd order accurate finite differencing can be implemented on the grey colored control volume right on the free surface with the grid molecules shown in Figure 3-4(a) as

$$\frac{\partial u}{\partial \eta} = 1.5u_P - 2u_W + 0.5u_{WW} \tag{3-91}$$

$$\frac{\partial u}{\partial \xi} = 0.5\left(u_S - u_N\right) \tag{3-92}$$

$$\frac{\partial v}{\partial \eta} = 0.5\left(v_{ne} + v_{se} - v_{nw} - v_{sw}\right) \tag{3-93}$$

$$\frac{\partial v}{\partial \xi} = 0.5\left(v_{sw} + v_{se} - v_{nw} - v_{ne}\right) \tag{3-94}$$

and with the grid molecules shown in Figure 3-4(b) as

$$\frac{\partial v}{\partial \eta} = \left(v_P - v_W\right) \tag{3-95}$$

$$\frac{\partial v}{\partial \xi} = 0.25\left(v_{SW} + v_S - v_{NW} - v_N\right) \tag{3-96}$$

$$\frac{\partial u}{\partial \eta} = 0.5\left(1.5u_n - 2u_{nw} + u_{nww} + 1.5u_s - 2u_{sw} + u_{sww}\right) \tag{3-97}$$

$$\frac{\partial \mathrm{u}}{\partial \xi} = \left(u_s - u_n\right) \tag{3-98}$$

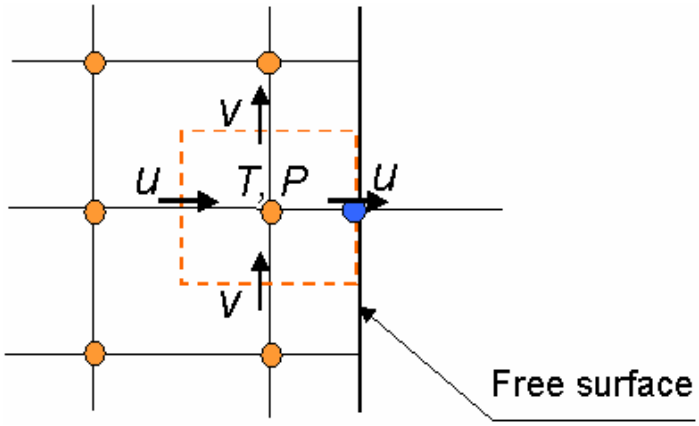

Figure 3-3 Boundary grid at the free surface

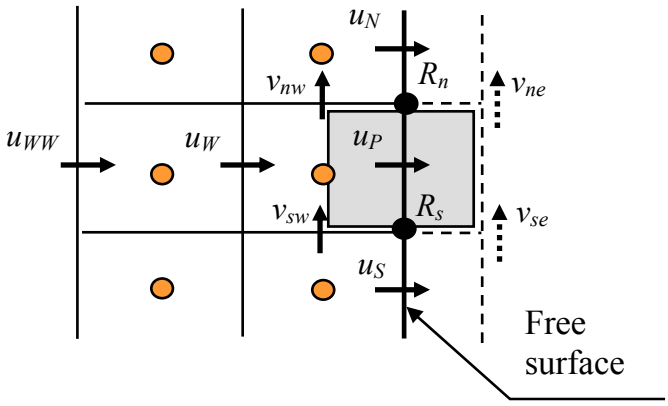

(a) control volume for u at the free surface

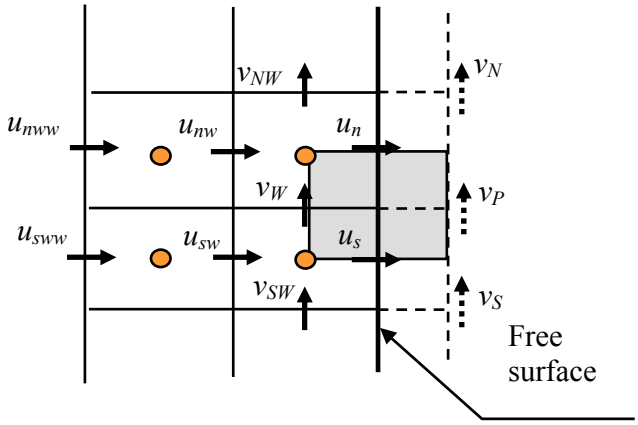

(b) control volume for v at the free surface

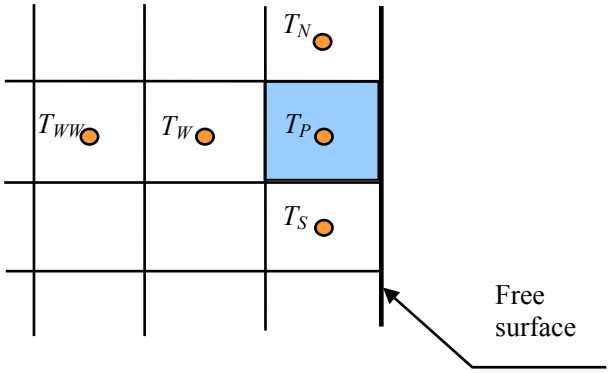

(c) control volume for T at the free surface

Figure 3-4 Grid molecules for the staggered grid at the free surface

Substituting Equations (3-91) ~ (3-94) into Equation (D-16), we obtain the following 5-grid-point equation for *u* after some manipulation:

$$\sum_i a_i u_i = S_{u,fs} + p, \qquad i = N, WW, W, P, S \tag{3-99}$$

where

$$a_N = -\mathrm{Re}^{-1}\,\mu \frac{g^{12}}{\sqrt{g^{11}}} n_{r,N} \tag{3-100}$$

$$a_{WW} = \mathrm{Re}^{-1}\,\mu \sqrt{g^{11}}\, n_{r,WW} \tag{3-101}$$

$$a_W = -4\,\mathrm{Re}^{-1}\,\mu \sqrt{g^{11}}\, n_{r,W} \tag{3-102}$$

$$a_P = 2\,\mathrm{Re}^{-1} \frac{\mu}{\sqrt{g^{11}}} \left(1.5 g^{11} n_{r,P} - B^n\right) \tag{3-103}$$

$$a_S = \mathrm{Re}^{-1}\,\mu \frac{g^{12}}{\sqrt{g^{11}}} n_{r,S} \tag{3-104}$$

$$\begin{aligned} S_{u,fs} = &-\mathrm{Re}^{-1} \frac{2\mu}{\sqrt{g^{11}}} \left\{ 0.5 g^{11} \left[(n_z v)_{ne} + (n_z v)_{se} - (n_z v)_{nw} - (n_z v)_{sw} \right] \right. \\ &+ 0.5 g^{12} \left[(n_z v)_{se} + (n_z v)_{sw} - (n_z v)_{ne} - (n_z v)_{nw} \right] \\ &\left. - 0.25 C^n \left(v_{ne} + v_{nw} + v_{se} + v_{sw} \right) \right\} + \mathrm{Re}^{-1}\, Ca^{-1} \zeta \kappa \end{aligned} \tag{3-105}$$

Substituting Equation (3-95) ~ (3-98) into Equation (D-17), we obtain the following 6-grid-point equation for *v* after some manipulation:

$$\sum_i a_i v_i = S_{v,fs}, \qquad i = NW, N, W, P, SW, S \tag{3-106}$$

where

$$a_{NW} = -0.25 g^{12} n_{r,NW} - 0.25 J n_{z,NW} \tag{3-107}$$

$$a_N = -0.25 g^{12} n_{r,N} - 0.25 J n_{z,N} \tag{3-108}$$

$$a_W = -g^{11} n_{r,W} - 0.5C^t \tag{3-109}$$

$$a_P = g^{11} n_{r,P} - 0.5C^t \tag{3-110}$$

$$a_{SW} = 0.25 g^{12} n_{r,SW} + 0.25 J n_{z,SW} \tag{3-111}$$

$$a_S = 0.25 g^{12} n_{r,S} + 0.25 J n_{z,S} \tag{3-112}$$

$$\begin{aligned} S_{v,fs} &= 0.25 g^{11} \left[3(n_z u)_n - 4(n_z u)_{nw} - (n_z u)_{nww} + 3(n_z u)_s - 4(n_z u)_{sw} - (n_z u)_{sww} \right] \\ &+ g^{12} \left[(n_z u)_s - (n_z u)_n \right] - J \left[(n_r u)_s - (n_r u)_n \right] + 0.5 B^t (u_s + u_n) \end{aligned} \tag{3-113}$$

The 2nd order accurate central and one-sided finite differencing is also applied to the derivative terms in Equation (D-18) using the control volume with the grid molecules shown in Figure 3-4(c). The following 5-grid-point equation is obtained for *T*:

$$\sum_i a_i T_i = S_{T,fs}, \qquad i = N, WW, W, P, S \tag{3-114}$$

where

$$a_N = -a_S = 0.5k \frac{g^{12}}{\sqrt{g^{11}}} \tag{3-115}$$

$$a_{WW} = -0.5k \sqrt{g^{11}} \tag{3-116}$$

$$a_W = -2k \sqrt{g^{11}} \tag{3-117}$$

$$a_P = 1.5k \sqrt{g^{11}} \tag{3-118}$$

$$S_{T,fs} = \frac{1}{q_m} \left(q_{rad,opa} + q_{conv} \right) \tag{3-119}$$

Care should also be taken in the discretization of the kinematic condition given by Equation (3-21) to avoid fluctuations in the solution of the free surface profile. Using the grid molecules shown in Figure 3-4(a), we discretize the spatial derivative term by

$$\frac{dR}{dz} = \frac{R_s - R_n}{\Delta z} \tag{3-120}$$

Note that the above central difference is obtained using every two adjacent discrete radii instead of every other two adjacent ones. This is the mechanism to avoid fluctuations in the solution. The time derivative term is discretized by the 2nd order one-sided differencing scheme. Defining $R_c = 0.5(R_s + R_n)$, the discrete form of Equation (3-21) is given by the 2-point equation

$$a_s R_s^{n+1} + a_n R_n^{n+1} = S_{R,fs} \tag{3-121}$$

where

$$a_s = \frac{0.75}{\Delta t} + \frac{0.25\left(v_{nw}^{n+1} + v_{ne}^{n+1} + v_{sw}^{n+1} + v_{se}^{n+1}\right)}{\Delta z} \tag{3-122}$$

$$a_s = \frac{0.75}{\Delta t} - \frac{0.25\left(v_{nw}^{n+1} + v_{ne}^{n+1} + v_{sw}^{n+1} + v_{se}^{n+1}\right)}{\Delta z} \tag{3-123}$$

$$S_{R,fs} = u_P^{n+1} + \frac{2R_c^n - 0.5R_c^{n-1}}{\Delta t} \tag{3-124}$$

The solution of Equation (3-121) only needs one boundary condition: $R(z = 0) = 1$.

3.5.3 Solution of the Navier-Stokes Equations

The solution of the momentum equations needs the evaluation of the pressure derivative terms. There is no explicit equation for the solution of pressure. The implicit

condition requires that the correct pressure field should be such that the velocity field satisfies the continuity equation. Proper algorithm is needed to solve the pressure-velocity coupled Navier-Stokes equations. In this study, we find the artificial compressibility method (ACM) (Chorin, 1967) are robust in solving the governing equations for the glass domain, while the pressure-implicit with splitting of operators (PISO) algorithm (Issa, 1985) is more effective for solving the governing equations for the air domain. We extend the application of the PISO algorithm to the solution of Navier-Stokes equations in the curvilinear coordinate system and on the staggered grids.

3.5.3.1 ACM for the Glass Domain

In the glass domain, the ACM is used to solve the pressure-velocity coupled equations. An artificial time derivative of the pressure is added to the continuity equation. The modified continuity equation in the curvilinear coordinate system is given by

$$\frac{\partial}{\partial \tilde{t}}\left(\frac{p}{J}\right)+\beta\left[\frac{\partial}{\partial \eta}\left(\frac{U}{J}\right)+\frac{\partial}{\partial \xi}\left(\frac{V}{J}\right)\right]=\beta S_p \tag{3-125}$$

where $\tilde{t}$ is the fictitious time, and β is the artificial compressibility factor that can be tuned to obtain the optimum convergence rate. The pressure field can then be explicitly solved by the standard time marching scheme using the above equation and the latest velocity field at each time step. The artificial term vanishes when the time marching iteration reaches the steady state so that the physical continuity equation is satisfied. Since we only need steady state solution, the physical time *t* in the momentum and energy equation is also replaced by the artificial time $\tilde{t}$.

3.5.3.2 PISO scheme for the Air Domain

ACM works well for the solution of the governing equations for the glass domain, but it is not a robust and efficient method for solving the mixed convection problem in the air domain. Instead, the method of PISO is shown to be more effective for the air domain. This method is similar to the popular SIMPLER method developed by Patankar (1980). The main feature of the technique is the splitting of the solution process into a series of steps whereby operations on pressure are decoupled from those on velocity at each step. The fields obtained at each time step are close approximations of the exact solution of the difference equations. Usually only two steps of splitting of operators are needed at each time step, which makes the method an efficient non-iterative algorithm. Since our governing equations are discretized in the curvilinear coordinate system on the staggered grid, the intermediate equation generated in the algorithm is quite complicated.

Predictor Step

At first, the pressure field at the latest time step t^n is used in Equation (3-81) to obtain u^+ and v^+, which are the first intermediate estimations of the velocity field at the next time step. The following equations are solved

$$u_P^+ = \frac{1}{A_P{}^u}\left[\sum_{i=N,W,E,S} A_i{}^u u_i^+ + S_u + S_c + S_d + S_t\right] - \frac{1}{A_P{}^u}\left[\frac{\partial}{\partial\eta}\left(M^u p^n\right) + \frac{\partial}{\partial\xi}\left(N^u p^n\right)\right] \qquad (3\text{-}126)$$

$$v_P^+ = \frac{1}{A_P{}^v}\left[\sum_{i=N,W,E,S} A_i{}^v v_i^+ + S_v + S_c + S_d + S_t\right] - \frac{1}{A_P{}^v}\left[\frac{\partial}{\partial\eta}\left(M^v p^n\right) + \frac{\partial}{\partial\xi}\left(N^v p^n\right)\right] \qquad (3\text{-}127)$$

where the superscript n denotes the current time step. Since the velocity components u and v are defined at different locations in the staggered grid as shown in Figure 3-2, we

use the superscript *u* and *v* to differentiate the coefficients evaluated at the corresponding locations.

First Corrector Step

We define u', v' and p' as the corrections to u^+, v^+ and p^n, respectively, then the new estimations of the velocity and pressure fields are given by:

$$u^{++} = u^+ + u^{'};\ v^{++} = v^+ + v^{'} \tag{3-128}$$

$$p^+ = p^n + p^{'} \tag{3-129}$$

An approximation of u' and v' can be derived using Equation (3-126) and (3-127).

$$u' = -\frac{1}{A_P{}^u}\left[\frac{\partial}{\partial\eta}\left(M^u p^{'}\right)+\frac{\partial}{\partial\xi}\left(N^u p^{'}\right)\right] \tag{3-130}$$

$$v' = -\frac{1}{A_P{}^v}\left[\frac{\partial}{\partial\eta}\left(M^v p^{'}\right)+\frac{\partial}{\partial\xi}\left(N^v p^{'}\right)\right] \tag{3-131}$$

On the other hand, u^{++} and v^{++} should satisfy the continuity equation, *i.e.*

$$\frac{\partial}{\partial\eta}\left(\frac{\rho U^{++}}{J}\right)+\frac{\partial}{\partial\xi}\left(\frac{\rho V^{++}}{J}\right)=S_p \tag{3-132}$$

Substituting the expression of U and V given by Equation (D-9) and (D-10) into the above equation and applying the central difference scheme to the differentiations on a control volume for pressure, we get the following equation:

$$\begin{aligned}&\left[\frac{\rho}{J}\left(\eta_r u^{++}+\eta_z v^{++}\right)\right]_e-\left[\frac{\rho}{J}\left(\eta_r u^{++}+\eta_z v^{++}\right)\right]_w\\&\left[\frac{\rho}{J}\left(\xi_r u^{++}+\xi_z v^{++}\right)\right]_s-\left[\frac{\rho}{J}\left(\xi_r u^{++}+\xi_z v^{++}\right)\right]_n=S_p\end{aligned} \tag{3-133}$$

Substituting Equations (3-128) ~ (3-131) into the above equation and applying the central differencing to the pressure derivative terms, we obtain the following 9-grid-poiont discrete Poisson equation for p' after some manipulations:

$$\sum_i a_i p_i^{'} = -\left[\left(\frac{\rho U^+}{J}\right)_e - \left(\frac{\rho U^+}{J}\right)_w + \left(\frac{\rho V^+}{J}\right)_s - \left(\frac{\rho V^+}{J}\right)_n\right] + S_p \qquad (3\text{-}134)$$
$$i = NW, N, NE, W, P, E, SW, S, SE$$

where the coefficients for the pressure at the central node and 8 neighboring grid points as shown in Figure 3-1 are given by

$$a_{NW} = 0.25\frac{\rho_w}{A_{P,w}}\left(z_{\xi,w}z_{\eta,NW} + r_{\xi,w}r_{\eta,NW}\right) + 0.25\frac{\rho_n}{A_{P,n}}\left(z_{\eta,n}z_{\xi,NW} + r_{\eta,n}r_{\xi,NW}\right) \qquad (3\text{-}135)$$

$$\begin{aligned} a_N = &-\frac{\rho_n}{A_{P,n}}\left(z_{\eta,n}z_{\eta,N} + r_{\eta,n}r_{\eta,N}\right) - 0.25\frac{\rho_e}{A_{P,e}}\left(z_{\xi,e}z_{\eta,N} + r_{\xi,e}r_{\eta,N}\right) \\ &+ 0.25\frac{\rho_w}{A_{P,w}}\left(z_{\xi,w}z_{\eta,N} + r_{\xi,w}r_{\eta,N}\right) \end{aligned} \qquad (3\text{-}136)$$

$$a_{NE} = -0.25\frac{\rho_e}{A_{P,e}}\left(z_{\xi,e}z_{\eta,NE} + r_{\xi,e}r_{\eta,NE}\right) - 0.25\frac{\rho_n}{A_{P,n}}\left(z_{\eta,n}z_{\xi,NE} + r_{\eta,n}r_{\xi,NE}\right) \qquad (3\text{-}137)$$

$$\begin{aligned} a_W = &-\frac{\rho_w}{A_{P,w}}\left(z_{\xi,w}z_{\xi,W} + r_{\xi,w}r_{\xi,W}\right) - 0.25\frac{\rho_s}{A_{P,s}}\left(z_{\eta,s}z_{\xi,W} + r_{\eta,s}r_{\xi,W}\right) \\ &+ 0.25\frac{\rho_n}{A_{P,n}}\left(z_{\eta,n}z_{\xi,W} + r_{\eta,n}r_{\xi,W}\right) \end{aligned} \qquad (3\text{-}138)$$

$$\begin{aligned} a_P = &\frac{\rho_e}{A_{P,e}}\left(z_{\xi,e}z_{\xi,P} + r_{\xi,e}r_{\xi,P}\right) + \frac{\rho_w}{A_{P,w}}\left(z_{\xi,w}z_{\xi,P} + r_{\xi,w}r_{\xi,P}\right) \\ &+ \frac{\rho_s}{A_{P,s}}\left(z_{\eta,s}z_{\eta,P} + r_{\eta,s}r_{\eta,P}\right) + \frac{\rho_n}{A_{P,n}}\left(z_{\eta,n}z_{\eta,P} + r_{\eta,n}r_{\eta,P}\right) \end{aligned} \qquad (3\text{-}139)$$

$$a_E = -\frac{\rho_e}{A_{P,e}}\left(z_{\xi,e}z_{\xi,E} + r_{\xi,e}r_{\xi,E}\right) + 0.25\frac{\rho_s}{A_{P,s}}\left(z_{\eta,s}z_{\xi,E} + r_{\eta,s}r_{\xi,E}\right) - 0.25\frac{\rho_n}{A_{P,n}}\left(z_{\eta,n}z_{\xi,E} + r_{\eta,n}r_{\xi,E}\right) \tag{3-140}$$

$$a_{SW} = -0.25\frac{\rho_w}{A_{P,w}}\left(z_{\xi,w}z_{\eta,SW} + r_{\xi,w}r_{\eta,SW}\right) - 0.25\frac{\rho_s}{A_{P,s}}\left(z_{\eta,s}z_{\xi,SW} + r_{\eta,s}r_{\xi,SW}\right) \tag{3-141}$$

$$a_S = -\frac{\rho_s}{A_{P,s}}\left(z_{\eta,s}z_{\eta,S} + r_{\eta,s}r_{\eta,S}\right) + 0.25\frac{\rho_e}{A_{P,e}}\left(z_{\xi,e}z_{\eta,S} + r_{\xi,e}r_{\eta,S}\right) - 0.25\frac{\rho_w}{A_{P,w}}\left(z_{\xi,w}z_{\eta,S} + r_{\xi,w}r_{\eta,S}\right) \tag{3-142}$$

$$a_{SE} = 0.25\frac{\rho_e}{A_{P,e}}\left(z_{\xi,e}z_{\eta,SE} + r_{\xi,e}r_{\eta,SE}\right) + 0.25\frac{\rho_s}{A_{P,s}}\left(z_{\eta,s}z_{\xi,SE} + r_{\eta,s}r_{\xi,SE}\right) \tag{3-143}$$

In the staggered grid, one face of each boundary control volume is aligned with the solid boundaries along the glass free surface or the furnace wall. The same type of discrete Poisson equation for pressure can be derived at these boundary control volumes except that some of the pressure derivative terms in Equations (3-130) and (3-131) have to be discretized by one-sided finite differencing so that all the grid points associated with the Poisson equation are within the computation domain.

Equation (3-134) together with the boundary equations are solved to obtain p', which is then substituted into Equations (3-130) and (3-131) to get u' and v'. The velocity and pressure fields can now be updated by Equations (3-128) and (3-129). Note that u^{++} and v^{++} satisfy the continuity equation.

Second Corrector Step

We define u'', v'' and p'' as the further corrections to u^{++}, v^{++} and p^{+}, respectively, then the new estimations of the velocity field and the pressure field can be given by:

$$u^{+++} = u^{++} + u''; \; v^{+++} = v^{++} + v'' \tag{3-144}$$

$$p^{++} = p^{+} + p'' \tag{3-145}$$

An approximation of u'' and v'' can be derived using Equation (3-126) and (3-127).

$$u'' = \sum_{i=N,W,E,S} \frac{A_i^u}{A_P^u} u_i' - \frac{1}{A_P^u}\left[\frac{\partial}{\partial \eta}\left(M^u p''\right) + \frac{\partial}{\partial \xi}\left(N^u p''\right)\right] \tag{3-146}$$

$$v'' = \sum_{i=N,W,E,S} \frac{A_i^v}{A_P^v} v_i' - \frac{1}{A_P^v}\left[\frac{\partial}{\partial \eta}\left(M^v p''\right) + \frac{\partial}{\partial \xi}\left(N^v p''\right)\right] \tag{3-147}$$

Since both (u^{+++}, v^{+++}) and (u^{++}, v^{++}) satisfy the continuity equation, (u'', v'') should satisfy the following equation

$$\frac{\partial}{\partial \eta}\left(\frac{\rho U''}{J}\right) + \frac{\partial}{\partial \xi}\left(\frac{\rho V''}{J}\right) = 0 \tag{3-148}$$

Substituting Equations (3-146) and (3-147) into the above equation, we obtain another 9-grid-point discrete Poisson equation:

$$\sum_i a_i p_i'' = -\left[\left(\frac{\rho \hat{U}'}{J}\right)_e - \left(\frac{\rho \hat{U}'}{J}\right)_w + \left(\frac{\rho \hat{V}'}{J}\right)_s - \left(\frac{\rho \hat{V}'}{J}\right)_n\right] \tag{3-149}$$
$$i = NW, N, NE, W, P, E, SW, S, SE$$

where $\hat{U}'$ and $\hat{V}'$ are constructed by $\hat{u}'$ and $\hat{v}'$, and

$$\hat{u}' = \sum_{i-N,W,E,S} \frac{A_i^u}{A_P^u} u_i' \; ; \quad \hat{v}' = \sum_{i-N,W,E,S} \frac{A_i^v}{A_P^v} v_i' \tag{3-150}$$

The coefficients a_i in Equation (3-149) are given by Equations (3-135) ~ (3-143).

Equation (3-149) together with the similarly derived boundary equations are solved to obtain p'', which is then substituted into Equations (3-146) and (3-147) to get

u'' and v''. The velocity and pressure fields can now be updated by Equation (3-144) and (3-145). This complete the splitting process at which stage the u^{+++}, v^{+++} and p^{++} fields are taken to stand for the exact solution of u^{n+1}, v^{n+1} and p^{n+1}.

3.5.4 Computation Algorithm

The solution of the conjugate problem of the fiber drawing process is challenging since it requires the simultaneous solution of the governing equations in both the glass and the air domains as well as the radiative transfer and the enclosure analysis. Furthermore, the free interface between the glass and the air is unknown. Multiple loops of iterations are needed to obtain the numerical solution, which makes the convergence of the computation challenging.

The degree of freedoms (unknown variables) during the computation iterations can be effectively reduced by decoupling the temperature iteration and the free surface iteration. Based on this idea, the following computation procedures turn out to be efficient and robust in solving the steady state free surface profile, the velocity and temperature fields of the glass and the air. Two procedures are presented: one is for the complete 2-D model; the other is for the semi 2-D model.

Computational Procedure for the Complete 2-D Model

In this computational procedure, 2-D models are used for all the thermo-fluid transports in both the glass and the air domains.

Step 1: Input the assumed initial free surface profile $R(z)$ and the values of the primitive variables (p, u, v, T).

Step 2: Conjugate temperature iteration (with a given free surface and the glass velocity distribution).

(a) Calculate all the view factors.

(b) Solve the 2-D governing equations for the mixed convection problem in the air domain using the PISO algorithm, and then calculate the convective heat flux along the free interface by $q_{conv} = -k_a \left.\frac{\partial T}{\partial n}\right|_a$.

(c) Solve the RTE using the FVM; at the same time, obtain the furnace radiosities through the enclosure analysis. Iteration is needed for the intensities along the free interface.

(d) Calculate $\nabla \cdot \mathbf{q}_R$ using the intensities solved in the last step.

(e) Solve the 2-D glass energy equation using the implicit time marching scheme.

(f) Repeat Step 2(c) until a steady state solution of the glass temperature is reached.

(g) Repeat Step 2(b) until the glass temperature does not vary between two consecutive iterations in this step.

Step 3: Free surface and velocity field computation (with the given glass temperature field obtained in Step 2).

(a) Calculate the glass viscosity using the temperature field solved in Step 2.

(b) Use the velocity and pressure fields in the last time step as the initial estimation of the fields in the current time step; then use the initial or intermediate estimation of the fields in evaluating the nonlinear coefficients and source terms in Equation (3-81).

(c) Solve the 5-grid-point discrete equations for *u* and *v*.

(d) Using the intermediate velocity field obtained in Step 3(c), explicitly update the pressure field by Equation (3-125).

(e) Go back to Step 3(b) until the velocity field does not vary between two consecutive iterations in this step.

(f) After the current time step velocity field is obtained, update the free surface profile using the kinematic condition given by Equation (3-121) in the discrete form.

(g) Regenerate the 2-D curvilinear grid using the updated free surface profile.

(h) Assign the new velocity and pressure field to the old time step variables, and then go back to Step 3(b) to calculate the fields in a new time step until the solution shows that the steady state has been reached.

Step 4: Go back to Step 2 until the relative change between two consecutive computed free surface profiles at Step 4 is less than 10^{-5}.

Computational Procedure for the Semi 2-D Model

In this computational procedure, 2-D models are still used in solving the thermal-fluid transport in the air domain and the thermal transport in the glass domain, while the 1-D glass flow model developed in Section 3.4 is used for free surface and glass velocity calculation.

Step 1: Input the assumed initial free surface profile R(z) and the values of the primitive variables v(z) and T(r, z) for glass.

Step 2: Conjugate temperature iteration (with a given free surface and the glass velocity distribution).

(a) Neglecting the radial variation of $v(z)$, the radial component of velocity is obtained by $u = -0.5r\dfrac{dv}{dz}$ so that the 2-D continuity equation $\dfrac{1}{r}\dfrac{\partial(ru)}{\partial r} + \dfrac{\partial v}{\partial z} = 0$ is satisfied.

(b) Calculate the view factors.

(c) Solve the 2-D governing equations for the mixed convection problem in the air domain using the PISO algorithm, and then calculate the convective heat flux along the free interface by $q_{conv} = -k_a \left.\frac{\partial T}{\partial n}\right|_a$.

(d) Solve the RTE using the FVM; at the same time, obtain the furnace radiosities through the enclosure analysis. Iteration is needed for the intensities along the free interface.

(e) Calculate $\nabla \cdot \mathbf{q}_R$ using the intensities solved in the last step.

(f) Solve the glass energy equation using implicit time marching scheme.

(g) Repeat Step 2(d) until a steady state solution of the glass temperature is reached.

(h) Repeat Step 2(c) until the glass temperature does not vary between two consecutive iterations at this step.

Step 3: Free surface computation (with the temperature field $T(r,z)$ obtained in Step 2).

(a) Calculate the glass viscosity using the radially lumped temperature given by $\overline{T}(z) = \frac{2}{R^2(z)} \int_0^{R(z)} T(r,z) r dr$.

(b) Calculate 1-D glass velocity distribution $v(z)$ using Equation (3-50).

(c) Update the free surface profile using Equation (3-55).

(d) Repeat Step 3(b) until the free surface profile does not change between two consecutive iterations.

Step 4: Regenerate the 2D curvilinear grid, and then repeat Step 2 until the relative change between two consecutive computed free surface profiles at Step 4 is less than 10^{-5}.

CHAPTER IV

REDUCED ORDER MODELING AND ROBUST CONTROL

4.1 Overview

In the previous chapters, we have developed the computational models for the thermal-fluid transports in the fiber drawing system, which can be used for design optimizations. In this chapter, we develop a reduced order dynamic model on the basis of the computational models and then design a robust controller using the ROM. A quasi 1-D fluid dynamic model is developed first. The PDE's are then linearized around the steady state solution obtained from the 2-D CFD model. Karhunen-Loeve (K-L) decomposition is applied to the transient simulation data obtained using the CFD model to obtain a set of optimal numerical eigenfunctions corresponding to the most typical structures of the transient response. The empirical eigenfunctions are then used as the basis functions in the Galerkin's procedure on the linear PDE's to obtain the ROM. Finally, the ROM is written in a state space form, and a mixed H_∞/LQG controller is designed, which not only minimizes the H_2 norm but also reduces the H_∞ norm of the closed-loop system to less than a small constant.

4.2 Quasi 1-D Fluid Dynamic Model

As will be shown in Chapter V that the glass velocity and temperature distributions are approximately 1-D in axial direction in the neck-down region for the large preforms up to 8cm in diameter. Furthermore, as the goal of a close-loop control system is to meet the control objective, the model used for the controller design is not

required to be as accurate as the one used for variable prediction and analysis. Hence, we use a quasi 1-D fluid dynamic model in deriving the reduced order model that will be used in the control design. This greatly simplifies the modeling process and reduces the computational cost.

For the system shown in Figure 1-2, the regulated outputs are the fiber diameter and tension; the manipulating inputs are the draw speed, the feed-rate, and the furnace irradiation. The draw dynamics of the free surface flow are characterized using the following three coupled distributed state variables: $a = \pi R^2$ (the glass cross-sectional area of radius R), the glass axial velocity v, and the glass temperature T. Using the characteristic quantities given by Equation (3-6), the dimensionless dynamic equations (where the asterisks are dropped for ease of presentation) for the 1-D conservation of mass, momentum and energy are given by:

$$\frac{\partial a}{\partial t} + \frac{\partial}{\partial z}(av) = 0 \tag{4-1}$$

$$\rho\left[\frac{\partial(av)}{\partial t} + \frac{\partial(av^2)}{\partial z}\right] = \frac{1}{\mathrm{Re}}\frac{\partial}{\partial z}\left[3a\mu(T)\frac{\partial v}{\partial z}\right] + \frac{1}{Fr}a \tag{4-2}$$

$$\rho C_p\left[\frac{\partial(aT)}{\partial t} + \frac{\partial(avT)}{\partial z}\right] = \frac{1}{Pe}\frac{\partial}{\partial z}\left[a\tilde{k}(T)\frac{\partial T}{\partial z}\right] - \frac{2\pi R}{q_{m2}\mathbf{n}\cdot\mathbf{r}}\left(q''_{rad} + q''_{conv}\right) + 3\frac{Ec}{\mathrm{Re}}a\mu(T)\left(\frac{\partial v}{\partial z}\right)^2 \tag{4-3}$$

where g is the gravity acceleration; $\tilde{k}$ is the glass apparent conductivity; $q_{m2} = \rho C_p T_m v_f$ is used to nondimensionalize the heat flux terms; **n** and **r** are the unit normal and radial vectors at the free surface respectively. The elongational model for the normal stress, $\sigma_{zz} = 3\mu\partial v / \partial z$, has been used in deriving Equation (4-2).

The net radiation heat flux leaving the glass surface is given by

$$q''_{rad} = \widetilde{\varepsilon}_g \left(\widetilde{E}_b - \widetilde{H} \right) \tag{4-4}$$

where $\widetilde{\varepsilon}_g$ is the apparent glass emissivity which can be obtained using the correlation given by Myers (1989); $\widetilde{E}_b$ is the apparent blackbody emissive power given by σT^4 (σ is the Stefan-Boltzmann constant); and $\widetilde{H}$ is the apparent irradiation. Since the glass does not have physical emissivity and surface emission at the semitransparent band, the above apparent variables only represent an approximate characteristics of the radiation heat flux. The steady state values of the above apparent variables can be obtained from the 2-D numerical solution of the radiation heat flux and the glass temperature. In obtaining the apparent variables, q''_{rad} is calculated by $q''_{rad} = \int_0^\infty (J_\lambda - H_\lambda) d\lambda$ where H_λ is given by Equations (2-23); and J_λ at two different bands are given by Equations (2-15) and (2-16).

The air convective heat flux at the glass surface is given by

$$q''_{conv} = h(T - T_a) \tag{4-5}$$

where h is the convective heat transfer coefficient and T_a is the radially lumped air temperature. Both h and T_a can be obtained from the 2-D numerical solution of the air temperature field using the model presented in the last chapter.

We model the radiative transfer in the axial direction in the form of a Rosseland conductivity:

$$\widetilde{k} = k + \frac{16 n_g^2 \sigma T^3}{3 \widetilde{\kappa}_R} \tag{4-6}$$

where k is the molecular conductivity; and n_g is the average index of refraction of the glass. In Equation (4-6), the apparent absorption coefficient $\widetilde{\kappa}_R$ accounts for the fact that

the media is not optically thick, which can be obtained using the steady-state radiative flux and the temperature field solved from the 2-D CFD model presented in the previous chapters.

The boundary conditions of the quasi 1-D model are

$$\text{at } z = 0 \qquad a = 1, v = v_i = \frac{v_p}{v_f}, \frac{\partial^2 T}{\partial z^2} = 0 \tag{4-7}$$

$$\text{at } z = L_f + L_p \qquad v = v_o = 1, \frac{\partial^2 T}{\partial z^2} = 0 \tag{4-8}$$

where v_i and v_o are the dimensionless feed rate and draw speed, respectively.

4.3 Reduced Order Model (ROM)

The procedure for deriving the ROM is as follows: The quasi1-D CFD model is linearized around the steady state solution obtained from the full-2D model. The K-L expansion is applied to the CFD simulated data to obtain numerical eigenfunctions for each distributed state variable. Finally, the ROM is obtained by applying the Galerkin's method to the linear PDE's using the smallest number of basis functions.

4.3.1 Linear PDE's

To linearize the nonlinear system given by Equations (4-1) to (4-3), the distributed state variables are written as the superposition of their steady state values ($\bar{a}$, $\bar{v}$ and $\bar{T}$) and the dimensionless perturbations (a', v' and T'):

$$a(z,t) = \bar{a}(z)[1 + a'(z,t)] \tag{4-9}$$

$$v(z,t) = \bar{v}(z)[1 + v'(z,t)] \tag{4-10}$$

$$T(z,t) = \overline{T}(z)[1 + T'(z,t)] \tag{4-11}$$

As the transient temperature variation in response to the small magnitude of disturbances are small, the nonlinear dependence of $\mu(T)$, $\widetilde{k}(T)$ and $\widetilde{E}(T)$ on temperature can be approximated as the following linear relations

$$\mu(T) = \mu(\overline{T}) + \left.\frac{d\mu}{dT}\right|_{\overline{T}} \overline{T}T' \tag{4-12}$$

$$\widetilde{k}(T) = \widetilde{k}(\overline{T}) + \left.\frac{d\widetilde{k}}{dT}\right|_{\overline{T}} \overline{T}T' \tag{4-13}$$

$$\widetilde{E}(T) = \widetilde{E}(\overline{T}) + \left.\frac{d\widetilde{E}}{dT}\right|_{\overline{T}} \overline{T}T' \tag{4-14}$$

Garner (2000) has shown experimentally that the furnace temperature profiles are relatively similar in shape when the setting of the maximum furnace temperature is changed. Therefore, the irradiation from the furnace can be approximately written as

$$\widetilde{H}(z,t) = (1 + q'(t))\overline{H}(z) \tag{4-15}$$

where $q'(t)$ is the dimensionless perturbation of the irradiation which can be controlled by the electrical current input to the furnace, and $\overline{H}(z)$ is the steady state spatial distribution of the irradiation at the nominal setting.

The main source of the high frequency disturbances that we need to deal with is the fluctuation of the air convective heat flux at the free surface. We treat this disturbance as the perturbation to the convective heat transfer coefficient as follows:

$$h(z,t) = \bar{h}(z)\left[1 + h'(t)\right] \tag{4-16}$$

where $\bar{h}$ is the steady state value and h' is the dimensionless perturbation.

Substituting Equations (4-9) ~ (4-16) into Equations (4-1) ~ (4-3) and only retaining the first order terms, we obtain the following linear PDE's

$$\frac{\partial}{\partial t}\left(\bar{a}a'\right) + \frac{\partial}{\partial z}\left(\bar{a}\bar{v}a'\right) + \frac{\partial}{\partial z}\left(\bar{a}\bar{v}v'\right) = 0 \tag{4-17}$$

$$\begin{aligned} &\bar{a}\bar{v}\left(\frac{\partial a'}{\partial t} + \frac{\partial v'}{\partial t}\right) + \frac{\partial}{\partial z}\left[\bar{a}\bar{v}^2\left(a' + 2v'\right)\right] \\ &= \frac{3}{\mathrm{Re}}\frac{\partial}{\partial z}\left[\bar{a}\bar{\mu}\frac{\partial \bar{v}}{\partial z}\left(a' + \frac{\partial v'}{\partial z}\right) + \bar{a}\frac{\partial \bar{v}}{\partial z}\frac{d\mu}{dT}\Big|_{\bar{T}}\bar{T}T'\right] + \frac{1}{Fr}\bar{a}a' \end{aligned} \tag{4-18}$$

$$\begin{aligned} &\bar{a}\bar{T}\frac{\partial}{\partial t}\left(a' + T'\right) + \frac{\partial}{\partial z}\left[\bar{a}\bar{v}\bar{T}\left(a' + v' + T'\right)\right] \\ &= \frac{1}{Pe}\frac{\partial}{\partial z}\left[\bar{a}\bar{k}\frac{\partial \bar{T}}{\partial z}\left(a' + \frac{\partial T'}{\partial z}\right) + \bar{a}\frac{\partial \bar{T}}{\partial z}\frac{d\tilde{k}}{dT}\Big|_{\bar{T}}\bar{T}T'\right] \\ &- \frac{2\pi R}{q_{m2}\mathbf{n}\cdot\mathbf{r}}\left[\left(\frac{d\tilde{E}}{dT}\Big|_{\bar{T}} + \bar{h}\right)\bar{T}T' + \left(\bar{T} - T_a\right)h'\right] \\ &+ \frac{2\pi R}{q_{m2}\mathbf{n}\cdot\mathbf{r}}\tilde{\varepsilon}\bar{H}q' + \frac{3Ec}{\mathrm{Re}}\left[\bar{a}\bar{\mu}\left(\frac{\partial \bar{v}}{\partial z}\right)^2\left(a' + 2\frac{\partial v'}{\partial z}\right) + \bar{a}\left(\frac{\partial \bar{v}}{\partial z}\right)^2\frac{d\mu}{dT}\Big|_{\bar{T}}\bar{T}T'\right] \end{aligned} \tag{4-19}$$

4.3.2 Karhunen-Loeve Expansion

The state variables $a'(z, t)$, $v'(z, t)$ and $T'(z, t)$ in the linear PDE's are distributed parameters and thus infinite dimensional. In order to obtain finite order models formed by ordinate differential equations (ODE's), it is necessary to discretize the PDE's. The lowest possible order of the distributed system model can be achieved by using the optimal (empirical or numerical) eigenfunctions through the K-L decomposition. For this purpose, we obtain a sufficient large set (ensemble) of snapshots which are the distributed

state variables sampled during the transient responses to all the possible manipulating inputs and the disturbances. The manipulating inputs to the system are v_i', v_o', and q'. These inputs may also be superposed by small magnitude of disturbances from the actuators. The fluctuation of h' is one of the main sources of high frequency disturbances. Assuming that the arbitrary input to the system may be represented as Fourier series, i.e. linear combination of sinusoidal functions with frequencies up to the bandwidth ($\omega_{\max}$) of the system to that input, we simulate the transient responses to each input at both its lowest frequency (step input) and highest frequency (sinusoidal input at $\omega_{\max}$) using the quasi 1-D CFD model. In sampling the snapshots during the simulations, shorter sampling periods are used for steep responses while longer periods are used for slow responses. Unlike the trigonometric or other mathematical functions, the numerical eigenfunctions obtained using the simulation data of the physical model have embedded physical characteristics and satisfy the boundary conditions automatically.

The manipulated inputs $v_i'(t)$ and $v_o'(t)$ are the boundary values of the velocity perturbation. In order to explicitly involve these inputs in the system equations as required by control models, the following variable is defined

$$\hat{v}(z,t) = v'(z,t) - \frac{\bar{v}'_{\alpha_o}(z)}{\alpha_o} v_o'(t) - \frac{\bar{v}'_{\alpha_i}(z)}{\alpha_i} v_i'(t) \tag{4-20}$$

where $\bar{v}'_{\alpha_o}$ and $\bar{v}'_{\alpha_i}$ are the stead state responses of v' to the step input of $v_o' = \alpha_o$ and $v_i' = \alpha_i$, respectively; and α_o and α_i are two small constants. Note that $\hat{v}$ satisfies homogeneous boundary conditions.

The snapshots for each state variable of a', $\hat{v}$ and T' form an ensemble represented as $\{u_n(z)\}$, where n = 1, 2, …, N and N is the total number of snapshots obtained in the simulations for all the inputs. The numerical eigenfunction $\phi(z)$ should represent the most typical characteristic structure among the snapshots. This is equivalent to obtaining a function $\phi(z)$ which minimizes the following objective function

$$J = \langle (\phi(z) - u_n(z), \phi(z) - u_n(z)) \rangle \tag{4-21}$$

where $\langle \cdot \rangle$ is the ensemble average given by $\langle x_n \rangle = 1/N \sum_{n=1}^{N} x_n$, and $(\cdot,\cdot)$ is the inner product in the spatial domain given by $(x, y) = \int_0^L x(z) y(z) dz$. The minimization of the cost function in Equation (4-21) is mathematically equivalent to maximize the ensemble average of the inner product between $\phi(z)$ and $u_n(z)$, i.e.

$$\text{Maximize } J = \frac{\left\langle (\phi, u_n)^2 \right\rangle}{(\phi, \phi)} \tag{4-22}$$

where the cost function is normalized to make the solution unique. The cost function can be rewritten as

$$\begin{aligned} \left\langle (\phi, u_n)^2 \right\rangle &= \left\langle \int_0^{L_t} \phi(z) u_n(z) dz \int_0^{L_t} \phi(z') u_n(z') dz' \right\rangle \\ &= \int_0^{L_t} \left[\int_0^{L_t} \langle u_n(z) u_n(z') \rangle \phi(z) dz \right] \phi(z') dz' \\ &= \int_0^{L_t} [\mathbf{R}\phi(z)] \phi(z') dz' \\ &= (\mathbf{R}\phi, \phi) \end{aligned} \tag{4-23}$$

where the linear operator **R** is defined as $\mathbf{R}\phi(z) = \int_0^L \langle u_n(z) u_n(z') \rangle \phi(z) dz$. It follows that the maximization problem of Equation (4-22) is reduced to the following eigenvalue problem

$$\mathbf{R}\phi = \lambda\phi \tag{4-24}$$

and the function that maximizes *J* of Equation (4-22) is the eigenfunction of Equation (4-24) corresponding to the largest eigenvalue.

An efficient way to solve the above integral equation is provided by the method of snapshots (Sirovich, 1987), where the eigenfunction is approximated as a linear combination of the snapshots as follows

$$\phi(z) = \sum_{n=1}^{N} c_n u_n(z) \tag{4-25}$$

Substituting this into Equation (4-24) yields

$$\mathbf{Bc} = \lambda\mathbf{c} \tag{4-26}$$

where the entry of matrix **B** is

$$B^{\kappa k} := \frac{1}{N} \int_0^L u_\kappa(z) u_k(z) dz \tag{4-27}$$

The elements of the eigenvector $\mathbf{c} = [c_1 \quad \ldots \quad c_N]^T$ are used in Equation (4-25) to construct the eigenfunction $\phi(z)$. If we put the order of the magnitude of the eigenvalues as $\lambda_1 > \lambda_2 > \ldots > \lambda_N$ and the corresponding eigenfunctions are $\phi_1, \phi_2, \ldots, \phi_N$, then ϕ_1 represent the most typical structure of the snapshot ensemble and ϕ_2 is the next typical structure, and so forth.

4.3.3 Galerkin Discretization

Using the numerical eigenfunctions obtained in the last section, we can map the distributed state variables to the spectral coefficients in the linear combination of eigenfunctions as follows:

$$a'(z,t) = \sum_{i=1}^{K_a} x_{ai}(t)\phi_{ai}(z) \tag{4-28}$$

$$v'(z,t) = \sum_{i=1}^{K_v} x_{vi}(t)\phi_{vi}(z) + \frac{\bar{v}'_{\alpha_o}(z)}{\alpha_o} v'_o(t) + \frac{\bar{v}'_{\alpha_i}(z)}{\alpha_i} v'_i(t) \tag{4-29}$$

$$T'(z,t) = \sum_{i=1}^{K_T} x_{Ti}(t)\phi_{Ti}(z) \tag{4-30}$$

where ϕ_a, ϕ_v and ϕ_T are the eigenfunctions obtained using the snapshots of a', $\hat{v}$ and T', respectively; K_a, K_v and K_T are the number of eigenfunctions retained in the expansion for a', $\hat{v}$ and T', respectively; and x_a, x_v, and x_T are the spectral coefficients in the linear mapping of each distributed state variable. Equation (4-29) is obtained by substituting $\hat{v}(z,t) = \sum_{i=1}^{K_v} x_{vi}(t)\phi_{vi}(z)$ into Equation (4-20) and rearranging the equation.

Equations (4-28) ~ (4-30) are substituted into Equation (4-17) ~ (4-19). Both sides of the resulted continuity equation are multiplied by each of the K_a eigenfunctions ϕ_a and are integrated in the spatial domain. K_a ordinary differential equations (ODE's) are obtained in this Galerkin procedure (Fletcher, 1984). Similarly, K_v and K_T ODE's are obtained from the resulted momentum equation and energy equation, respectively. The linear ODE's with a total number of $K = K_a + K_v + K_T$ are given by

$$\sum_{i=1}^{K_a} M_{a,ik}\dot{x}_{ai} = \sum_{i=1}^{K_a} E_{a,ik}x_{ai} + \sum_{i=1}^{K_v} F_{a,ik}x_{vi} + H_{a,k}v_o' + S_{a,k}v_i' \tag{4-31}$$

$$k = 1, 2, ..., K_a$$

$$\sum_{i=1}^{K_a} M_{v,ik}\dot{x}_{ai} + \sum_{i=1}^{K_v} L_{ik}\dot{x}_{vi} = \sum_{i=1}^{K_a} E_{v,ik}x_{ai} + \sum_{i=1}^{K_v} F_{v,ik}x_{vi} + \sum_{i=1}^{K_T} G_{v,ik}x_{Ti} + H_{v,k}v_o' + S_{v,k}v_i' + R_k\dot{v}_o' + W_k\dot{v}_i' \tag{4-32}$$

$$k = 1, 2, ..., K_v$$

$$\sum_{i=1}^{K_a} M_{T,ik}\dot{x}_{ai} + \sum_{i=1}^{K_T} I_{ik}\dot{x}_{Ti} = \sum_{i=1}^{K_a} E_{T,ik}x_{ai} + \sum_{i=1}^{K_v} F_{T,ik}x_{vi} + \sum_{i=1}^{K_T} G_{T,ik}x_{Ti} + H_{T,k}v_o' + S_{T,k}v_i' + T_k q' + U_k h' \tag{4-33}$$

$$k = 1, 2, ..., K_T$$

where the linear coefficients are given by

$$M_{a,ik} = \int_0^L \bar{a}\phi_{ai}\phi_{ak}dz \tag{4-34}$$

$$E_{a,ik} = -\int_0^L \frac{d}{dz}(\bar{a}\bar{v}\phi_{ai})\phi_{ak}dz \tag{4-35}$$

$$F_{a,ik} = -\int_0^L \frac{d}{dz}(\bar{a}\bar{v}\phi_{vi})\phi_{ak}dz \tag{4-36}$$

$$H_{a,k} = -\frac{1}{\alpha_o}\int_0^L \frac{d}{dz}(\bar{a}\bar{v}\bar{v}'_{\alpha_o})\phi_{ak}dz \tag{4-37}$$

$$S_{a,k} = -\frac{1}{\alpha_i}\int_0^L \frac{d}{dz}(\bar{a}\bar{v}\bar{v}'_{\alpha_i})\phi_{ak}dz \tag{4-38}$$

$$M_{v,ik} = \int_0^L \bar{a}\bar{v}\phi_{ai}\phi_{vk}dz \tag{4-39}$$

$$L_{ik} = \int_0^L \bar{a}\bar{v}\phi_{vi}\phi_{vk}dz \tag{4-40}$$

$$E_{v,ik} = \int_0^L \left[-\frac{d}{dz}(\bar{a}\bar{v}^2\phi_{ai}) + \frac{3}{\mathrm{Re}}\frac{d}{dz}\left(\bar{a}\bar{\mu}\frac{d\bar{v}}{dz}\phi_{ai}\right) + \frac{1}{Fr}\bar{a}\phi_{ai}\right]\phi_{vk}dz \tag{4-41}$$

$$F_{v,ik} = \int_0^L \left\{ -2\frac{d}{dz}\left(\overline{a}\overline{v}^2\phi_{vi}\right) + \frac{3}{\mathrm{Re}}\frac{d}{dz}\left[\overline{a}\overline{\mu}\frac{d}{dz}\left(\overline{v}\phi_{vi}\right)\right]\right\}\phi_{vk}dz \tag{4-42}$$

$$G_{v,ik} = \frac{3}{\mathrm{Re}}\int_0^L \frac{d}{dz}\left(\overline{a}S_1\frac{d\overline{v}}{dz}\phi_{Ti}\right)\phi_{vk}dz \tag{4-43}$$

$$H_{v,k} = \int_0^L \left\{ -\frac{2}{\alpha_o}\frac{d}{dz}\left(\overline{a}\overline{v}^2\overline{v}'_{\alpha_o}\right) + \frac{3}{\mathrm{Re}\,\alpha_o}\frac{d}{dz}\left[\overline{a}\overline{\mu}\frac{d}{dz}\left(\overline{v}\overline{v}'_{\alpha_o}\right)\right]\right\}\phi_{vk}dz \tag{4-44}$$

$$S_{v,k} = \int_0^L \left\{ -\frac{2}{\alpha_i}\frac{d}{dz}\left(\overline{a}\overline{v}^2\overline{v}'_{\alpha_i}\right) + \frac{3}{\mathrm{Re}\,\alpha_i}\frac{d}{dz}\left[\overline{a}\overline{\mu}\frac{d}{dz}\left(\overline{v}\overline{v}'_{\alpha_i}\right)\right]\right\}\phi_{vk}dz \tag{4-45}$$

$$R_k = -\int_0^L \overline{a}\overline{v}\frac{\overline{v}'_{\alpha_o}}{\alpha_o}\phi_{vk}dz \tag{4-46}$$

$$W_k = -\int_0^L \overline{a}\overline{v}\frac{\overline{v}'_{\alpha_i}}{\alpha_i}\phi_{vk}dz \tag{4-47}$$

$$M_{T,ik} = \int_0^L \overline{a}\overline{T}\phi_{ai}\phi_{Tk}dz \tag{4-48}$$

$$I_{ik} = \int_0^L \overline{a}\overline{T}\phi_{Ti}\phi_{Tk}dz \tag{4-49}$$

$$E_{T,ik} = \int_0^L \left[-\frac{d}{dz}\left(\overline{a}\overline{v}\overline{T}\phi_{ai}\right) + \frac{1}{Pe}\frac{d}{dz}\left(\overline{a}\overline{k}\frac{d\overline{T}}{dz}\phi_{ai}\right) + \frac{3E_c}{\mathrm{Re}}\overline{a}\overline{\mu}\left(\frac{d\overline{v}}{dz}\right)^2\phi_{ai}\right]\phi_{Tk}dz \tag{4-50}$$

$$F_{T,ik} = \int_0^L \left\{ -\frac{d}{dz}\left(\overline{a}\overline{v}\overline{T}\phi_{vi}\right) + \frac{6Ec}{\mathrm{Re}}\overline{a}\overline{\mu}\frac{d\overline{v}}{dz}\frac{d}{dz}\left(\overline{v}\phi_{vi}\right)\right\}\phi_{Tk}dz \tag{4-51}$$

$$\begin{aligned} G_{T,ik} = \int_0^L \Bigg\{ & -\frac{d}{dz}\left(\overline{a}\overline{v}\overline{T}\phi_{Ti}\right) + \frac{1}{Pe}\frac{d}{dz}\left[\overline{a}S_2\frac{d\overline{T}}{dz}\phi_{Ti} + \overline{a}\overline{k}\frac{d}{dz}\left(\overline{T}\phi_{Ti}\right)\right] \\ & - \frac{2\pi\overline{R}}{q_m\left(\mathbf{n}\cdot\mathbf{r}\right)}\left(S_3 + h\right)\phi_{Ti} + \frac{3Ec}{\mathrm{Re}}\overline{a}S_1\left(\frac{d\overline{v}}{dz}\right)^2\phi_{Ti}\Bigg\}\phi_{Tk}dz \end{aligned} \tag{4-52}$$

$$H_{T,k} = \int_0^L \left[-\frac{1}{\alpha_f} \frac{d}{dz} \left(\bar{a}\bar{v}\bar{T}\bar{v}'_{\alpha_f} \right) + \frac{6Ec}{\mathrm{Re}\,\alpha_f} \bar{a}\bar{\mu} \frac{d\bar{v}}{dz} \frac{d\bar{v}'_{\alpha_f}}{dz} \right] \phi_{Tk} dz \tag{4-53}$$

$$S_{T,k} = \int_0^L \left[-\frac{1}{\alpha_i} \frac{d}{dz} \left(\bar{a}\bar{v}\bar{T}\bar{v}'_{\alpha_i} \right) + \frac{6Ec}{\mathrm{Re}\,\alpha_i} \bar{a}\bar{\mu} \frac{d\bar{v}}{dz} \frac{d\bar{v}'_{\alpha_i}}{dz} \right] \phi_{Tk} dz \tag{4-54}$$

$$T_k = \int_0^L \frac{2\pi\bar{R}}{q_{m2}(\mathbf{n}\cdot\mathbf{r})} \tilde{\varepsilon}\bar{H}\phi_{Tk} dz \tag{4-55}$$

$$U_k = -\int_0^L \frac{2\pi\bar{R}}{q_{m2}(\mathbf{n}\cdot\mathbf{r})} \bar{h} \left(1 - \frac{T_a}{\bar{T}} \right) \phi_{Tk} dz \tag{4-56}$$

where $S_1 = \left.\frac{\partial \mu}{\partial T}\right|_{\bar{T}}$, $S_2 = \left.\frac{\partial \tilde{k}}{\partial T}\right|_{\bar{T}}$, and $S_3 = \left.\frac{\partial \tilde{E}}{\partial T}\right|_{\bar{T}}$

The measurable outputs include the fiber cross-section area, temperature and tension force at the post-chamber exit ($z = L$):

$$\mathbf{y}_0 = \left[a'(L,t) \quad T'(L,t) \quad F'(L,t) \right]^T \tag{4-57}$$

Using the elongational model $F_t = 3a\mu dv/dz$, the perturbation form of the tension force can be shown to be

$$F' = \left[3\bar{a} \frac{d\bar{v}}{dz} \left(\bar{\mu}a' + S_1 T' \right) + 3\bar{a}\bar{\mu} \frac{d}{dz} \left(\bar{v}v' \right) \right] / \bar{F} \tag{4-58}$$

Using Equations (4-28) ~ (4-30) and (4-58), the elements of the output vector in Equation (4-57) can be expressed as

$$y_1 = \sum_{i=1}^{K_a} x_{ai}(t) \phi_{ai}(L) \tag{4-59}$$

$$y_2 = \sum_{i=1}^{K_v} x_{vi}(t)\phi_{vi}(L) \tag{4-60}$$

$$\begin{aligned} y_3 = \Bigg\{ & 3\bar{a}\frac{d\bar{v}}{dz}\left(\bar{\mu}\sum_{i=1}^{K_a} x_{ai}\phi_{ai} + S_1\sum_{i=1}^{K_T} x_{Ti}\phi_{Ti} \right) \\ & + 3\bar{a}\bar{\mu}\left[\sum_{i=1}^{K_v} x_{vi}\frac{d}{dz}\left(\bar{v}\phi_{vi}\right) + \frac{v_o'}{\alpha_o}\frac{d}{dz}\left(\bar{v}\bar{v}_{\alpha_o}'\right) + \frac{v_i'}{\alpha_i}\frac{d}{dz}\left(\bar{v}\bar{v}_{\alpha_i}'\right) \right] \Bigg\}_{z=L} / \bar{F}(L) \end{aligned} \tag{4-61}$$

4.3.4 State Space Control Model

The actuator dynamics of the manipulated inputs can be approximated by the following 1st order models

$$\tau_o \dot{v}_o' + v_o' = K_o u_o \tag{4-62}$$

$$\tau_i \dot{v}_i' + v_i' = K_i u_i \tag{4-63}$$

$$\tau_f \dot{q}' + q' = K_f u_f \tag{4-64}$$

where the subscripts "*o*", "*i*" and "*f*" denote the fiber winding spool, preform feed mechanism, and furnace; and τ, K and u are the time constant, gain and input of the actuators, respectively. Equations (4-62) and (4-63) can be rearranged as

$$\dot{v}_o' = -\frac{1}{\tau_o} v_o' + \frac{K_o}{\tau_o} u_o \tag{4-65}$$

$$\dot{v}_i' = -\frac{1}{\tau_i} v_i' + \frac{K_i}{\tau_i} u_i \tag{4-66}$$

After substituting equations (4-65) and (4-66) into Equation (4-32), we can combine the actuator dynamics and the linear ODE system model and write the ROM in the following state space form:

$$\begin{aligned}\mathbf{M}\dot{\mathbf{x}}_0 &= \mathbf{A}_0\mathbf{x}_0 + \mathbf{B}_0\mathbf{u} + \mathbf{D}_h h' \\ \mathbf{y}_0 &= \mathbf{C}_0\mathbf{x}_0 + \mathbf{D}_0\mathbf{u}\end{aligned} \tag{4-67}$$

where $\mathbf{x}_0 = [x_{a1}, x_{a2}, \ldots, x_{aK_a}, x_{v1}, x_{v2}, \ldots, x_{vK_v}, x_{T1}, x_{T2}, \ldots, x_{TK_a}, v_o', v_i', q']^T$ is the state vector; and $\mathbf{u} = [u_o, u_i, u_f]^{\mathrm{T}}$ is the input vector. The number of state variables is $K = K_a + K_v + K_T + 3$. The matrixes $\mathbf{M}$, $\mathbf{A}_0 \in \mathbf{R}^{K\times K}$, $\mathbf{B}_0 \in \mathbf{R}^{K\times 3}$, $\mathbf{D}_{\mathrm{h}} \in \mathbf{R}^{K\times 1}$, $\mathbf{C}_0 \in \mathbf{R}^{3\times K}$, and $\mathbf{D}_0 \in \mathbf{R}^{3\times 3}$ can be identified from the ROM, and are given by

$$\mathbf{M} = \begin{bmatrix} \mathbf{M}_a & 0^{K_a\times K_v} & 0^{K_a\times K_T} \\ \mathbf{M}_v & \mathbf{L} & 0^{K_v\times K_T} \\ \mathbf{M}_T & 0^{K_T\times K_v} & \mathbf{I}^{K_T\times K_T} \end{bmatrix} \tag{4-68}$$

$$\mathbf{A}_0 = \left[\begin{array}{ccc|ccc} \mathbf{E}_a & \mathbf{F}_a & 0^{K_a\times K_T} & 0^{K_a\times 1} & 0^{K_a\times 1} & 0^{K_a\times 1} \\ \mathbf{E}_v & \mathbf{F}_v & \mathbf{G}_v & \mathbf{H}_v - \mathbf{R}/\tau_o & \mathbf{S}_v - \mathbf{W}/\tau_i & 0^{K_v\times 1} \\ \mathbf{E}_T & \mathbf{F}_T & \mathbf{G}_T & \mathbf{H}_T & \mathbf{S}_T & \mathbf{T} \\ \hline & 0^{3\times(K_a+K_v+K_T)} & & -1/\tau_o & 0 & 0 \\ & & & 0 & -1/\tau_i & 0 \\ & & & 0 & 0 & -1/\tau_f \end{array}\right] \tag{4-69}$$

$$\mathbf{B}_0 = \begin{bmatrix} 0^{K_a\times 1} & 0^{K_a\times 1} & 0^{K_a\times 1} \\ \mathbf{R}K_o/\tau_o & \mathbf{W}K_i/\tau_i & 0^{K_v\times 1} \\ 0^{K_T\times 1} & 0^{K_T\times 1} & 0^{K_T\times 1} \\ K_o/\tau_o & 0 & 0 \\ 0 & K_i/\tau_i & 0 \\ 0 & 0 & K_f/\tau_f \end{bmatrix} \tag{4-70}$$

$$\mathbf{C}_0 = \left[\begin{array}{ccc|c} \phi_a^{1\times K_a}(L) & 0^{1\times K_v} & 0^{1\times K_T} & 0^{2\times 3} \\ 0^{1\times K_a} & \phi_a^{1\times K_v}(L) & 0^{1\times K_T} & \\ \hline & \mathbf{C}_1 & & \mathbf{C}_2 \end{array}\right] \tag{4-71}$$

where

$$\mathbf{C}_1 = \left[\left(\frac{3\bar{a}\bar{\mu}\phi_a^{1\times K_a}}{\bar{F}} \frac{d\bar{v}}{dz} \right)\Bigg|_{z=L} \quad \left[\frac{3\bar{a}\bar{\mu}}{\bar{F}} \frac{d}{dz}\left(\bar{v}\phi_v^{1\times K_v}\right) \right]\Bigg|_{z=L} \quad \left(\frac{3\bar{a}S_1\phi_T^{1\times K_T}}{\bar{F}} \frac{d\bar{v}}{dz} \right)\Bigg|_{z=L} \right] \tag{4-72}$$

$$\mathbf{C}_2 = \left[\left[\frac{1}{\alpha_o \bar{F}} \frac{d}{dz}\left(\bar{v}\bar{v}'_{\alpha_o}\right) \right]\Bigg|_{z=L} \quad \left[\frac{1}{\alpha_i \bar{F}} \frac{d}{dz}\left(\bar{v}\bar{v}'_{\alpha_i}\right) \right]\Bigg|_{z=L} \quad 0 \right] \tag{4-73}$$

4.4 Robust Control

In this section, we design a mixed H∞/LQG controller which not only minimizes the H_2 norm but also reduces the H∞ norm of the closed-loop system to less than a small constant. The minimization of the H_2 norm guarantees the good performance of the close-loop system. The small H_∞ norm increases the robustness of the close-loop system so that the effect of the modeling errors is reduced. The control objective of the fiber drawing process is to regulate the fiber diameter and tension under the effects of disturbances. The uniformity of the fiber diameter is one of the key quality factors affecting the optical loss in fibers. The deviation of the fiber diameter from the nominal value of $125\mu m$ should be no larger than $1\mu m$ and as small as possible. The main source of disturbances is the fluctuation of h' which has high frequency contents. The effect of the high frequency disturbances can only be compensated by manipulating the draw speed since the other two control inputs (feed rate and furnace heat flux) have very small bandwidths and the corresponding actuators have large time constants as will be shown in the later simulations. In this case, the fluctuations in the fiber diameter and tension cannot be minimized at the same time with only a single effective control input. We choose the fiber diameter as the higher priority regulated output in this study.

The plant model can be formulated as the following standard state space two-port system:

$$\begin{aligned}\dot{\mathbf{x}} &= \mathbf{A}\mathbf{x} + \mathbf{B}\mathbf{u} + \mathbf{D}_1\mathbf{w} \\ \mathbf{z} &= \mathbf{E}_1\mathbf{x} + \mathbf{E}_2\mathbf{u} \\ \mathbf{y} &= \mathbf{C}\mathbf{x} + \mathbf{D}\mathbf{u} + \mathbf{D}_2\mathbf{w}\end{aligned} \tag{4-74}$$

where a new state variable $x_{K+1} = \int_0^t a'(L,t)dt$ is added and $\mathbf{x} = [\mathbf{x}_0{}^{\mathrm{T}}\ x_{K+1}]^{\mathrm{T}}$. The system given by Equation (4-67) is augmented by the following state equation

$$\dot{x}_{K+1} = a'(L,t) = \begin{bmatrix}1 & 0 & 0\end{bmatrix}(\mathbf{C}_0\mathbf{x}_0 + \mathbf{D}_0\mathbf{u}) \tag{4-75}$$

The performance vector is given by $\mathbf{z} = [\mathbf{z}_{\mathrm{x}}{}^{\mathrm{T}}\ \mathbf{z}_{\mathrm{u}}{}^{\mathrm{T}}]^{\mathrm{T}}$, where $\mathbf{z}_x = \begin{bmatrix}x_{K+1} & \varepsilon_1 F'(L,t)\end{bmatrix}^T$ and $\mathbf{z}_u = diag(\begin{bmatrix}\varepsilon_2 & \varepsilon_3 & \varepsilon_4\end{bmatrix})\mathbf{u}$. Instead of using $a'(L,t)$ directly, the integration of $a'(L,t)$ or x_{K+1} in $\mathbf{z}_{\mathrm{x}}$ is used to eliminate the steady state error of the fiber diameter. This integration adds one more order to the system. The constants ε_i (i = 1, 2, 3, 4) are the weights on the performance variables and control efforts, which can be tuned to obtain the best overall performance. ε_1 should be less than 1 since the fiber tension has lower priority than the fiber diameter as mentioned earlier. The weighting matrix $\mathbf{E}_1$ and $\mathbf{E}_2$ are readily given as follows:

$$\mathbf{E}_1 = \begin{bmatrix} 0^{1\times K} & 1 \\ \begin{bmatrix}0 & 0 & \varepsilon_1\end{bmatrix}\mathbf{C}_0 & 0 \\ 0^{3\times(K+1)} & 0^{3\times 1}\end{bmatrix} \tag{4-76}$$

$$\mathbf{E}_2 = \begin{bmatrix} 0^{1\times 3} \\ \begin{bmatrix}0 & 0 & \varepsilon_1\end{bmatrix}\mathbf{D}_0 \\ diag(\begin{bmatrix}\varepsilon_2 & \varepsilon_3 & \varepsilon_4\end{bmatrix})\end{bmatrix} \tag{4-77}$$

The measured output is given by $\mathbf{y} = \begin{bmatrix} a'(L,t) & T'(L,t) \end{bmatrix}^T$. Although the fiber tension at the chamber exit is also available in the measurement, we do not include it in **y** since the calculation of F' involves one more linearization in Equation (4-58), which may induce poor performance in the dynamic observer. The disturbance input vector is formed by two parts: $\mathbf{w} = [\mathbf{w}_1{}^{\mathrm{T}} \quad \mathbf{w}_2{}^{\mathrm{T}}]^{\mathrm{T}}$; the system disturbance vector $\mathbf{w}_1$ is given by $\mathbf{w}_1 = \begin{bmatrix} h' & w_o & w_i & w_f \end{bmatrix}^T$ where w_o, w_i and w_f are the disturbances superposed on the actuator inputs u_o, u_i and u_f, respectively; the sensor noises for the measured output vector **y** are given by $\mathbf{w}_2 = \begin{bmatrix} w_a & w_T \end{bmatrix}^T$ where w_a and w_T are the noise on $a'(L,t)$ and $T'(L,t)$. The matrixes $\mathbf{A} \in \mathbf{R}^{(K+1)\times(K+1)}$, $\mathbf{B} \in \mathbf{R}^{(K+1)\times 3}$, $\mathbf{C} \in \mathbf{R}^{2\times(K+1)}$ and $\mathbf{D} \in \mathbf{R}^{2\times 3}$ are readily obtained from Equation (4-67) and are given as follows:

$$\mathbf{A} = \left[\begin{array}{c|c} \mathbf{M}^{-1}\mathbf{A}_0 & 0^{K\times 1} \\ \hline \begin{bmatrix} 1 & 0 & 0 \end{bmatrix}\mathbf{C}_0 & 0 \end{array}\right] \tag{4-78}$$

$$\mathbf{B} = \begin{bmatrix} \mathbf{M}^{-1}\mathbf{B}_0 \\ \begin{bmatrix} 1 & 0 & 0 \end{bmatrix}\mathbf{D}_0 \end{bmatrix} \tag{4-79}$$

$$\mathbf{C} = \begin{bmatrix} 1 & 0 & 0 \\ 0 & 1 & 0 \end{bmatrix}\begin{bmatrix} \mathbf{C}_0 & 0^{3\times 1} \end{bmatrix} \tag{4-80}$$

$$\mathbf{D} = \begin{bmatrix} 1 & 0 & 0 \\ 0 & 1 & 0 \end{bmatrix}\mathbf{D}_0 \tag{4-81}$$

The weighting matrixes for the disturbances and noises are given by

$$\mathbf{D}_1 = \begin{bmatrix} \begin{bmatrix} \mathbf{M}^{-1}\mathbf{D}_h & 0 \end{bmatrix}^T & \mathbf{B}diag(\begin{bmatrix} \varepsilon_5 & \varepsilon_6 & \varepsilon_7 \end{bmatrix}) & 0_{(K+1)\times 2} \end{bmatrix} \tag{4-82}$$

$$\mathbf{D}_2 = \begin{bmatrix} 0_{2\times 4} & diag(\begin{bmatrix} \varepsilon_8 & \varepsilon_9 \end{bmatrix}) \end{bmatrix} \tag{4-83}$$

where ε_i (i = 5-9) are the tunable weights.

The system given by Equation (4-74) is stabilizable and detectable. Given the above (N+1)th order plant model, the mixed H_∞/LQG control problem is to determine an (N+1)th order dynamic compensator

$$\begin{aligned} \dot{\mathbf{x}}_c &= \mathbf{A}_c\mathbf{x}_c + \mathbf{B}_c\mathbf{y} \\ \mathbf{u} &= \mathbf{C}_c\mathbf{x}_c \end{aligned} \tag{4-84}$$

which satisfies the following design criteria:

i) the close-loop system in Equation (4-74) and (4-84) is internally stable;

ii) the close-loop transfer function $\widetilde{G}_{zw}(s)$ from disturbances **w** to performance variables **z** satisfies the constraint

$$\left\|\widetilde{G}_{zw}(s)\right\|_\infty = \sup_{\omega\in\mathbf{R}} \sigma_{\max}\left[\widetilde{G}_{zw}(j\omega)\right] \le \gamma \tag{4-85}$$

where σ denotes the singular value and $\gamma > 0$ is a given constant; and

iii) the H_2 norm of $\widetilde{G}_{zw}(s)$

$$\left\|\widetilde{G}_{zw}(s)\right\|_2^2 = \frac{1}{2\pi}\int_{-\infty}^{\infty}\left\|\widetilde{G}_{zw}(j\omega)\right\|_F^2 d\omega \tag{4-86}$$

is minimized.

The block diagram of the close loop system is shown in Figure 4-1. The solution of the above control problem can be found in Haddad (1995) and is given below

$$\mathbf{A_c} = \mathbf{A} - \mathbf{Q}\mathbf{C}^T\mathbf{V}_2^{-1}\mathbf{C} - \mathbf{B}\mathbf{R}_\mathbf{2}^{-1}\mathbf{B}^T\mathbf{P}\left(\mathbf{I} - \gamma^{-2}\mathbf{Q}\mathbf{P}\right)^{-1} + \gamma^{-2}\mathbf{Q}\mathbf{R_1} \tag{4-87}$$

$$\mathbf{B_c} = \mathbf{Q}\mathbf{C}^T\mathbf{V}_2^{-1} \tag{4-88}$$

$$\mathbf{C_c} = -\mathbf{R}_2^{-1}\mathbf{B}^T\mathbf{P}\left(\mathbf{I} - \gamma^{-2}\mathbf{Q}\mathbf{P}\right)^{-1} \tag{4-89}$$

where the positive semi-definite matrix **P** and **Q** satisfy

$$\mathbf{A}^T\mathbf{P} + \mathbf{P}\mathbf{A} + \mathbf{R}_1 + \gamma^{-2}\mathbf{P}\mathbf{V}_1\mathbf{P} - \mathbf{P}\mathbf{B}\mathbf{R}_2^{-1}\mathbf{B}^T\mathbf{P} = 0 \tag{4-90}$$

$$\mathbf{A}\mathbf{Q} + \mathbf{Q}\mathbf{A}^T + \mathbf{V}_1 + \gamma^{-2}\mathbf{Q}\mathbf{R}_1\mathbf{Q} - \mathbf{Q}\mathbf{C}^T\mathbf{V}_2^{-1}\mathbf{C}\mathbf{Q} = 0 \tag{4-91}$$

and where $\mathbf{R}_1 = \mathbf{E}_1{}^T\mathbf{E}_1$, $\mathbf{R}_2 = \mathbf{E}_2{}^T\mathbf{E}_2$, $\mathbf{V}_1 = \mathbf{D}_1\mathbf{D}_1{}^T$, $\mathbf{V}_2 = \mathbf{D}_2\mathbf{D}_2{}^T$.

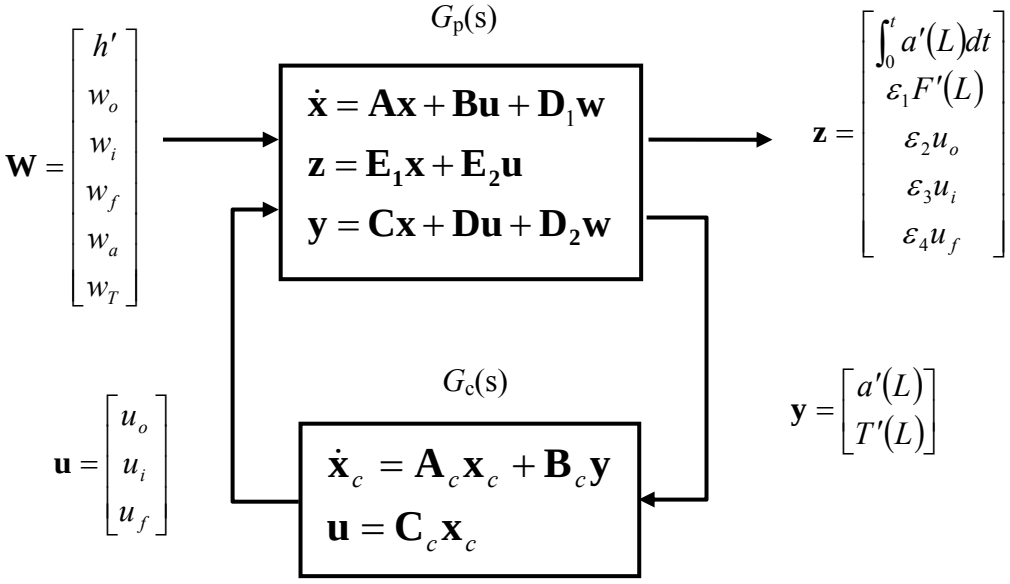

Figure 4-1 Block diagram of the close-loop system

From the small gain theory, the H_∞ norm of the system uncertainty matrix $\Delta(s)$ should not exceed $1/\gamma$ in order to retain the asymptotic stability of the close-loop system. Hence, higher system robustness can be achieved by using smaller γ in Equation (4-85). But if γ is too small, there may not be positive semi-definite solution of **P** and **Q** in

Equations (4-90) and (4-91). In order to obtain the highest possible robustness, we estimate an initial value of γ and then gradually reduce its value until the smallest possible γ that renders positive semi-definite solution of **P** and **Q** is found.

CHAPTER V

COMPUTATIONAL RESULTS

5.1 Overview

The computational results of this thesis consist two parts: 1) numerical solutions of the CFD models; and 2) dynamic simulations of the robust control system. Using the numerical model and algorithm developed in Chapters II and III, the first part of this chapter presents the steady state simulations of the modern fiber drawing process where large preforms and high draw speeds are used. The models are validated by numerical and experimental methods. The 2-D numerical solutions of the temperature and velocity fields in both the glass and air domains are presented. The characteristics of the variable distributions are analyzed. The accuracy of the semi 2-D model is studied by comparing with the complete 2-D model. The semi 2-D model is then used to study the effects of draw speed on the glass temperature distribution and the glass solidification location in the post-chamber. In the second part of this chapter, the ROM is validated by comparing with a dynamic semi 2-D CFD model in the transient responses. The close-loop simulations of the robust control system are carried out using the dynamic CFD model. Finally, the robustness of the controller is studied under different sources of modeling errors.

5.2 Computational Results of the CFD models

In this section, the steady state simulations using the CFD models developed in Chapter II and III are carried out. The models are validated by numerical and experimental methods.

5.2.1 Simulation Parameters

A MATLAB program with C++ subroutines has been written to predict the temperature/velocity fields in a state-of-the-art fiber drawing process as shown in Figure 1-2, where a high draw speed (up to 35m/s) along with a large preform diameter (up to 0.18m) is considered. The simulation parameters are shown in Table 5-1.

Table 5-1: Parameters used in the simulation

Specified fiber radius, R_f (μm)	62.5
Specified draw speed, v_f (m/s)	18, 25, 30, 35
Specified draw tension, F_t (grams)	90
Preform radius, R_p (m)	0.045
Furnace peak temperature, $T_{f,max}$ (K)	2,400
Furnace minimum temperature, $T_{f,min}$ (K)	1,700
Furnace radius, R_{fur} (m)	0.06
Furnace length, L_f (m)	0.45
Post-chamber radius, R_{post} (m)	0.055
Post-chamber length, L_p (m)	2.75

The glass preform is made of fused silica. Most of the physical properties of fused silica are taken from Fleming (1964). More recent experimental correlation of the glass viscosity was obtained by Bansal (1986)

$$\mu(T) = 0.1\exp\left(-14.368 + \frac{61939.539}{T}\right) \tag{5-1}$$

The radiation properties and the band-model of the wavelength spectrum are given in Appendix B.

A non-uniform grid is used with a denser spacing near the free interface and the walls. In the air domain, the dimension of the first grid adjacent to the fiber surface should be at least less than half of the fiber radius, *i.e.*, 30μm, in order to account for the sharp gradients in the boundary layer.

Two cases are studied in the following simulations:

Case 1, furnace domain

The complete 2-D model is used and only the furnace domain is considered; the Neumann boundary condition for the velocity given by Equation (3-25) is used at the furnace exit. Since the glass surface velocity is small and the air temperature is close to the glass temperature in the furnace domain, the air convective heat flux is much smaller than the dominant radiation flux. Hence, the use of an approximate heat transfer coefficient h will not affect the accuracy of the solution significantly, while the total computation time can be greatly reduced. A sinusoidal variation of h varying from 30 W/m^2K at the furnace inlet to 50 W/m^2K at the exit was used. This heat transfer coefficient was based on the numerical solution of the 2-D air temperature in the furnace and the post-chamber. The average air temperature of 1900K inside the furnace was used. The simulation in this case offers the detailed 2-D temperature and velocity distribution in the glass. It also validates the effectiveness of the semi 2-D model.

A grid size study in the glass domain showed that no noticeable changes in the results are observed when the grid number is larger than 81x15 (in z and r directions, respectively). This is much smaller than 401x21 used by Choudhury *et al.* (1999). One of

the reasons for the efficiency is that the staggered grid guarantees strict energy conservation in the finite volume discretizaiton and reduces fluctuations in the solution. The grid used in Case 1 for the glass domain is shown in Figure 5-1.

Case 2, furnace/post-chamber domain

Semi 2-D model is used in this case and both the furnace and the post-chamber domains are considered. The simulation obtains the complete free surface profile so that the fiber solidification location can be predicted. The glass temperature in the post-chamber is also obtained. Both of these results are critical in supporting the post-chamber and the draw process design. Since the air convective heat flux becomes dominant for the glass cooing and solidification in the post-chamber, the 2-D air convection problem is numerically solved to obtain the heat flux along the free interface. As will be shown in the following results, the numerical solution from the semi 2-D model is close to that from the complete 2-D model, while the computation using the semi 2-D model is much more efficient than that using the complete 2-D model.

After a grid size study and refinement, the grid numbers of 200×15 and 160×34 (in z and r directions, respectively) are used in the glass and the air domain, respectively. Figure 5-2 shows the grid used in Case 2 for the air domain.

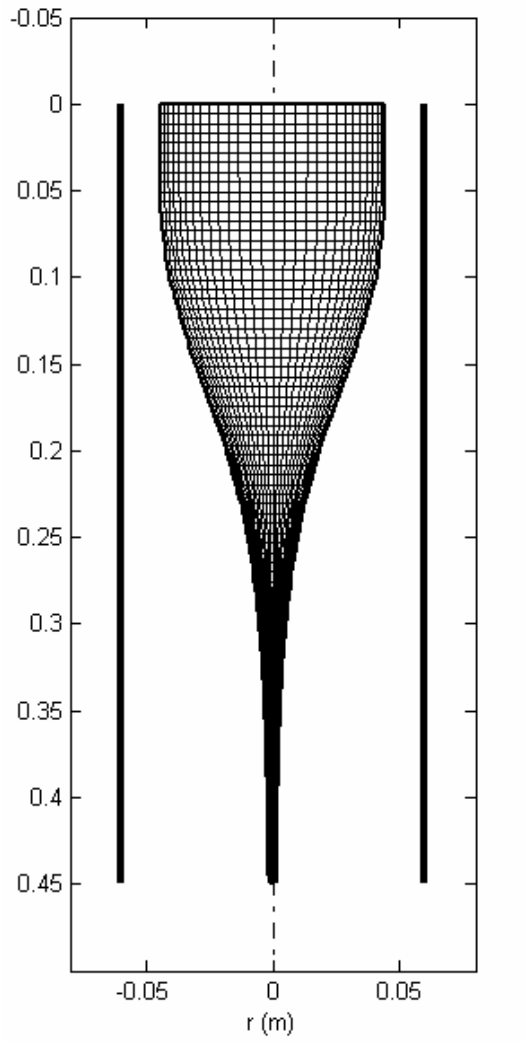

Figure 5-1 Curvilinear grid (81x15) used in Case 1 for the glass domain

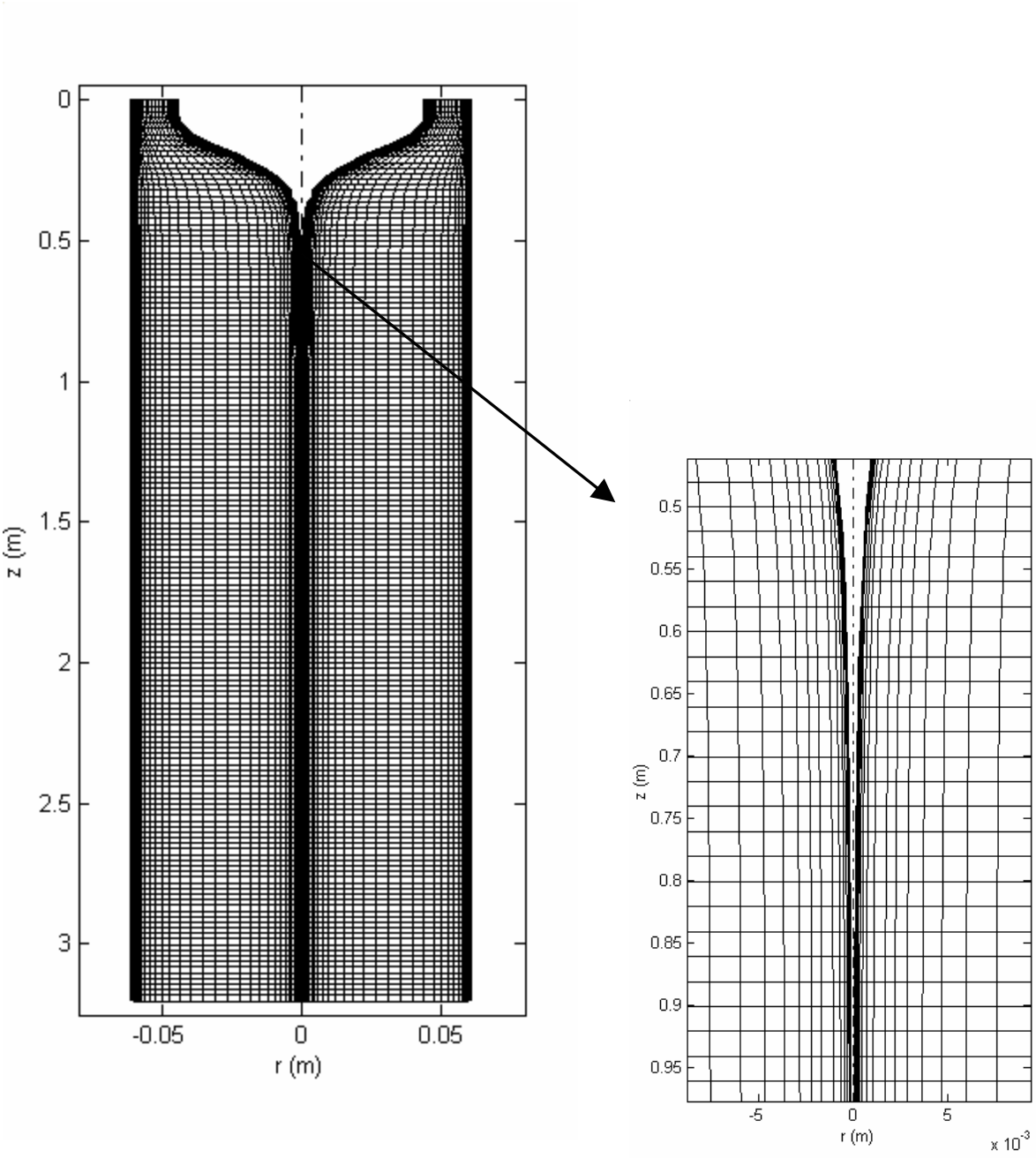

Figure 5-2 Curvilinear grid (160×34) used in Case 2 for the air domain

5.2.2 Model Validations

Since the measurement of the in-situ glass temperature and velocity, radiative and convective heat flux is extremely difficult inside the furnace and post-chamber under a

high temperature environment. We validate the radiation model and the CFD model using indirect numerical and experimental methods.

5.2.2.1 Radiation Model Validation

The validation of the 2-D computation code for the radiation transfer consists of two parts: the first part is to test the second law of thermodynamics; the second test compares the computation results against an exact integral solution of RTE which is available for 1-D semitransparent cylinders.

In the first test, the top and bottom boundaries of the glass domain are modified as perfect reflectors and adiabatic surfaces, and the furnace wall and the furnace openings form a blackbody surface with a constant temperature. For this enclosed system, the second law of thermodynamics requires the steady state glass temperature approaching the furnace temperature. Figure 5-3 shows the simulation results. The small discrepancy in Figure 5-3(a) is due to the mismatch between the control angle edge and the free surface at the neck-down region (so called control angle overhang). It is reduced by increasing the number of control angles as shown in Figure 5-3(b). These results satisfy the second law of thermodynamics.

Exact integral solution of RTE is available for a 1-D semitransparent cylinder whose temperature only varies in radial direction (Kesten, 1968). In order to validate our 2-D solution with this integral solution in the second test, the boundary conditions have been modified to obtain an equivalent 1-D solution. The diameter of the cylinder is constant. Unity diffuse reflectivities are assumed at both the top and the bottom boundaries. The temperatures in the glass and the furnace wall are assumed to be uniform such that the radiation intensity does not vary in the axial direction. Figure 5-4

compares the FVM solution with the integral solution under different glass temperatures and cylinder diameters. The radial flux is normalized by the furnace blackbody emissive power. As shown in the figures, the computed results agree with the exact solutions.

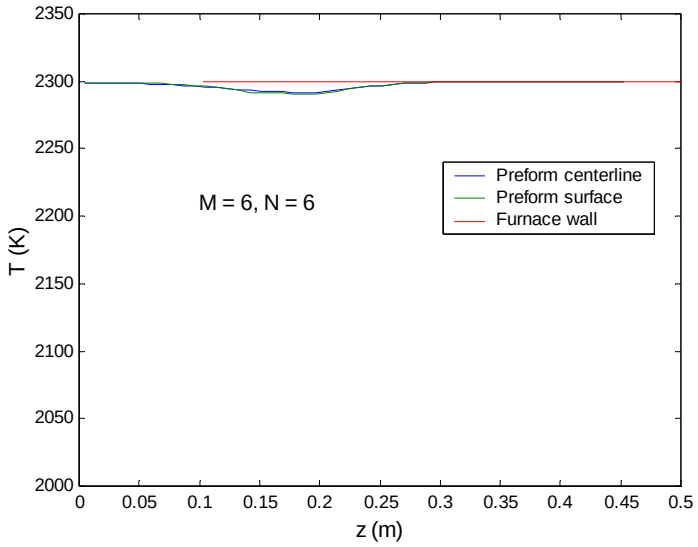

(a) Number of control angles 6x6

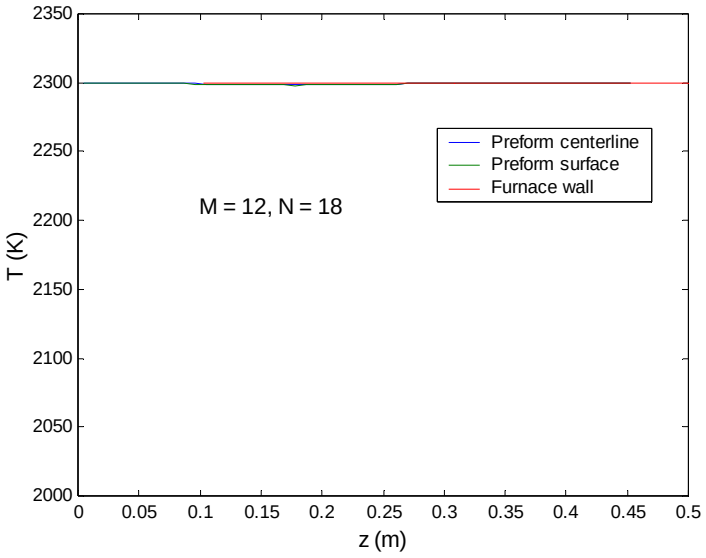

(b) Number of control angles 12x18

Figure 5-3 Steady state glass temperature in the enclosed furnace

(a) T_g = 500K

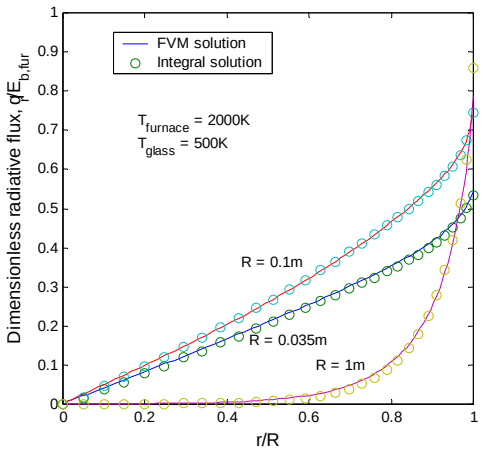

(b) T_g = 1,000K

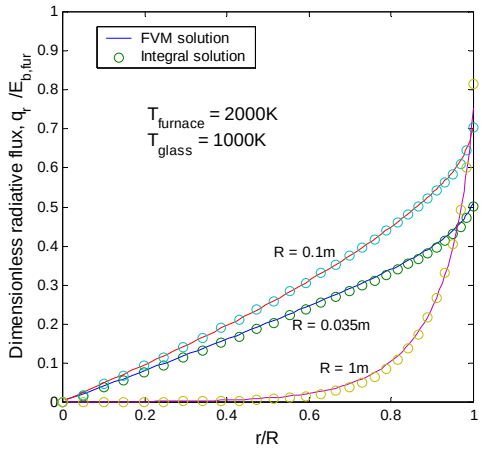

(c) T_g = 1,500K

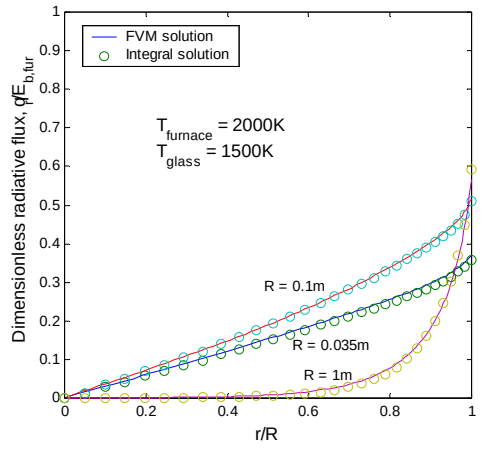

Figure 5-4 Comparison of the FVM and the integral solutions (T_f = 2000K)

5.2.2.2 Experimental Validation

We measured the stead state free surface profiles of the glass in the furnace domain and compared with the numerical predictions as follows. In the experiment, the preform was moved out of the furnace in a short time (less than 1 minute) in order to prevent shape deformation while the view factors were changed. After the glass cooled down, the neck-down profile was then measured by a laser scanner. Since the glass in the post-chamber had a small diameter and could break easily while the space for moving the preform was limited, only the neck-down profile in the furnace domain was measured. The remainder of the glass was cut before the preform was taken out.

Figure 5-5 compares the predicted free surface profiles against the measured ones at a draw speed of 25m/s. Both the complete and semi 2-D models were used to predict the free surface profile. The relative errors of the predicted free surface radii from the measurements are shown in Figure 5-6. As shown in Figure 5-6, most part of the predicted neck-down shapes has a relative error within ±15% from the measured data. The large error near the furnace exit can be explained by the following reason: when the preform is cut from the bottom and taken out of the furnace, the tension force caused by the draw mechanism does not exist anymore; as a consequence, the velocity gradient (and hence the free surface slope) near the bottom of the stub decreases since it is proportional to the normal tension force according to the elongational model $\sigma_{zz} = 3\mu dv/dz$. Hence, the measured free surface profile at the bottom has a smaller slope and larger diameter than that in the stead drawing process on which the predictions are based. It follows that the prediction errors near the furnace exit could be smaller than that shown in Figure 5-6. The discrepancy in the neck-down region can also be explained partly by the above

reason. But the modeling errors such as the surface radiation properties and the furnace temperature measurement errors may come into play.

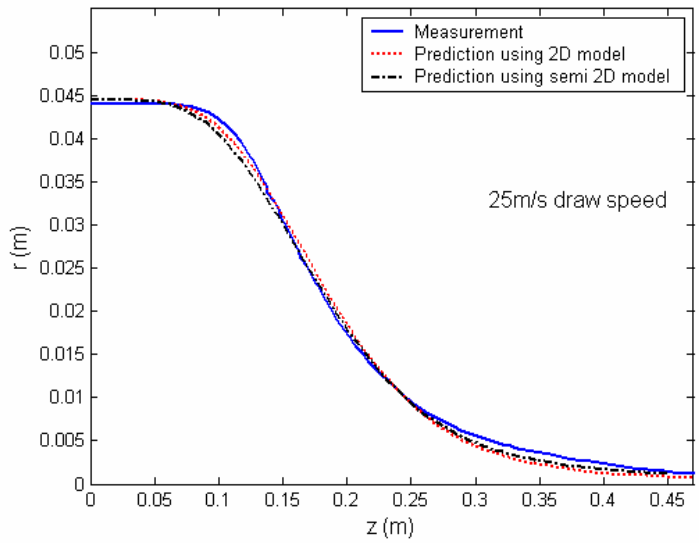

Figure 5-5 Model validations through free surface profiles

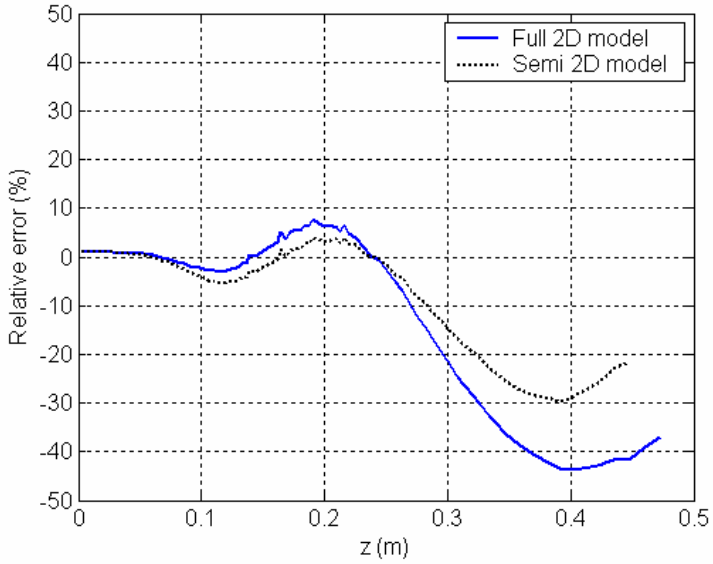

Figure 5-6 Relative errors of the predicted free surface radius

The inner wall temperature of the post-chamber was measured at several locations using thermo-couples in the 35m/s draw speed case. Figure 5-7 compares the calculated post-chamber wall temperature against the measured data and shows close agreement with each other. Hence, the method presented in Section 2.3.4 is an effective way to calculate the post-chamber wall temperature.

The fiber temperature at the exit of the post-chamber was also measured by an infrared thermo camera. The measured result at the draw speed of 30m/s is around 1400K, and the corresponding simulation result is 1418K. This close agreement partly validates the calculation of the mixed convection of the air around the fiber.

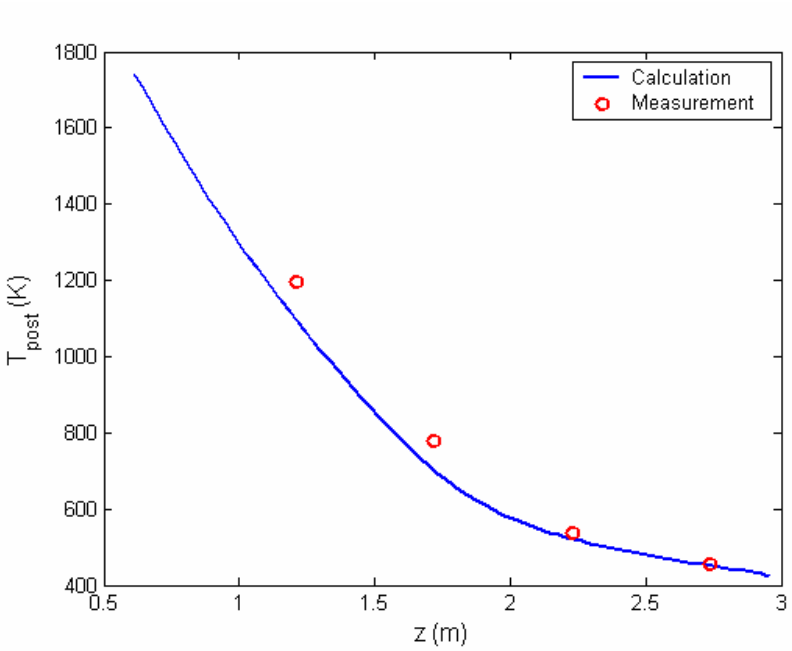

Figure 5-7 Experimental validation of the calculated post-chamber inner wall temperature

5.2.3 Simulation Results

In this section, the 2-D numerical solutions of the temperature/velocity fields in both the glass and air domains are presented. The accuracy of the semi 2-D model is

studied by comparing with the complete 2-D model. The semi 2-D model is then used to study the effects of draw speed on the glass temperature distribution and the glass solidification location in the post-chamber.

5.2.3.1 2-D Thermo-Fluid Transports in the Glass Domain

The following simulation results are for Case 1 in the glass domain at the draw speed of 25m/s.

Figure 5-8 to Figure 5-10 presents the 2-D glass temperature distributions, where Figure 5-8 shows the 2-D isothermal contours; Figure 5-9 and Figure 5-10 show the normalized radial and axial temperature distributions, respectively. Several observations are made:

- The glass temperature has a fairly two-dimensional distribution.
- The glass has a positive radial temperature gradient when absorbing heat flux near the furnace inlet, while has a negative radial gradient when dissipating heat flux at the furnace exit.
- The glass temperature near the furnace inlet is below the melting point due to the large view factors of that part to the ambient through the top opening.
- The glass temperature near the furnace exit decreases slowly but is well above the melting point as a result of strong advection, where the glass speed is rapidly increasing in this region. The glass should be cooled slowly before the solidification so that the optical loss in the final fiber product is low. Hence, a long insulated post-chamber is needed to cool the glass below the melting point.

Figure 5-11 to Figure 5-13 presents the 2-D glass velocity distributions, where Figure 5-11 shows the contours of the axial velocity; Figure 5-12 and Figure 5-13 show the normalized radial and axial velocity distributions, respectively. Several observations are made:

- The glass axial velocity component distribution is close to one-dimensional, even at the neck-down region. This can be explained by the follow mechanism. As the glass temperature is at most 20% higher than the melting point as shown in Figure 5-10. The glass viscosity is still high at the temperature. Any radial variation of v will cause a large shear stress, which in turn reduces the velocity variation in the radial direction.

- Near the furnace inlet, the glass start to melt from the surface due to the positive radial temperature gradient (as shown in Figure 5-9) while the center remains largely solid. Hence, the surface has a higher velocity than that at the center. When the glass completely melts in the neck-down region (about 1/3 of the furnace length), the surface velocity becomes lower than the centerline velocity. The radial variation of the axial velocity becomes negligible near the furnace exit where the molten glass is highly viscous and has a small diameter.

- The glass axial velocity increases exponentially in the neck-down region.

Although the glass velocity field is close to 1-D, the small radial variation of the axial velocity may have some significant effect on the material flow. In order to illustrate this, a visualization program utilizing the computed 2-D velocity field has been written to track a group of fictitious infinitesimal particles originally distributed at the same flat cross-section plane in the preform as they travel through the neck-down region.

Snapshots of the particles at different instants of time can be graphed from the following integral:

$$\mathbf{r}(t) = \mathbf{r}(0) + \int_0^t \mathbf{V}(\mathbf{r}(s))ds \tag{5-2}$$

where the location vector **r** is obtained by integrating the velocity vector **V** along a path in the r-z coordinate system; and *s* is a dummy variable representing time in the integration. Figure 5-14 shows how the particles travel through the neck-down region from the furnace inlet (or at z = 0), where the dashed lines represent the interface between the core rod and the cladding tube. As depicted in Figure 5-14(a), the particle distributions become dramatically distorted once they moves pass 1/3 of the furnace length where the glass axial velocity are faster in the center than that near the surface. Although the radial variations of the axial velocity component is not significant, the distortion of the particle distribution is accelerating since the particles at the center moves faster than those at the surface once the center particles move ahead to a larger velocity field. Pure one-dimensional models are not able to predict this effect of the 2-D flow pattern. An immediate application of this calculation is to predict the effect of a thin flat gap originally in the preform core on the final fiber if the computation domain is extended to the solidification point.

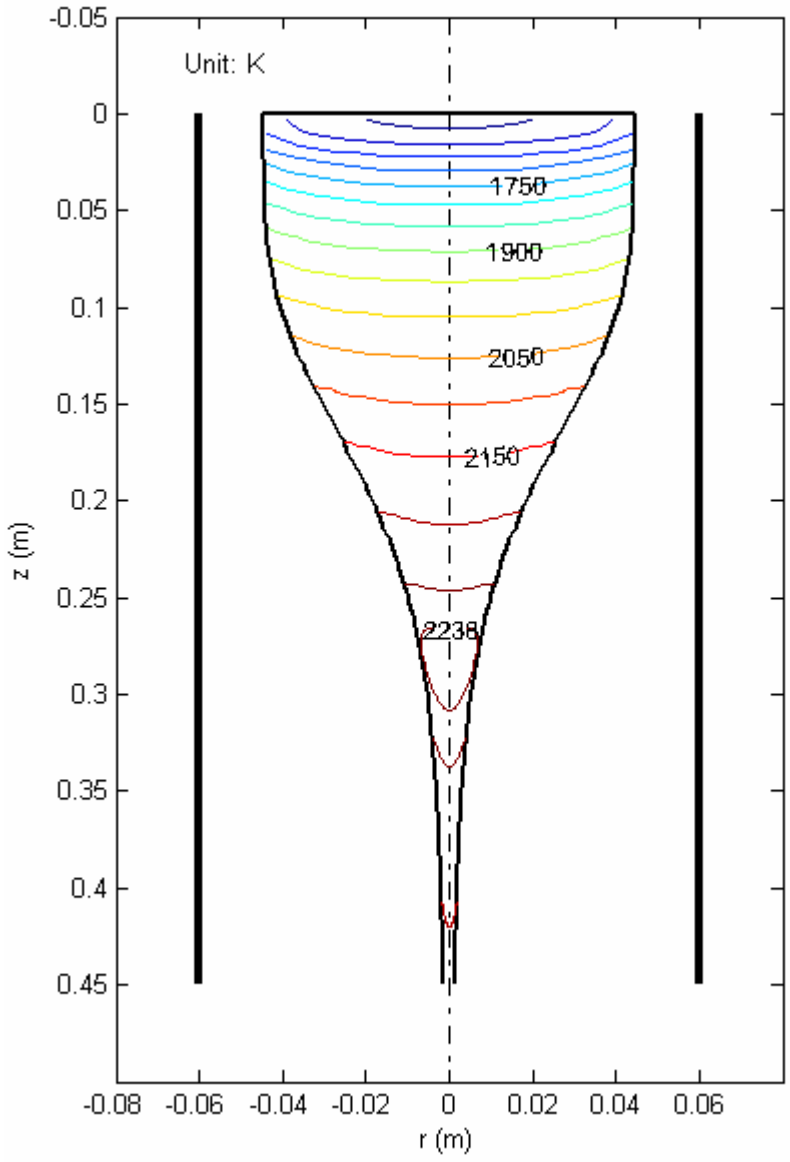

Figure 5-8 Glass temperature contour in the furnace domain

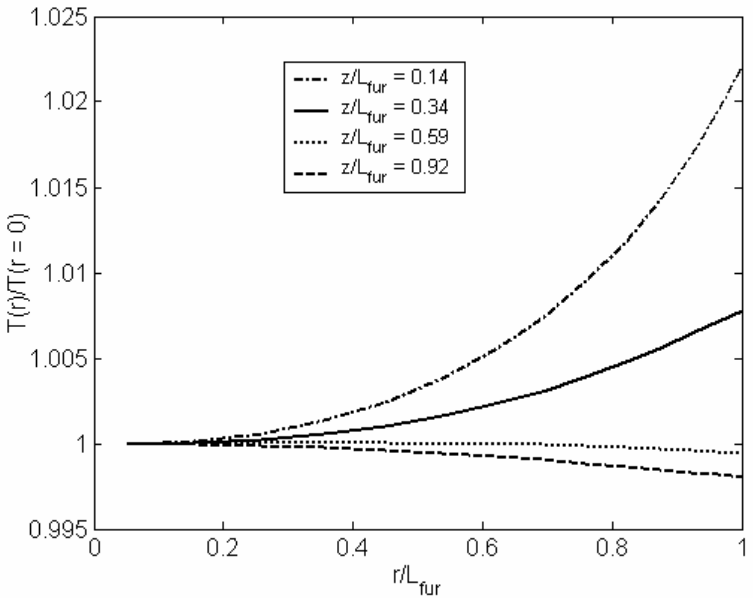

Figure 5-9 Radial temperature distribution of the glass

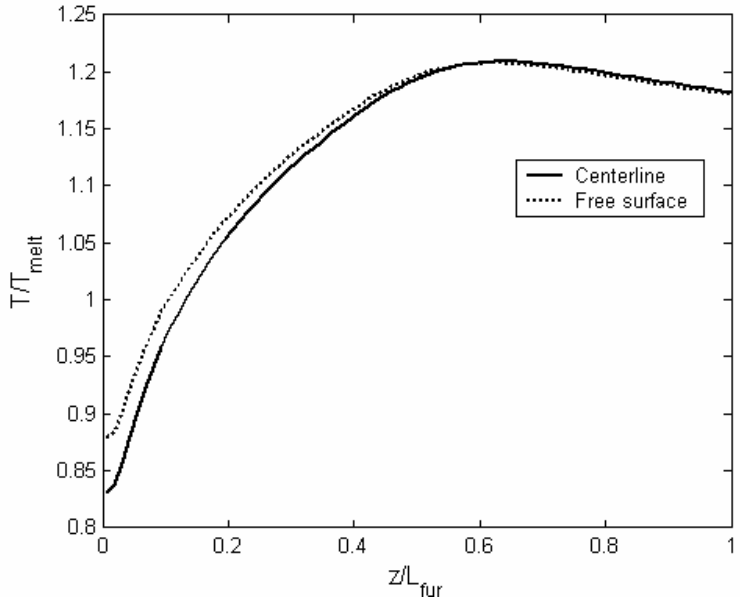

Figure 5-10 Axial temperature distribution of the glass

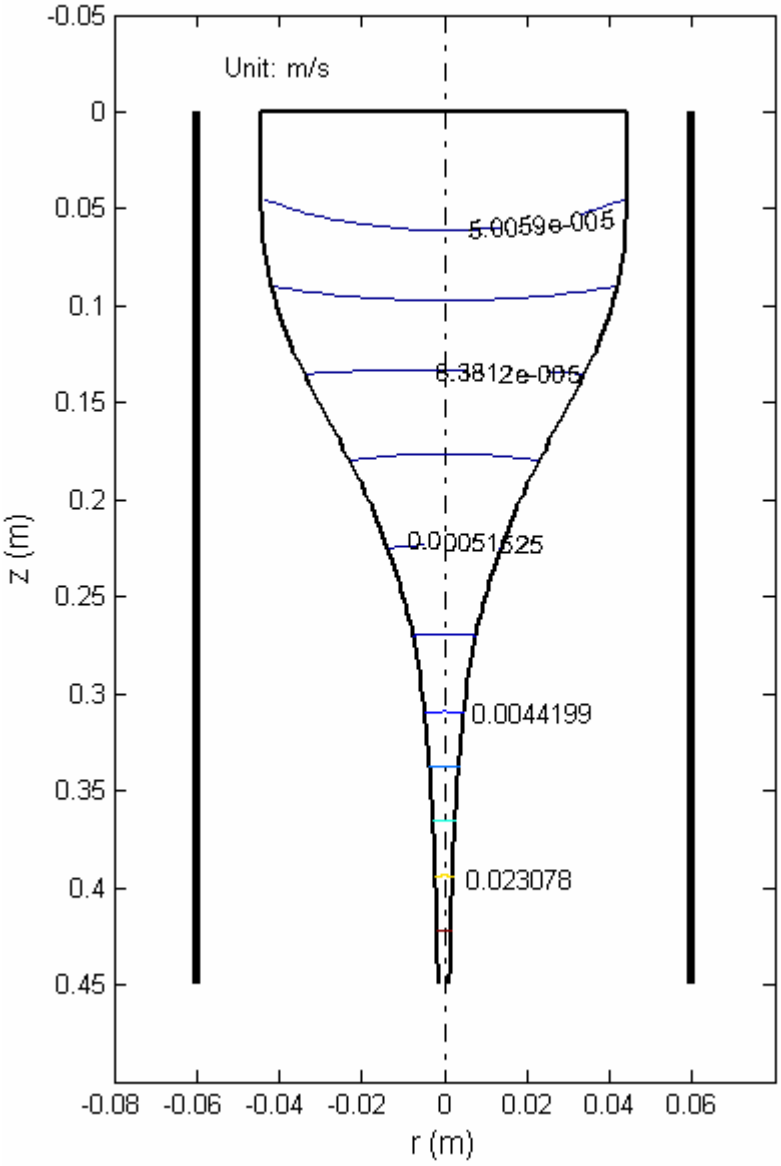

Figure 5-11 Glass velocity contour in the furnace domain

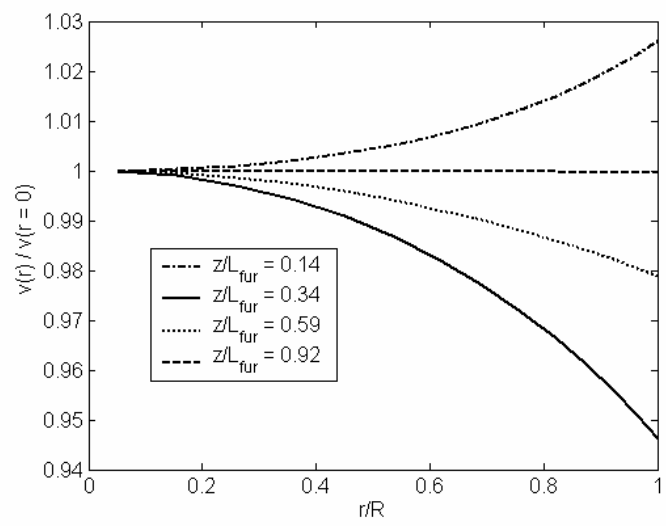

Figure 5-12 Radial distribution of normalized *v* in the glass

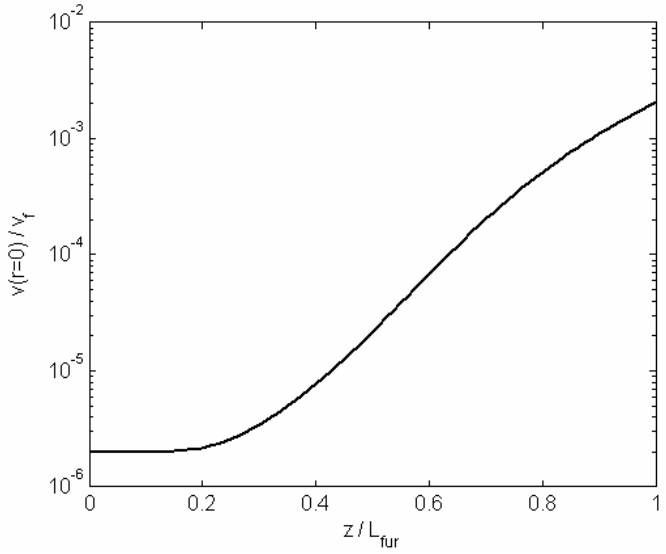

Figure 5-13 Axial distribution of normalized *v* in the glass

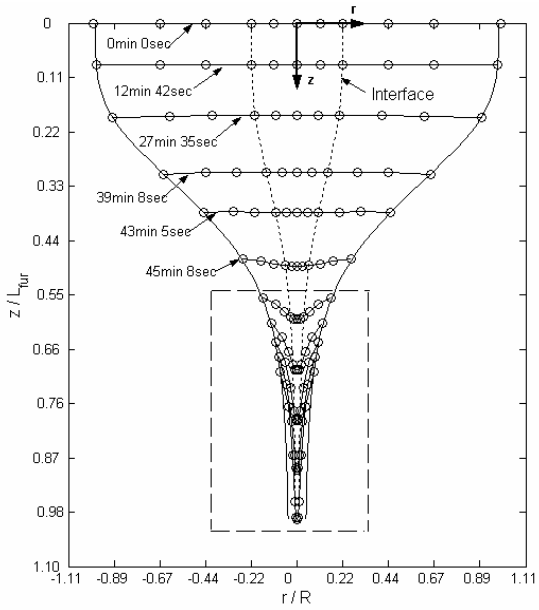

(a) complete snapshots at different instants of time

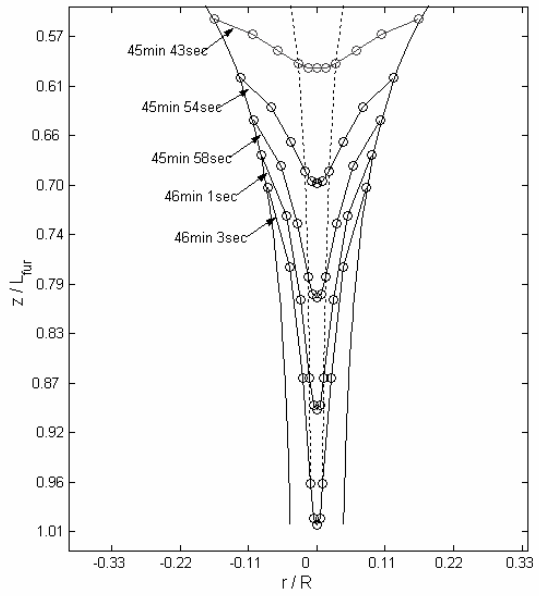

(b) zoom in the rectangular region in (a)

Figure 5-14 Particle flow tracking

5.2.3.2 2-D Thermo-Fluid Transports in the Air Domain

The following 2-D temperature and velocity distributions in the air domain are obtained in simulation case 2 at the draw speed of 25m/s. Since the ambient air may enter the chamber through the small iris opening at the bottom of the post-chamber, the post-chamber should be included in the computation domain so that the boundary condition at the opening can be specified.

Figure 5-15 and Figure 5-16 show the air temperature and velocity distributions, respectively. The speed of the glass in most part of the post-chamber is higher than 1m/s and increases until it reaches a steady state draw speed as shown in Figure 5-17. A boundary layer of air develops and grows downward around the continuously moving slim glass cylinder in the post-chamber due to the viscous drag at the surface as shown in Figure 5-15 and Figure 5-16. The air inside the boundary layer moves in the same direction as the glass. At the iris opening, the boundary layer has a thickness comparable to the radius of the opening. Hence, the buoyancy force generated by the pressure difference between the interior of the chamber and the ambient is greatly compensated by the inertia force (or dynamic pressure) in the boundary layer and the net air flow rate through the opening is small. As a result, the air in the furnace and the post-chamber is almost stationary relative to the strong convection inside the boundary layer, so the air temperature in the chamber is close to the wall temperature which is high above the ambient due to the radiation from the furnace and the insulation layer. The relatively small temperature difference between the glass and the air reduces the glass cooling rate before the solidification as desired.

Figure 5-18 compares the air convective heat flux with the radiation heat flux along the glass free surface. The air convective heat flux is negligible as compared with the radiative flux in the neck-down region inside the furnace. Hence, the use of an approximate heat transfer coefficient in simulation case 1 does not have considerable effect on the accuracy of the numerical solution as mentioned earlier. But the air convective heat flux becomes significant in the post-chamber as shown in the figure due to the high surface area to volume ratio and the high moving speed of the glass. As the thermal transport of the air in the post-chamber has significant effect on the glass temperature, 2-D numerical solution of the mixed air convection is required to obtain the heat flux at the glass surface in simulation case 2.

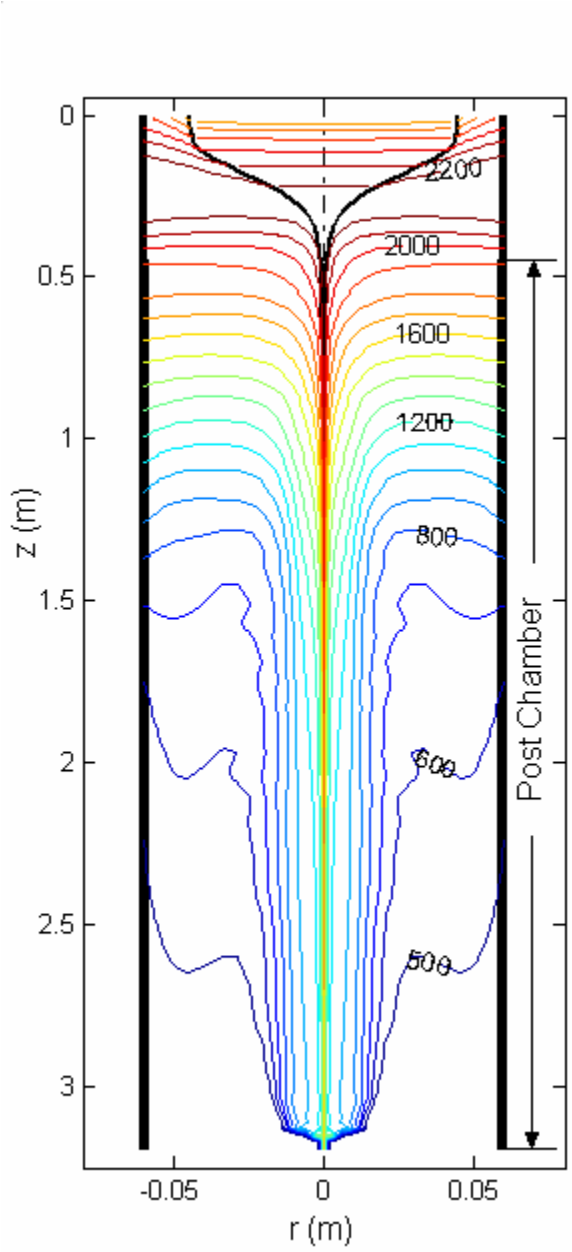

Figure 5-15 Air temperature contour in the furnace and post-chamber domain

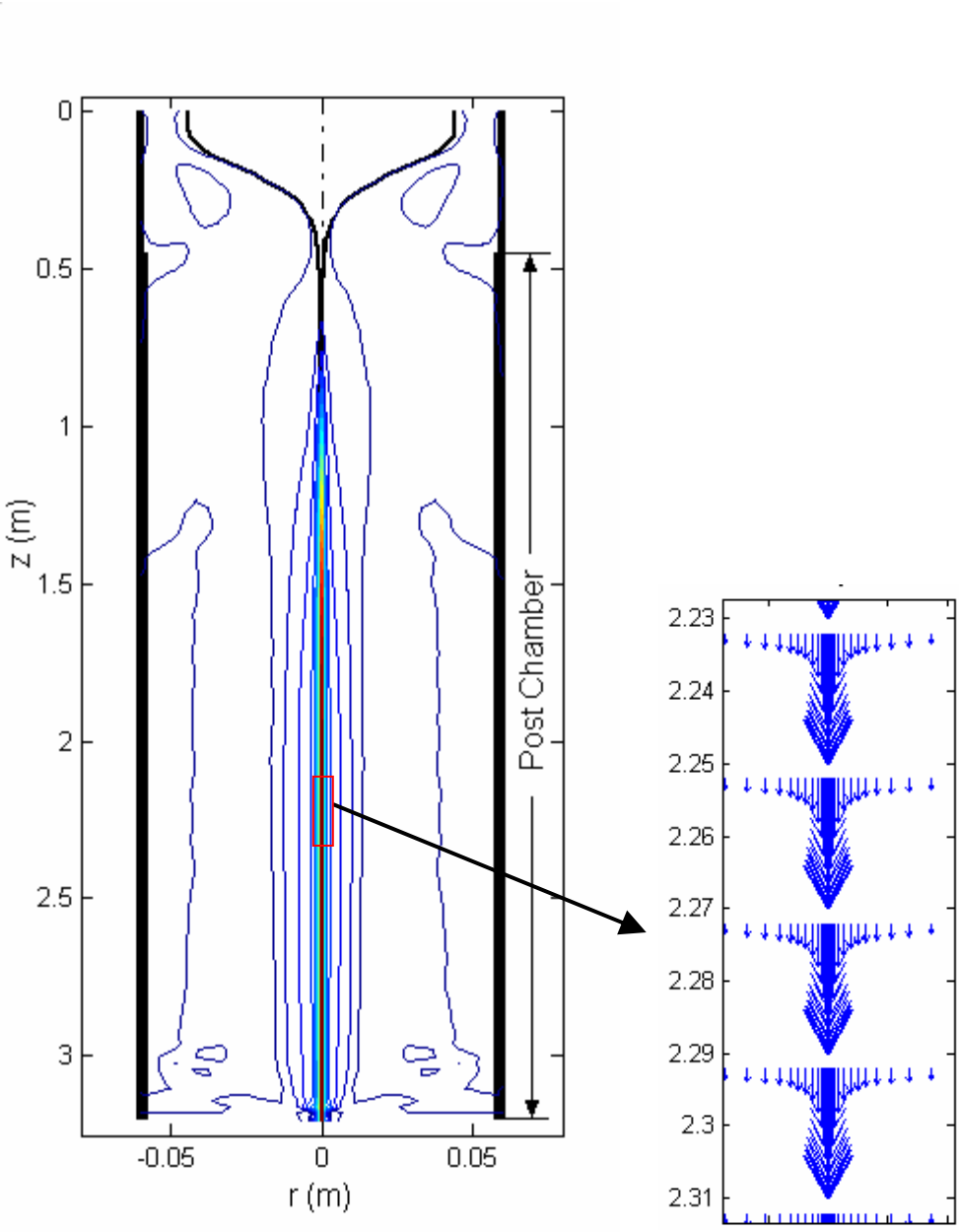

Figure 5-16 Air velocity contour in the furnace and post-chamber domain

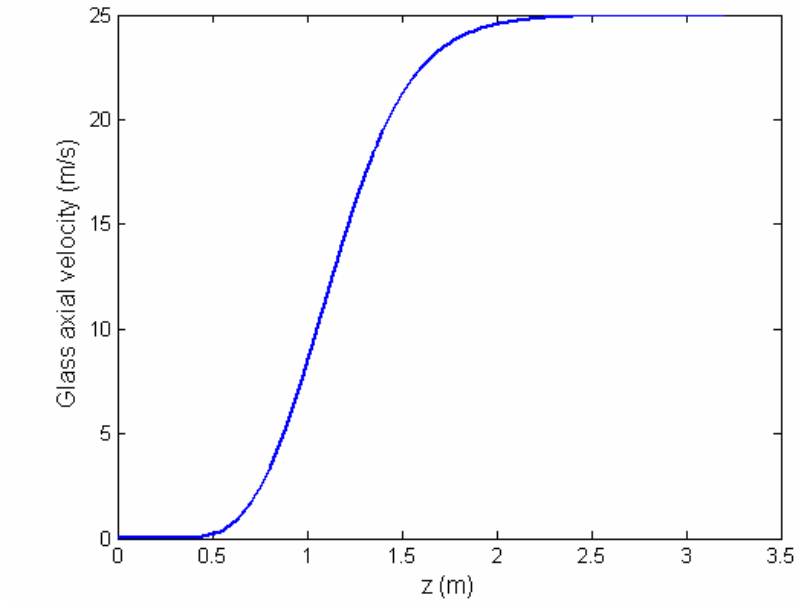

Figure 5-17 Glass surface axial velocity distribution

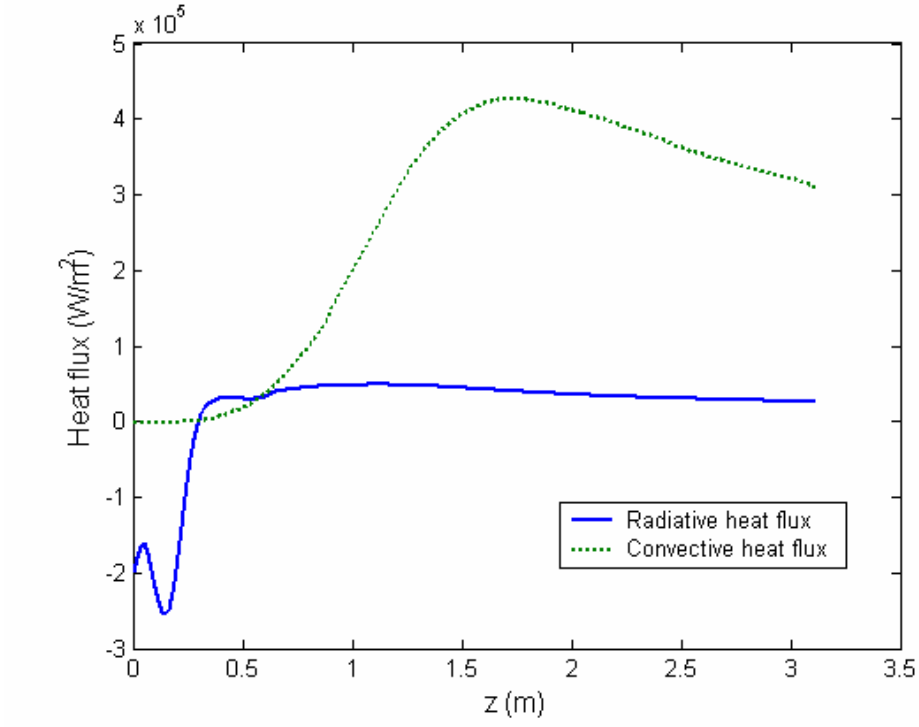

Figure 5-18 Heat flux on the glass free surface

5.2.3.3 Numerical validation of the Semi 2-D Model

It has been shown in Figure 5-5(a) that the free surface profile predicted by the semi 2-D model is close to that predicted by the complete 2-D model and matches the measurement data well. In order to demonstrate that this is still true for draw processes with larger preforms, we consider a case with parameters given in Table 5-2, where the preform diameter is doubled.

Table 5-2: Parameters used in the large-preform simulation

Specified fiber radius, R_f (μm)	62.5
Specified draw speed, v_f (m/s)	25
Specified draw tension, F_t (grams)	90
Preform radius, R_p (m)	0.09
Furnace peak temperature, $T_{f,max}$ (K)	2,460
Furnace minimum temperature, $T_{f,min}$ (K)	1,760
Furnace radius, R_{fur} (m)	0.12
Furnace length, L_{fur} (m)	0.7
Post-chamber radius, R_{post} (m)	0.12
Post-chamber length, L_p (m)	2.75

Figure 5-19, Figure 5-20 and Figure 5-21 compare the semi 2-D model and the full 2-D model in terms of the predicted free surface profile, the glass centerline temperature, and the axial velocity in the furnace domain, respectively. As shown in Figure 5-19, the diameter of the preform in the neck-down region predicted by the semi 2-D model is smaller than that from the 2-D model. Consequently, the temperature in that region is higher due to the higher view factors to the hot spot of the furnace. At the bottom of the furnace, the diameter of the glass predicted by the semi 2-D model is larger than that from the full 2-D model. As a consequence, the velocity of the glass is smaller as shown in Figure 5-21 since the mass flow rate is conserved in the axial direction. The axial mass advection is weaker as the velocity is smaller, which results in a lower

temperature near the exit in the semi 2-D solution as shown in Figure 5-20. As shown in the figures, all the above mentioned differences are negligible relative to the absolute variable values. Hence, the semi 2-D model can be used to effectively predict the free surface profile and the temperature distribution for preforms up to 0.18m in diameter.

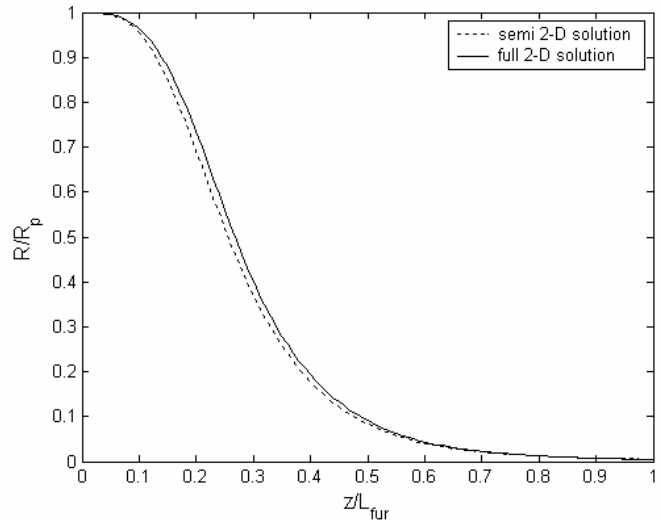

Figure 5-19 Free surface profiles predicted by the full and the semi 2-D models

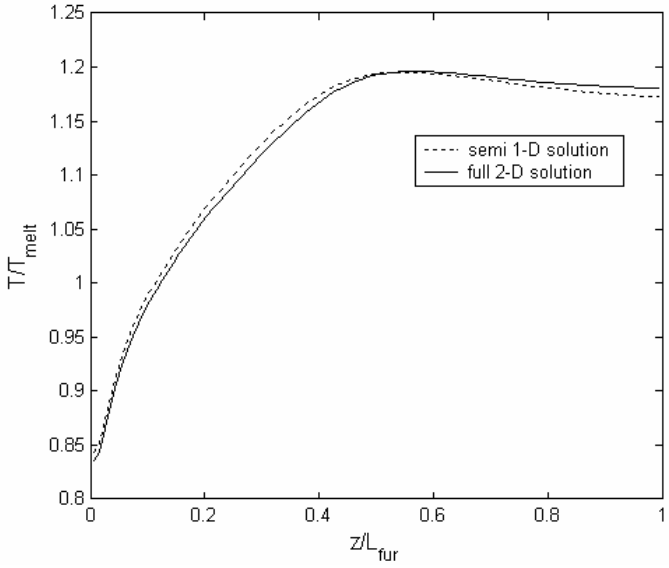

Figure 5-20 Centerline temperature predicted by the full and the semi 2-D models

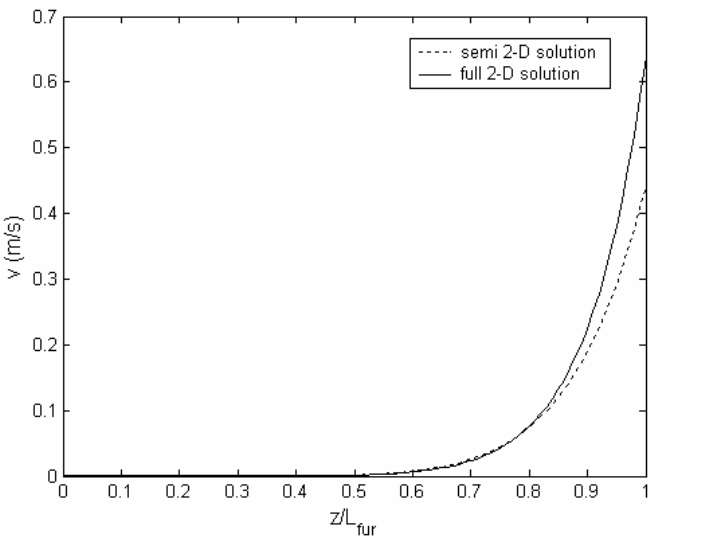

Figure 5-21 Axial velocity distributions predicted by the full and the semi 2-D models

5.2.3.4 Free Surface Profile and Fiber Solidification

Given a furnace and post-chamber configuration, an effective way to increase productivity is to use higher draw speeds and larger preforms. As a consequence, the glass takes a much longer distance to converge into fiber. On the other hand, the glass has to be cooled slowly during its gradual solidification in order to reduce the optical loss in the final product. Hence, an insulated post-chamber is usually added below the furnace where the glass melt keeps converging and is gradually cooled below the softening point. The interests here are to predict if the fiber can be steadily drawn and if the fiber solidifies inside the post-chamber under the high draw speeds.

The following results are from simulation case 2 using the parameters in Table 5-1. The draw speed was increased from 18m/s to 35m/s. Steady state solutions were obtained for all the draw speeds, which means the fiber can be steadily drawn under the given parameters. Figure 5-22 shows the effect of the draw speed on the neck-down profiles. When the draw speed is increased, the neck-down profile is shifted or stretched

downward to a certain extend. It is expected that the free surface region is longer for a higher draw speed. Figure 5-23 shows the axial glass temperature distributions (normalized to the melting point) under different draw speeds. The glass/fiber temperature decreases more slowly in the post-chamber under a higher draw speed. This implies that the effect of the advection increase on the glass temperature is much stronger than that of the air convection increase as the Reynolds number associated with the draw speed is higher. Figure 5-24 shows the convergence of the glass diameters to that of the fiber when the glass solidifies in the post-chamber. As shown in the figure, the fiber solidification is rather a gradual monotonically process than those of crystalline materials with a single phase transition temperature. Solid state glasses and fibers are actually non-crystalline super-cooled "liquid-like" melts. We define the location where the glass reaches within a bound of 0.25% about the steady state diameter (125μm) as the fiber solidification location. Figure 5-25 compares two methods of locating the fiber solidification for different draw speeds; namely, constant fiber diameter, and fiber melting temperature (1580ºC). The close match between the two methods shows that the glass viscosity at the melting point is high enough that the glass behaves like a solid. Hence, the glass (melting) temperature can be reasonably used to locate the fiber solidification. As shown in Figure 5-25, the fiber solidifies closer to the post-chamber exit when the draw speed is higher. It can be expected that if the draw speed increases above 40m/s, the fiber may solidify outside the post-chamber, in which case a longer post-chamber and draw tower is needed.

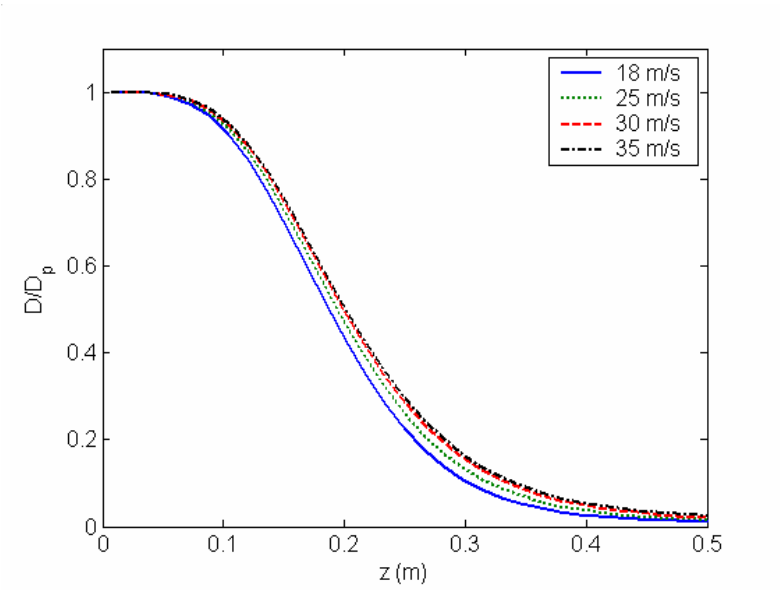

Figure 5-22 Neck-down profiles under different draw speeds

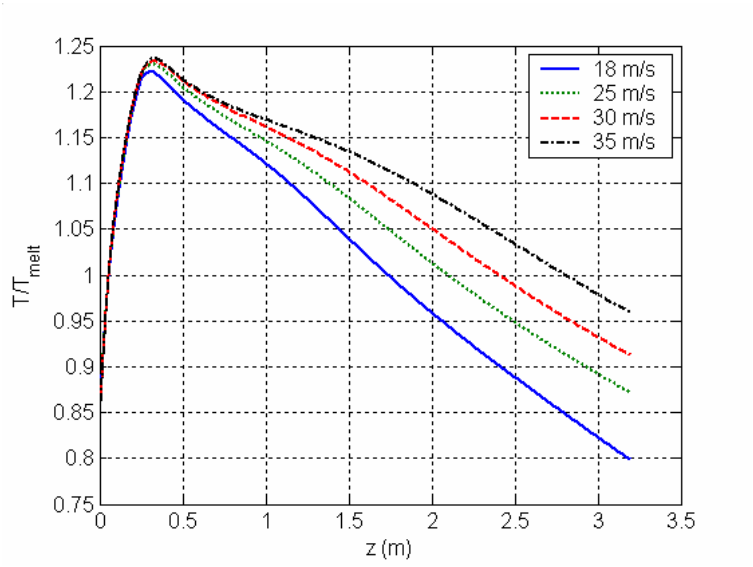

Figure 5-23 Axial temperature distributions under different draw speeds

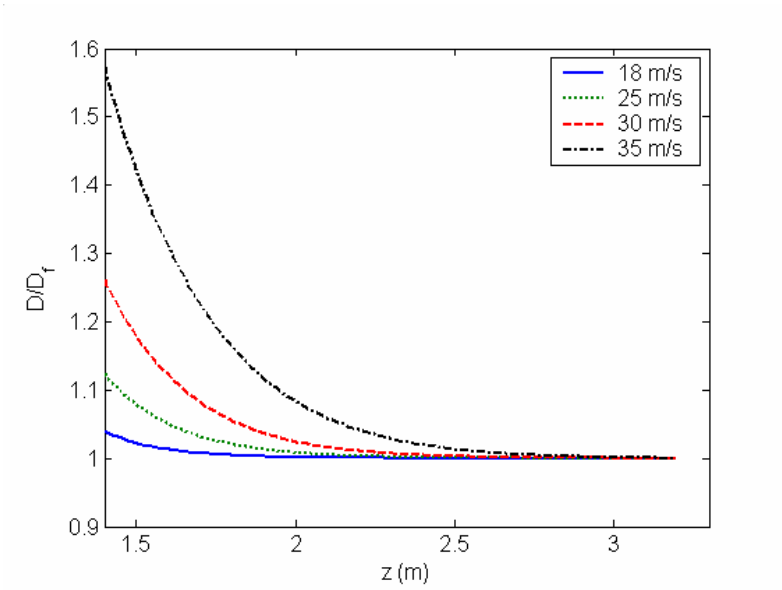

Figure 5-24 Fiber solidifications under different draw speeds

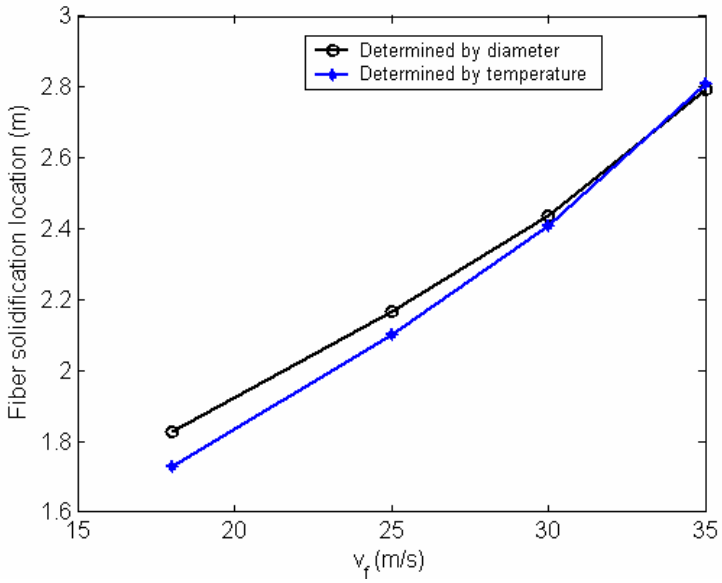

Figure 5-25 Fiber solidification locations under different draw speeds

5.3 Simulation Results for Robust Control

In all the following simulations, we consider a nominal draw speed of 25m/s and the other parameters are given in Table 5-1. A dynamic semi 2-D model is constructed by combining the 2-D energy equation and RTE with the 1-D fluid dynamic model given by Equations (4-1) and (4-2). The semi 2-D model developed in Section 3.4 is actually the steady state version of this dynamic model and has been validated in Section 5.2. The ROM is compared with the dynamic semi 2-D model in the transient responses. The close-loop responses are simulated using the dynamic semi 2-D CFD model. Finally, the robustness studies are carried out.

5.3.1 Results in Reduced Order Modeling

As described in Section 4.3.2, we need to simulate the transient responses to each input at both its lowest frequency (step input) and highest frequency (sinusoidal input at $\omega_{\max}$) using the quasi 1-D CFD model developed in Section 4.2. Table 5-3 gives the parameters used in obtaining the snapshots for each input. We only simulated the step responses to the inputs of v_i' and q' since the bandwidths of the system for these inputs are quite small.

Table 5-3 Parameters for snapshots

Input variables	$v_o'(t)$	$v_i'(t)$	$q'(t)$	$h'(t)$
Input functions	M and $M\sin(2\pi\omega_{\max}t)$	M	M	M and $M\sin(2\pi\omega_{\max}t)$
M	0.04	0.05	0.02	0.1
$\omega_{\max}$	100	-	-	100
Number of snapshots	250	100	150	254

Figure 5-26 shows the first 20 eigenvalues of the matrix **B** given by Equation (4-27) for each state variable (a', $\hat{v}$ and T') using a total number of 754 snapshots. For each variable, the eigenvalues are normalized to the first (maximum) one. The magnitude of the eigenvalues decreases exponentially to below 10^{-7} after the 20th eigenvalue. This suggests a potential to represent the system dynamics by only a small number of eigenmodes. We determined K_a = 25, K_v = 8 and K_T = 10 in obtaining the ROM by neglecting the eigenmodes corresponding to small eigenvalues. Since the governing equations for v and T are parabolic, the dominant dynamics are characterized by a small number of degrees of freedom. The continuity equation that governs a' is approximately hyperbolic, which requires more eigenmodes to accurately describe the dynamics. Figure 5-27 to Figure 5-29 show the first 3 eigenfunctions for each of the 3 state variables; and Figure 5-30 to Figure 5-32 show the last 3 eigenfunctions retained as the basis functions for each of the 3 state variables. The numerical eigenfunctions corresponding to the large eigenvalues have large magnitudes and smooth distributions. These eigenfunctions represent the large scale structures of the state variables and are related to the steady state response. On the contrary, the numerical eigenfunctions corresponding to the small eigenvalues have small magnitudes and sharply changing distributions. These eigenfunctions represent the small scale structures of the state variables and are related to the fast transient response.

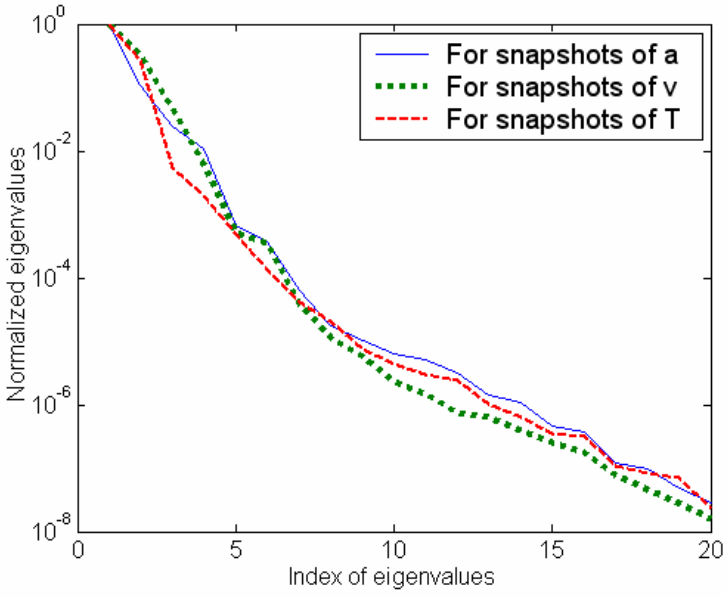

Figure 5-26 Normalized eigenvalues for the snapshots of a'

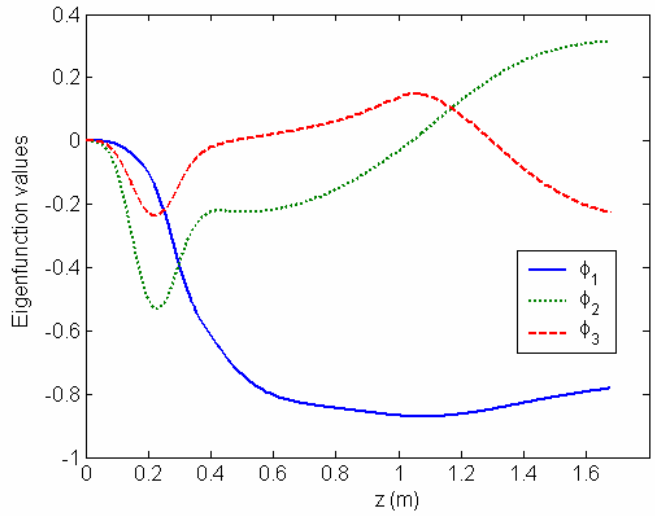

Figure 5-27 The 1st, 2nd and 3rd eigenfunctions for the snapshots of a'

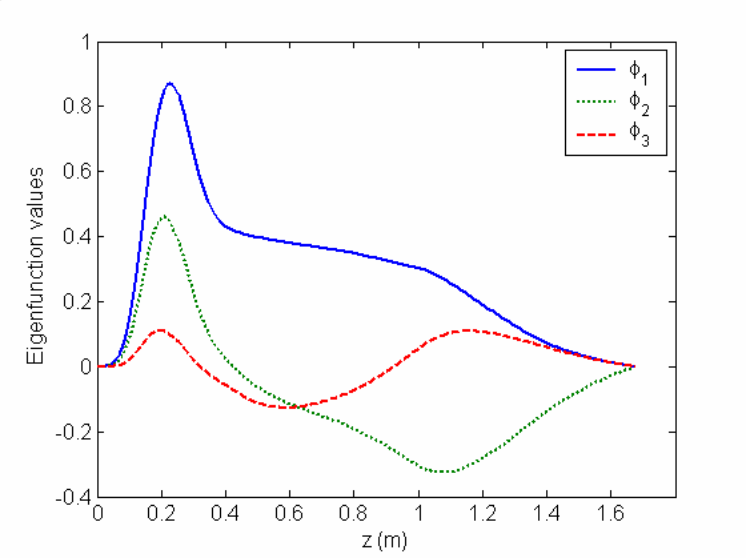

Figure 5-28 The 1st, 2nd and 3rd eigenfunctions for the snapshots of $\hat{v}$

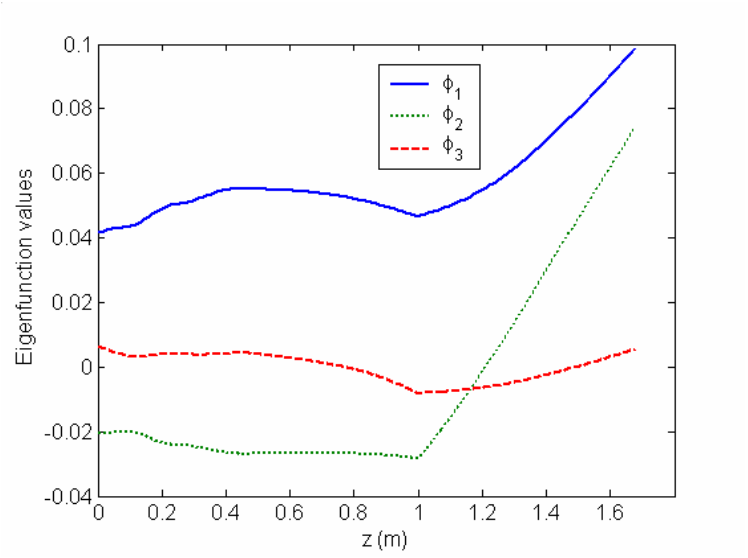

Figure 5-29 The 1st, 2nd and 3rd eigenfunctions for the snapshots of T'

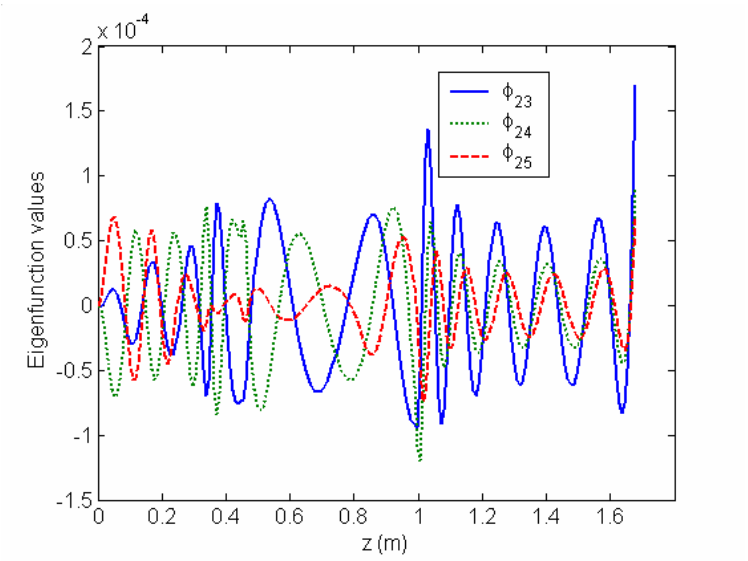

Figure 5-30 The 23rd, 24th and 25th eigenfunctions for the snapshots of a'

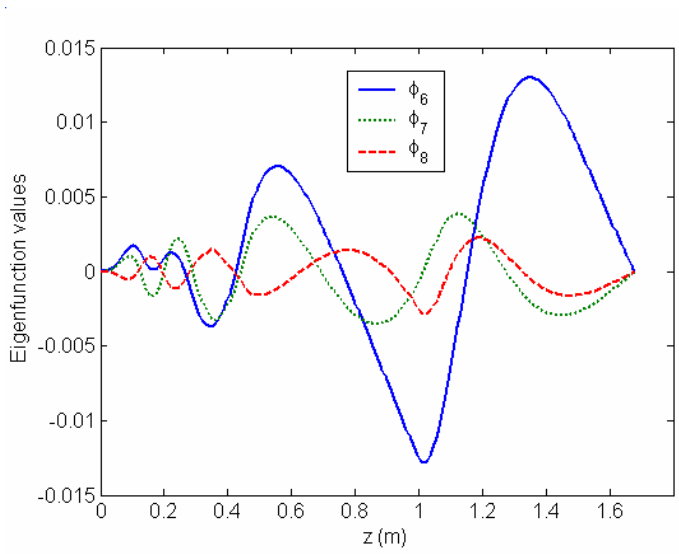

Figure 5-31 The 6th, 7th and 8th eigenfunctions for the snapshots of $\hat{v}$

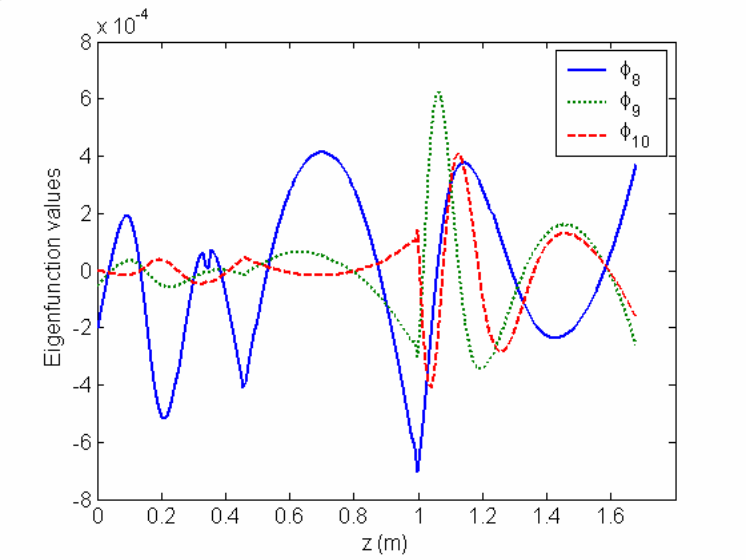

Figure 5-32 The 8th, 9th and 10th eigenfunctions for the snapshots of T'

Figure 5-33 to Figure 5-35 show the step responses of the fiber diameter and tension force to the inputs of v_o', v_i' and q'. The reduced order model matches the nonlinear semi 2-D CFD model well in the transient responses to small perturbations. It is also noticed that the dynamic responses of the system to the inputs of v_i' and q' are much slower than that to the input of v_o'. Hence, the effect of the high frequency disturbances such as the fluctuation of h' can only be attenuated by manipulating the draw speed.

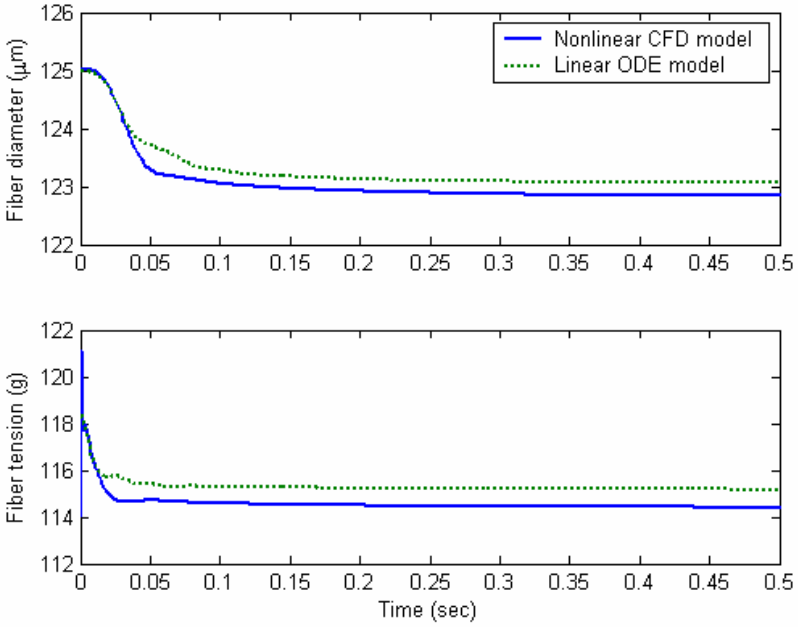

Figure 5-33 Responses to draw speed step input ($v_o' = 0.04$)

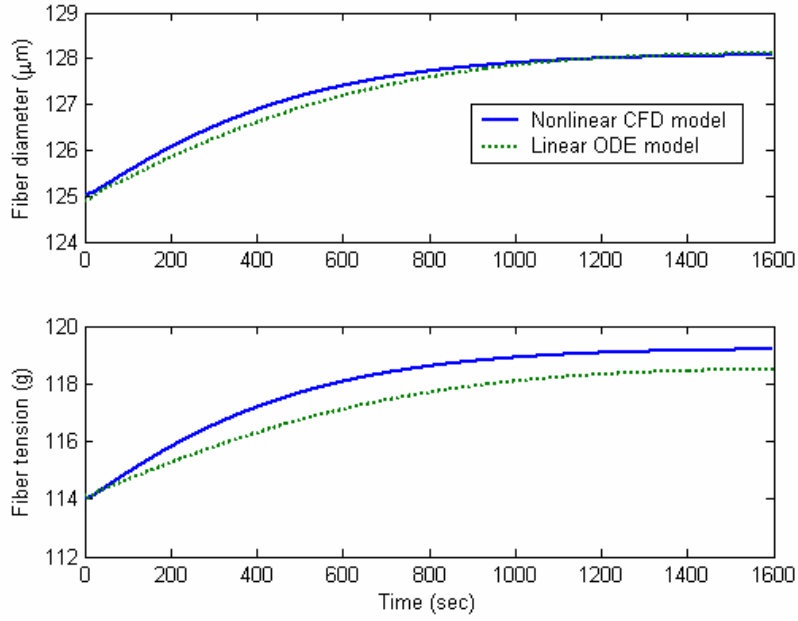

Figure 5-34 Responses to feed rate step input ($v_i' = 0.05$)

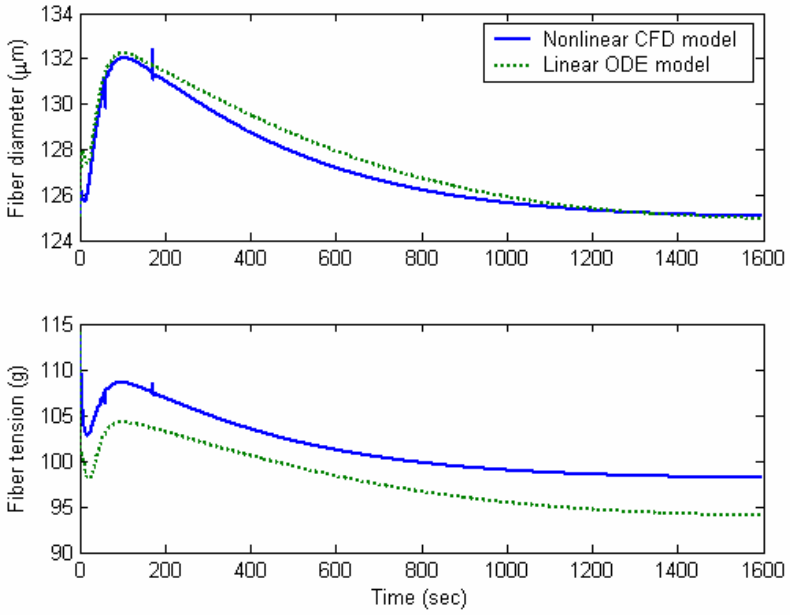

Figure 5-35 Responses to irradiation step input ($q' = 0.02$)

5.3.2 Close-Loop Simulations

The dynamic semi 2-D CFD model is used in the close-loop simulations. The superior performance of robust control system is demonstrated by comparing with the open-loop responses.

The detailed computation procedure is given below:

Step 1: Specify the initial conditions.

Step 2: Assume the value of $a(z)$, $v(z)$ and $T(z)$ for the current time step; solve Equation (4-1) and (4-2) to obtain the 1-D axial velocity $v(z)$; calculate the radial velocity component by $u = -0.5r\,dv/dz$ so that the 2-D continuity equation (Equation (3-7)) is satisfied.

Step 3: Solve the RTE, then substitute $\nabla \cdot \mathbf{q}_R$, v and u into Equation (3-10) to solve for the 2-D temperature field.

Step 4: Calculate the radially lumped temperature

$$\overline{T}(z) = \frac{2}{R^2(z)} \int_0^{R(z)} T(r,z) r dr \tag{5-3}$$

which is used to update the viscosity $\mu(T)$, then go back to Step 2 until the relative changes of v and T between two adjacent iterations are less than 10^{-6}.

Step 5: Calculate the outputs $\mathbf{y} = \left[a'(L,t) \quad T'(L,t)\right]^T$ and feed them to the controller (Equation (4-84)) to compute the manipulating inputs for the next time step. The elements of the input vector **u** are substituted into Equations (4-62) ~ (4-64) to obtain the updated v_o', v_i' and q', which specify the new boundary conditions for the glass velocity and the furnace heat flux. At the same time, the disturbance of h' is added to $\overline{h}$. Finally, save the values of the state variables at the current time step, forward the simulation time by Δt, and go back to Step 2 until the end of the simulation period is reached.

In the following close-loop simulations, the tunable weights (εi, i =1,..,9) in the controller design are chosen to be (0.5, 0.005, 0.001, 0.001, 0.5, 0.5, 0.5, 0.001, 0.001). The orders of magnitude of the time constants for the actuators are τ_o ~ 0.001s, τ_i ~ 1s and τ_q ~180s. The sampling time step is 0.001s.

Two disturbance inputs are considered separately: 1) a white noise fluctuation of $h'(t)$ is added to $\overline{h}(z)$ to simulate the disturbance in q''_{conv}; 2) a white noise fluctuation of w_o is superposed to the winder motor actuating input u_o to simulate the mechanical

vibration or other sources of disturbances. The responses to the disturbances are summarized in Table 5-4, where D_f is the fiber diameter and F_t is the fiber tension force. The white noise of $h'(t)$, the responses of fiber diameter and the manipulating draw speed in the close-loop system under the disturbance of $h'(t)$ are plotted in Figure 5-36 to Figure 5-38, respectively. The white noise of w_o, the responses of fiber diameter and the manipulating draw speed in the close-loop system under the disturbance of w_o are plotted in Figure 5-39 to Figure 5-41. The fiber diameter fluctuation in the close-loop system using the robust controller is much smaller than that in the open-loop system. More than 50% decrease in the fiber diameter fluctuations is observed. The fiber tension fluctuation and the draw speed variation in the close-loop system are also kept small.

Due to the inertia of the spool, the time constant of the draw-speed-control motor may be much larger than 1ms. To see the effect of the large motor time constant on the close-loop system performance, τ_o is increased to 50ms and the controller is redesigned. The responses to disturbance of $h'(t)$ are compared between two systems of different τ_o in Table 5-5 and Figure 5-43. The close-loop system with a τ_o of 50ms performs as well as that with a τ_o of 1ms. This is due to the fact that the high viscosity hampers the fiber diameter fluctuation in response to the high frequency disturbances so that the motor is fast enough to compensate the sensed fluctuations.

Table 5-4 Summary of responses to disturbances of $h'(t)$ and w_o

	(standard deviation, maximum deviation)			
	D_f (μm) Open-loop	D_f (μm) Close-loop	F_t (%) Close-loop	v_o (m/s) Close-loop
$h'(t)$	(0.32, 0.90)	(0.14, 0.46)	(3.9, 11)	(0.80, 2.5)
w_o	(0.27, 0.83)	(0.090, 0.28)	(1.87, 5.4)	(0.42, 1.26)

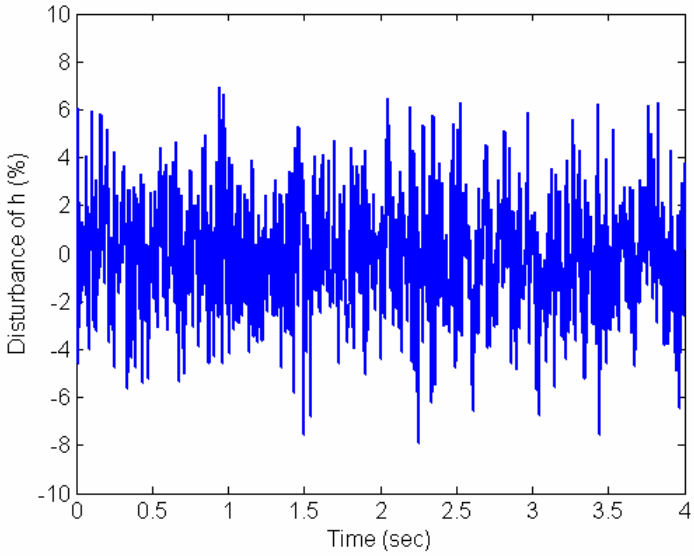

Figure 5-36 White noise disturbance of air convection

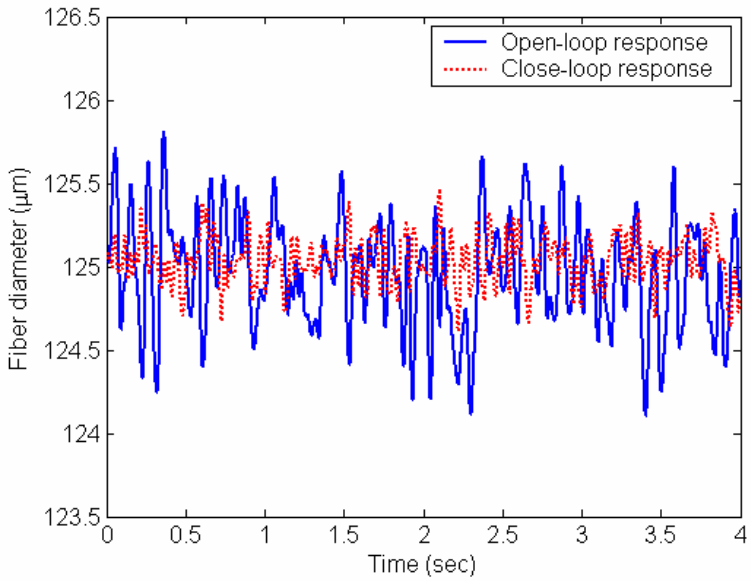

Figure 5-37 Responses of fiber diameter to the disturbance of $h'(t)$

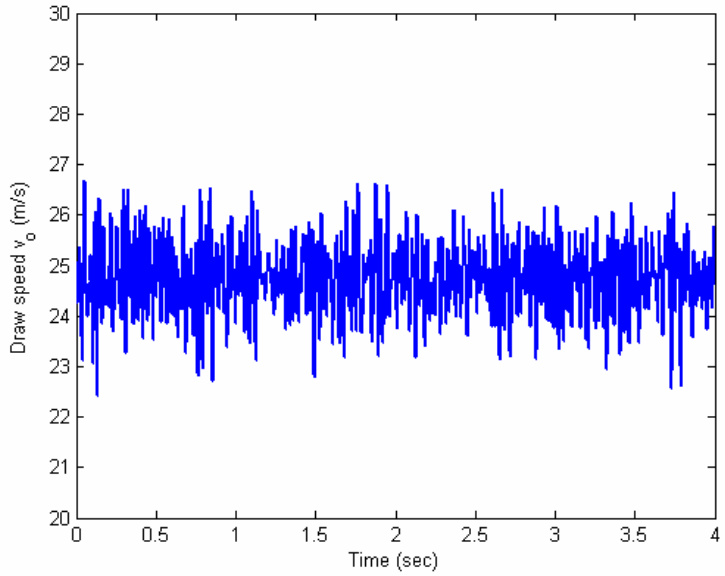

Figure 5-38 Manipulating draw speed under the disturbance of $h'(t)$

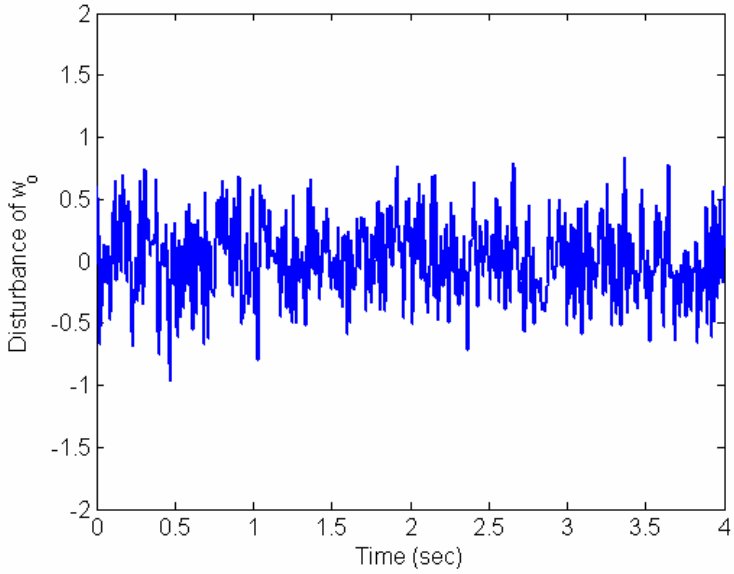

Figure 5-39 White noise disturbance of winder motor vibration w_o

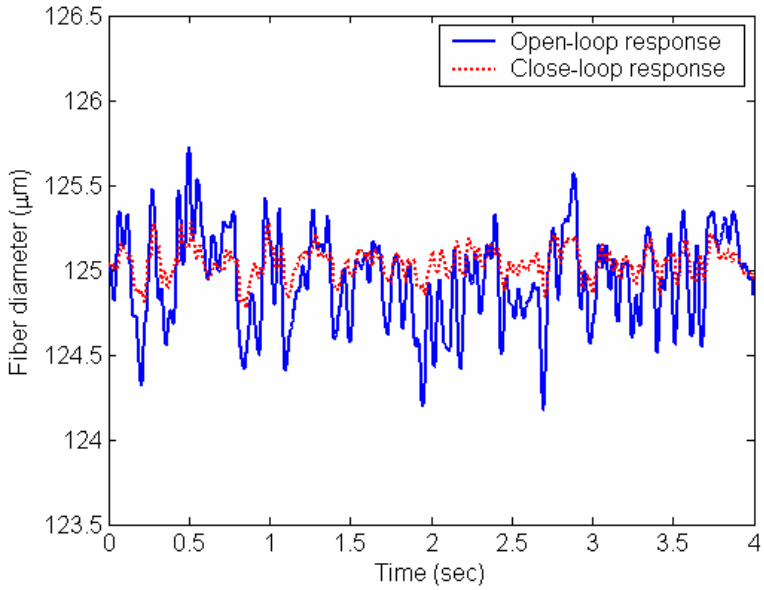

Figure 5-40 Responses of fiber diameter to the disturbance of w_o

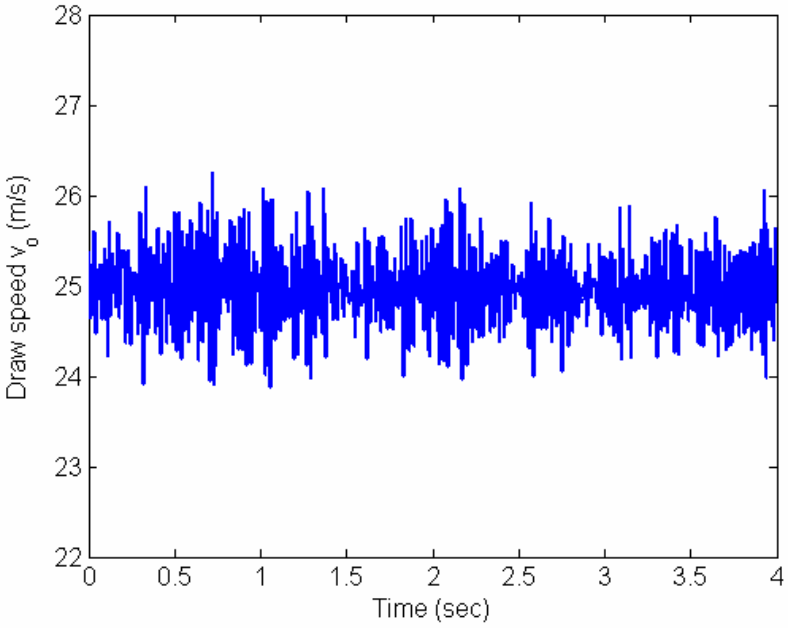

Figure 5-41 Manipulating draw speed under the disturbance of w_o

Table 5-5 Effects of τ_o on close-loop system responses to the disturbance of $h'(t)$

τ_o (ms)	(standard deviation, maximum deviation)		
	D_f (μm)	F_t (%)	v_o (m/s)
1	(0.14, 0.46)	(3.9, 11)	(0.80, 2.5)
50	(0.16, 0.48)	(3.6, 12)	(0.85, 2.6)

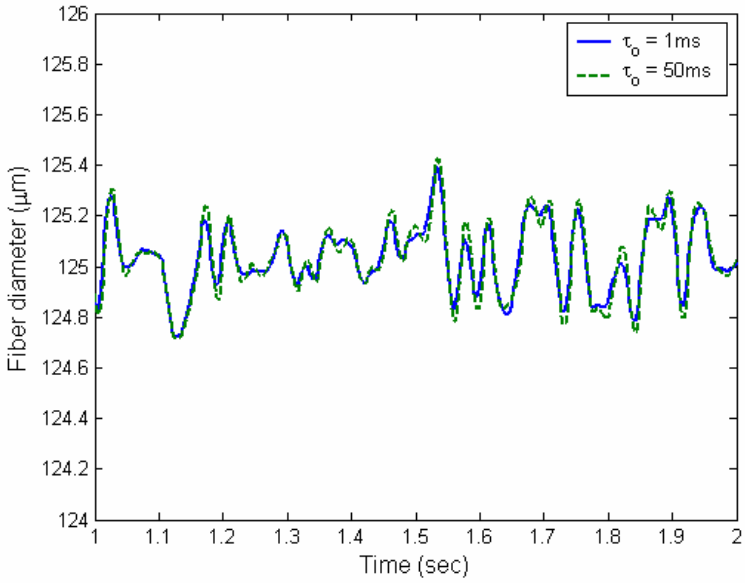

Figure 5-42 Effects of τ_o on close-loop responses of fiber diameter to the disturbance of $h'(t)$

5.3.3 Robustness Studies

Some robustness of the controller has been demonstrated in the above simulations using the dynamic 2-D CFD model since the design is based on the linear ROM. Although the CFD model is validated by some measurements, there are still possible modeling errors in the values of critical parameters and material properties, the effects of which on the close-loop performance should be studied. The most possible modeling errors include: the air convection heat transfer coefficient, the furnace temperature, the glass viscosity, and the glass absorption coefficient. These modeling errors can alter the steady state response and the transient snapshots of the variables used for deriving the

ROM. In the following robustness studies, the responses of the open-loop and close-loop systems subject to the white noise disturbance in h' are simulated using the 2-D CFD model when each modeling error is considered. The standard deviation (STD) of the fiber diameter in the simulations are summarized in

Table 5-6 Fiber diameter fluctuations in the robustness studies

Modeling error	STD of fiber diameter (μm)	
	Open-loop	Close-loop
10% underestimation of $\bar{h}$	0.3531	0.1560
30K overestimation of T_f	0.3424	0.1308
10% underestimation of μ	0.3580	0.1705
50% underestimation κ_1	0.3475	0.1911
Combination of above errors	0.2735	0.1376

Air convective heat transfer coefficient

The nominal $\bar{h}$ is obtained from the 2-D numerical solution of the air boundary layer flow around the glass cylinder in the chamber. This solution is subject to modeling errors since an algebraic turbulence model is used and there are no reliable experimental or theoretical results on when the laminar boundary layer around the slim moving cylinder turns into turbulence. In order to test the robustness of the controller subject to this modeling error, the nominal $\bar{h}$ is increased by 10%. The simulation starts from the steady state at the nominal conditions so that it also shows the response to a biased disturbance in h.

Figure 5-43 compares the open-loop and close-loop responses of the fiber diameter, which shows that the disturbance attenuation capability of the close-loop system is not affected by the 10% modeling error in h. It also shows that although the

open-loop system is stable, it takes a much longer time for the fiber diameter to come back to the specified steady state value when a step disturbance of h is applied. The close-loop responses of the fiber tension and the manipulating draw speed are shown in Figure 5-44 and Figure 5-45, respectively. It is shown that the draw speed is also biased during the transient in order to compensate the effect of the step disturbance.

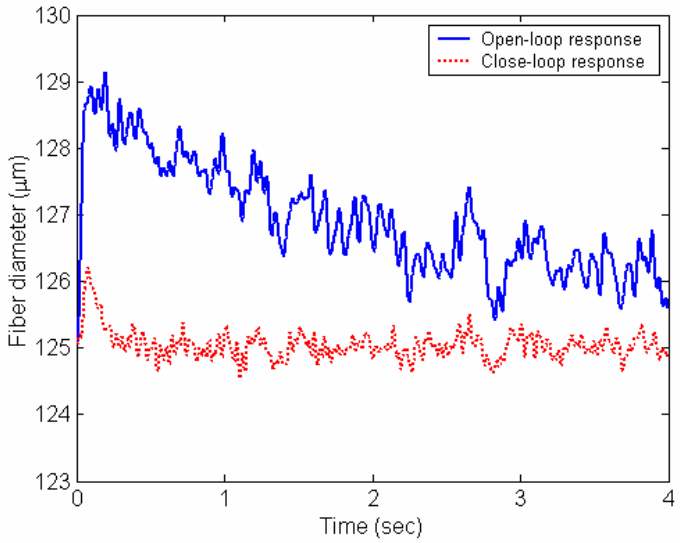

Figure 5-43 Responses of fiber diameter to the 10% increase in h

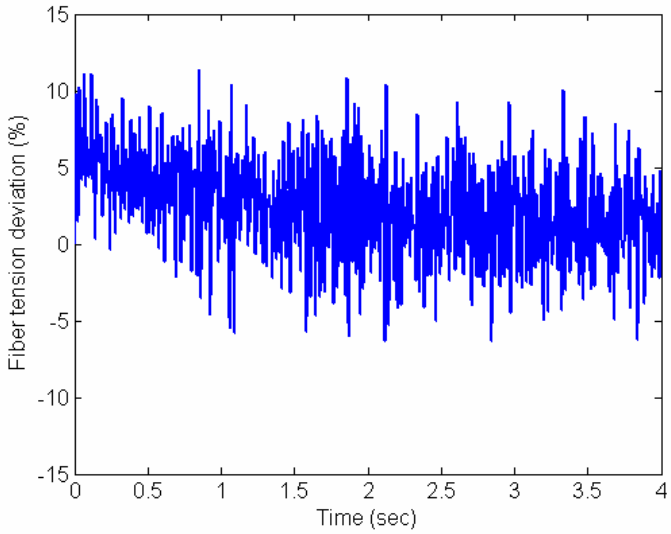

Figure 5-44 Close-loop response of fiber tension to the 10% increase in h

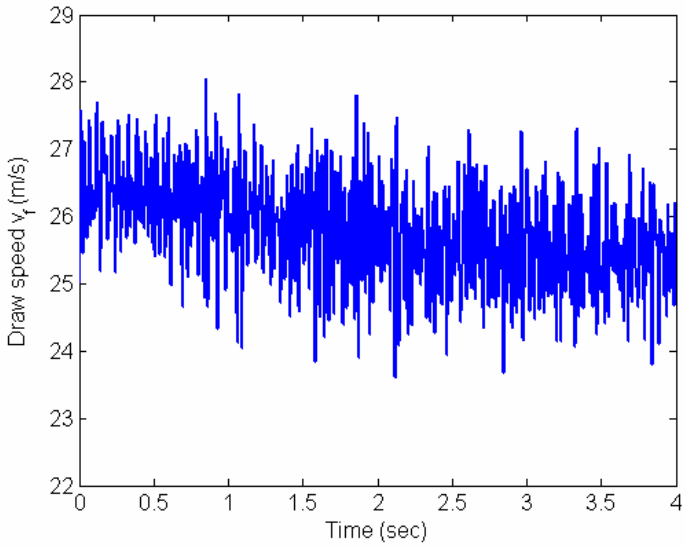

Figure 5-45 Manipulating draw speed response to the 10% increase in *h*

Furnace temperature

The furnace temperature used in the full model simulation is measured by an infrared thermometer (MIKRON M90V) when there is no preform inside the furnace. The existence of a preform in the furnace may induce an offset on the furnace temperature profile. As the camera has to be outside the furnace during the measurement, the long distance between the camera and the measuring points and the limitation on the focusing capability of the camera may also induce some measuring errors due to the averaging effect. In order to test the robustness of the controller under these measuring errors, the furnace temperature is decreased by 30K in the simulation. The simulation starts from the steady state at the nominal conditions so that it also shows the response to a step disturbance in T_f.

Figure 5-46 compares the responses of the open-loop and the close-loop systems in the first 4 seconds. It shows that the open-loop system responds slowly to the furnace temperature step change, and hence the slowly varying content in the fiber diameter can

be easily eliminated by the fast controller. The fast varying content in the fiber diameter due to the white noise in h is also effectively attenuated in the close-loop system under the modeling error. As shown in Figure 5-47 for the close-loop response of the fiber tension, the fast varying content is still restrained within ±10%; but the fiber tension is slowly increasing due to the furnace temperature decrease, which can be easily eliminated by controlling the furnace temperature using tension feedback.

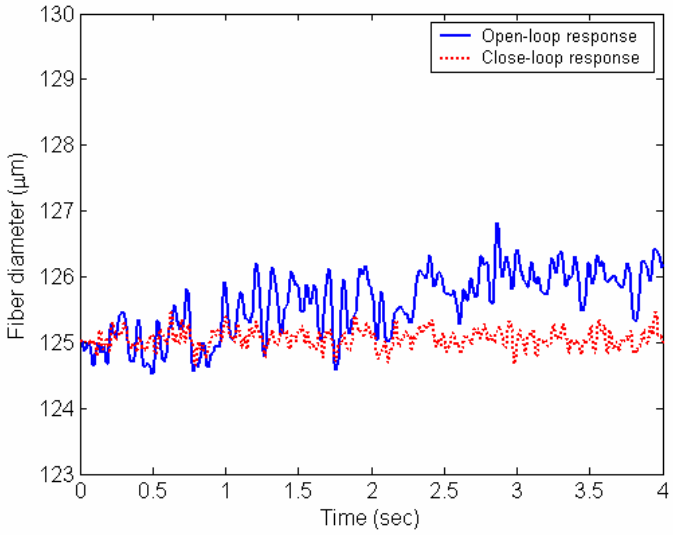

Figure 5-46 Responses of fiber diameter to the 30K decrease in T_f

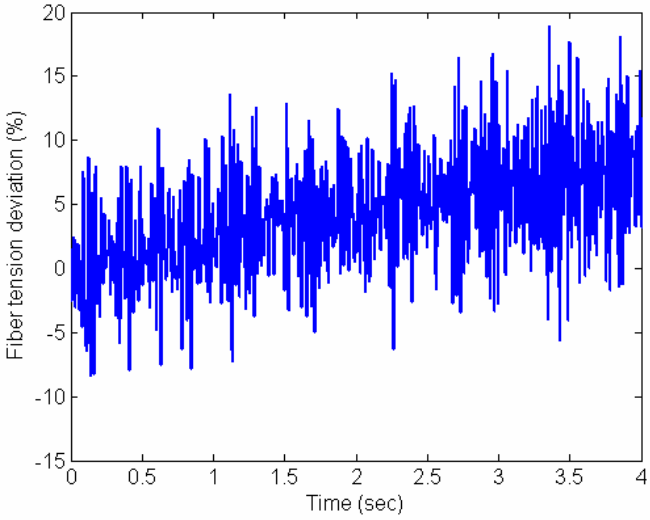

Figure 5-47 Close-loop response of fiber tension to the 30K decrease in T_f

The glass viscosity

The glass viscosity used in the model may deviate from the actual value due to the actual composition of the glass material and the measuring errors in obtaining the correlation. Figure 5-48 shows the responses of the fiber diameter subject to a 10% modeling error in the glass viscosity. The fiber tension response in the close-loop system is shown in Figure 5-49. The close-loop system is robust under the modeling error in the glass viscosity as shown in the figures.

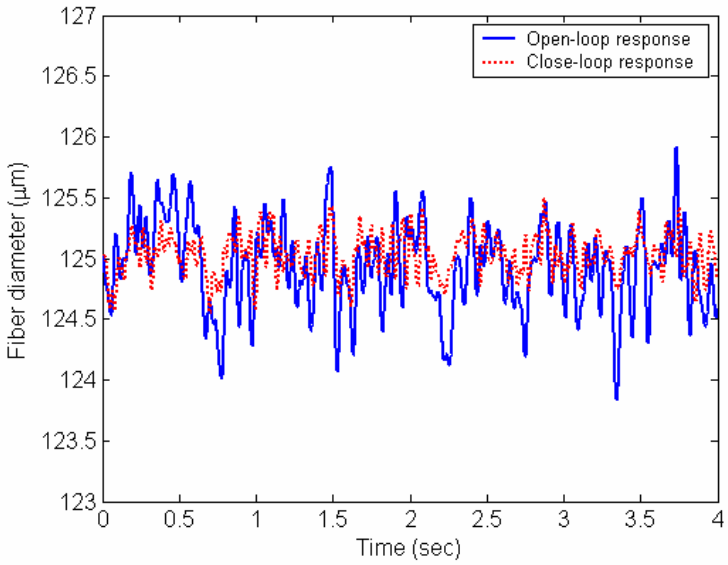

Figure 5-48 Responses of fiber diameter subject to 10% error in the glass viscosity

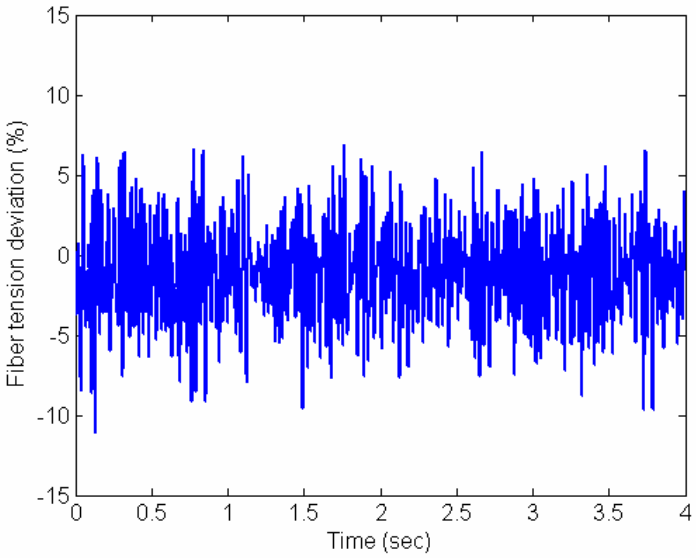

Figure 5-49 Close-loop response of fiber tension subject to 10% modeling error in the glass viscosity

Glass absorption coefficient

The absorption coefficient, especially at the small wavelength band, has significant effect on the radiative transfer and consequently the temperature field of the glass. Since the high temperature measurement of the absorption coefficient is not available, the value that we use was obtained from room temperature measurement data which may deviate from the high temperature values. In order to study the robustness of the controller subject to this modeling error, the first band absorption coefficient is increased by 50% in the simulation. Figure 5-50 and Figure 5-51 show the responses of the fiber diameter and tension force, respectively. As shown in the figures, the close-loop system is robust and performs well subject to the existence of the modeling error.

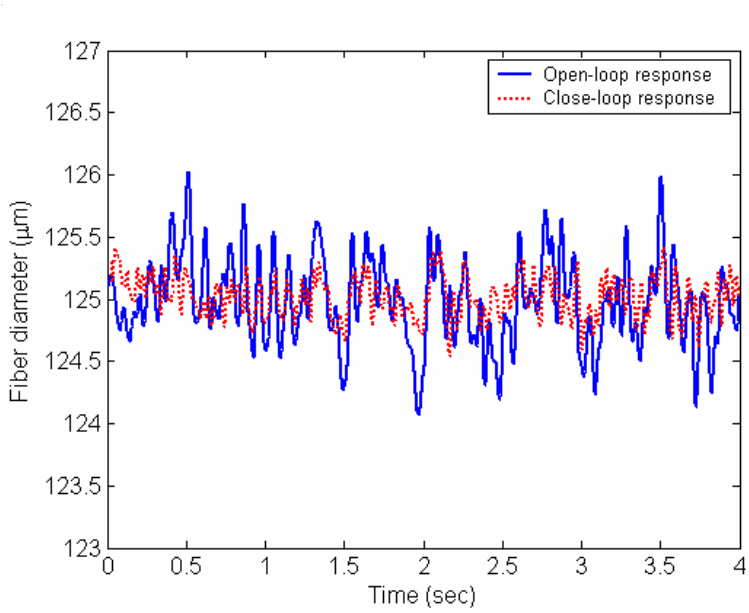

Figure 5-50 Responses of fiber diameter subject to 50% modeling error in the first band glass absorption coefficient

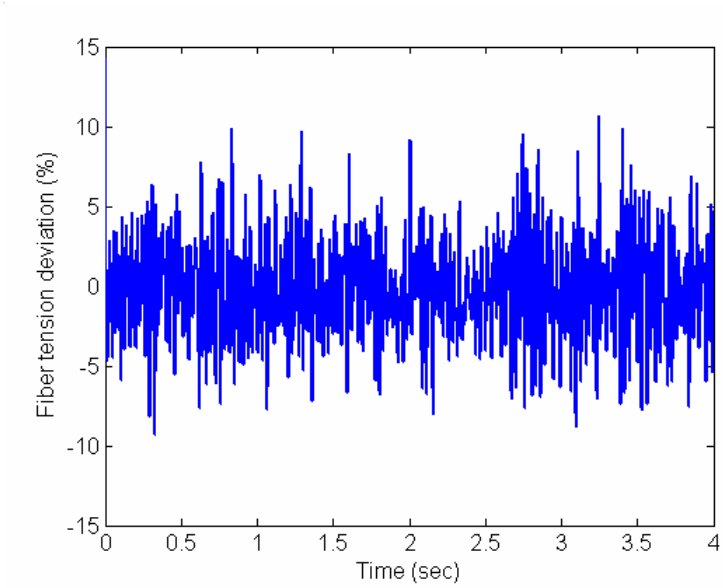

Figure 5-51 Close-loop response of fiber tension subject to 50% modeling error in the first band glass absorption coefficient

The combination of modeling errors

Since some or all of the above mentioned modeling errors may exist at the same time, it is necessary to study the robustness of the controller subject to the combination of these modeling errors. In the following simulation, the modeling errors considered include: 10% underestimation of h, 20K underestimation of T_f, 10% underestimation of μ and 50% underestimation of κ_λ at the small wavelength band. The responses of the fiber diameter, the tension force, and the draw speed are shown in Figure 5-52 to Figure 5-54. As shown in the figures, the close-loop system is still robust and performs well under the combination of the modeling errors.

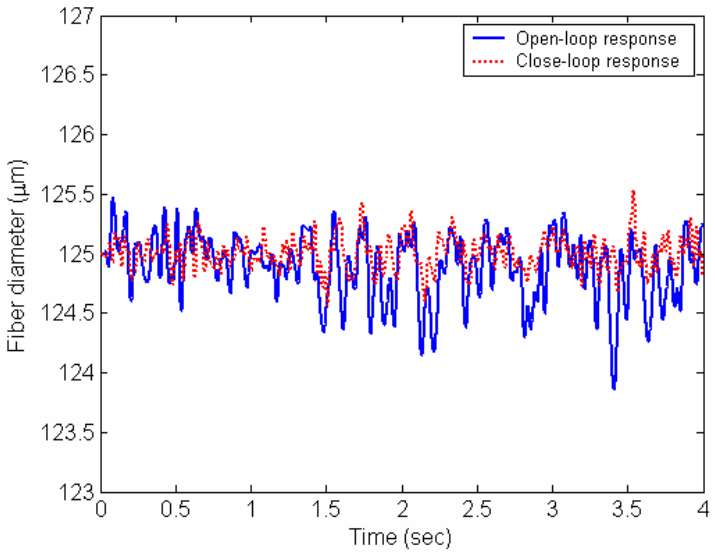

Figure 5-52 Responses of fiber diameter subject to the combination of modeling errors

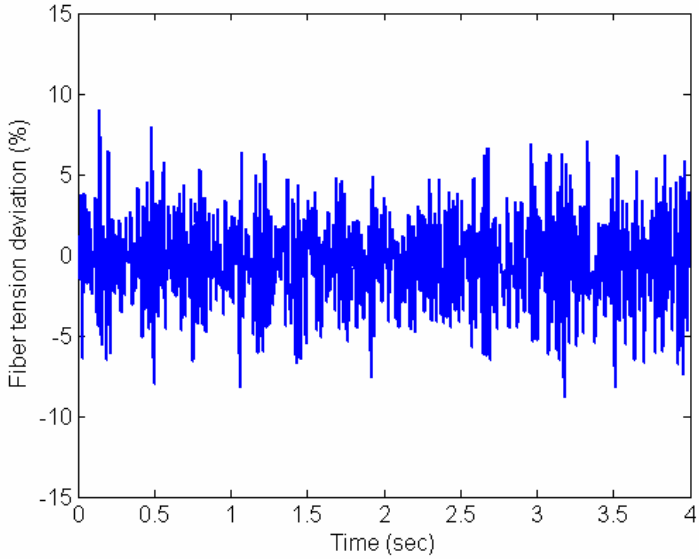

Figure 5-53 Close-loop response of fiber tension subject to the combination of modeling errors

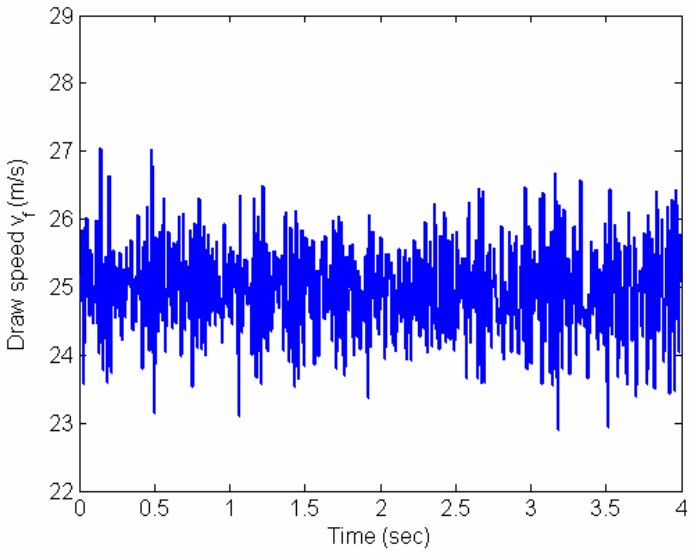

Figure 5-54 Manipulating draw speed subject to the combination of modeling errors

CHAPTER VI

CONCLUSIONS AND FUTURE WORKS

6.1 Conclusions

The modeling and control of a highly temperature coupled and viscous free surface flow with the radiation transfer have been presented, and the approach has been directly applied to the modern optic fiber drawing process where large preforms and high draw speeds are used. The research in this dissertation can be divided into two parts:

(1) Computational modeling and simulations of the thermal-fluid transports.

(2) Reduced order modeling and robust control of the dynamic system.

In part one, both the complete 2-D and semi 2-D numerical models for the modern fiber drawing process were developed. The conclusions of this part are summarized as follows:

(1) We developed the fully conservative form of the 2-D RTE in both curvilinear and cylindrical coordinates systems so that the numerical scheme can be used for arbitrary axisymmetric cylindrical geometries. The RTE was directly solved using the FVM. The boundary condition for the radiation intensities at the free surface was obtained by an enclosure analysis. The numerical solution of the radiation heat flux was shown to be in close match with the exact solutions for a simplified problem. Since the same spatial grid was used in solving the fluid dynamic equations and the RTE, the numerical solution of the RTE was shown to be accurate and efficient.

(2) We considered both the furnace and the post-chamber in solving the conjugate problem of the temperature coupled glass free surface flow and the mixed convection of the air. The staggered grid used in both the glass and the air domains guaranteed strict energy conservation and as a result, a much smaller grid number than those used in the previous studies was needed for a even larger and longer preform. The staggered grid also offered a convenient way to implement the free surface boundary conditions. The numerical solution of the mixed convection of the air in the post-chamber showed that the calculated convective heat flux along the free surface is sensitive to the size of the grids within the boundary layer, especially of those at the vicinity of the fiber since the fiber has a small diameter but a high moving speed.

(3) The comparisons between our predictions against experimentally measured neck-down profiles drawn at high draw speeds validated both the complete 2-D and the semi 2-D models. The comparisons between the complete 2-D and the semi 2-D models further verified that the semi 2-D model offers an accurate and efficient way to simulate the modern draw process for preform diameters up to 9cm and draw speeds up to 35m/s.

(4) The steady state simulations showed that the fluid flow of the melting glass is close to 1-D even at the neck-down region, while the temperature distribution has some 2-D characteristics. Although the radial variation of the axial velocity component is not significant, its effect is dramatic in predicting the effect of a thin flat gap originally in the preform core on the final fiber. The simulations using the semi 2-D model showed that the location of glass solidification determined by

the glass diameter was consistent with that determined by locating the glass temperature equal to its melting temperature (1580ºC). When the draw speed is higher, the neck-down profile is stretched downward and the glass solidification location is lower in or even out of the post-chamber.

In part two, we applied the K-L expansion with the Galerkin scheme in the reduced order modeling of multi-variable distributed systems such as the fiber drawing process with nonlinear and coupled dynamics. A quasi 1-D fluid dynamic model was developed first, which is accurate around the neighborhood of the nominal equilibrium state. The nonlinear PDE's were then perturbed around the steady state solution obtained from the 2-D CFD model to get a linear form. There are three distributed state variables in the system: glass diameter, axial velocity and temperature. The variables are strongly coupled with each other as already shown in the simulations in part one. K-L decomposition was applied to the transient simulation data obtained from the dynamic CFD model to obtain a set of optimal numerical eigenfunctions for each distributed state variables. The numerical eigenfunctions were then used as the basis functions in the Galerkin's procedure on the linear PDEs to obtain the reduced order ODE's. As the governing equations for the velocity and temperature are parabolic type, the dominant dynamics of the variables are characterized by a small number of degrees of freedom. The continuity equation that governs the glass diameter is close to the hyperbolic type, which requires more eigenmodes to accurately describe the dynamics. The simulations showed that the reduced order model closely catches the transient dynamics of the system as the CFD model. Finally, mixed H_∞/LQG controller was designed on the basis of the

reduced order model. The close-loop control was demonstrated to be robust and superior to the open-loop system.

6.2 Future Works

This research work has made several contributions as summarized in Section 1.5. Yet there are still several issues to be addressed in the future works.

(1) In this study, the glass free surface is assumed to be diffuse to both radiation reflections and transmissions since there may be hydrodynamic instabilities that make the surface wavy and the wavelength of the fluctuation is comparable to that of the radiation. But which mechanisms may cause the instabilities and how to determine the onset of the instabilities and the wavelength of the fluctuations are still open questions. Experimental or theoretical works are needed to answer the questions.

(2) In this study, the furnace temperature is measured and used as an input in the simulations. Before the prototyping of the draw facility, the furnace temperature is actually unknown. A model of the induction heating furnace is needed to predict the furnace temperature in the early stage of a new furnace design. The furnace model is also needed in the control of furnace temperature for the regulation of fiber draw tension.

(3) Although the performance of the robust controller has been demonstrated via numerical simulations using the validated semi 2-D CFD model, real experiments on the close-loop system are still needed to further verify the design and the robustness of the controller.

APPENDIX A

FURNACE TEMPERATURE MEASUREMENT AND CALCULATION

A.1 Thermometer

The furnace temperature is measured by a single color IR thermometer - model M90V from MICRON Instrument Company, Inc. The camera is held by a fixture above the furnace and focused on the entrance of the furnace wall through the top opening. The camera is then moved vertically downward and the temperature along the furnace wall is recorded by the computer that is connected to the camera. There is no preform inside the furnace during the measurement so that the view of the camera is not blocked. The measuring range is limited in the furnace chamber since the view of the camera is blocked by the edge of the furnace opening. The calibration function of the thermometer is given by

$$V(T) = K\int_{\lambda_1}^{\lambda_2} C_1\lambda^{-5}e^{-C_2/(\lambda T)}d\lambda \approx KE_{b\lambda}(T)\Delta\lambda \tag{A-1}$$

where

$$E_{b\lambda}(T) = C_1\lambda^{-5}e^{-C_2/(\lambda T)} \tag{A-2}$$

and $\Delta\lambda = (\lambda_2 - \lambda_1) << 1\,\mu m$; V is the voltage signal sensed by the optical sensor; and K is a constant related to the intrinsic parameters of the optical system and the emissivity setting. The single color thermometer measures radiation intensity at the wavelength

of $\lambda = 0.65\mu m$. The above equations are used by the device to convert the voltage signal from the transducer back to temperature.

A.2 Consideration of reflections in the furnace

When we measure the temperature of the furnace, the thermometer actually detects the radiosities of the furnace wall, which consist not only the emissive power given by Equation (A-2), but also the reflection of the radiosities from all the surfaces in the furnace enclosure. Given the temperature output of the thermometer, T', the radiosity can be recovered by Equation (A-2) using $J_\lambda = E_{b\lambda}(T')$. By dividing the furnace wall into *M* small ring elements, the radiosity at element *i* can be given by

$$J_{\lambda,i}(T_i') = \varepsilon_\lambda E_{b\lambda,i}(T_i) + (1-\varepsilon_\lambda)\sum_{j=1}^{M} F_{i-j} J_{\lambda,j}(T_j') \qquad \text{(A-3)}$$

where F_{i-j} is the diffuse view factor from the i^{th} element to the j^{th} element; ε_λ is the emissivity. Given the recovered J_λ, we can solve the blackbody emissive power $E_{b\lambda}$ from the above equation, and then recover the real temperature T_i using Equation (A-2).

In the measurement, we can simply set the emissivity as 1.0. But we need the real emissivity in Equation (A-3). All the following radiation properties are taken from the tabulated data from Touloukian *et al.* (1973). The material of the furnace inner tube is ZrO_2. The average normal spectral emissivity of ZrO_2 at $\lambda = 0.65\mu m$ is 0.6 at T = 1900K ~ 2500K. The average hemispherical spectral emissivity of ZrO_2 is also around 0.6, which shows that the emissivity can be assumed direction independent. The post-chamber has a quartz silica inner tube above the porous aluminum silicate insulator. The normal transmitivity of the quartz at $\lambda = 0.65\mu m$ is above 0.95 for a 6.35mm layer. In

our case the quartz tube is only 2.5mm thick. Hence the tube is approximately transparent at $\lambda = 0.65\mu m$. The aluminum silicate has a normal total emissivity of 0.9 and normal spectral reflectivity of 0.05. Considering the multiple reflections inside the porous material, an apparent emissivity of 1.0 can be used for the post-chamber wall.

Using the above surface emissivities and Equation (A-3)(A-3), the corrected furnace temperature is obtained and compared with the outputs of the thermometer in Figure A-1. The maximum furnace temperature after correction is 22K higher than the thermometer output, while the corrected temperature is about 20~40K lower than the thermometer output at both ends of the furnace. In the post-chamber both temperature are the same due to the unit emissivity.

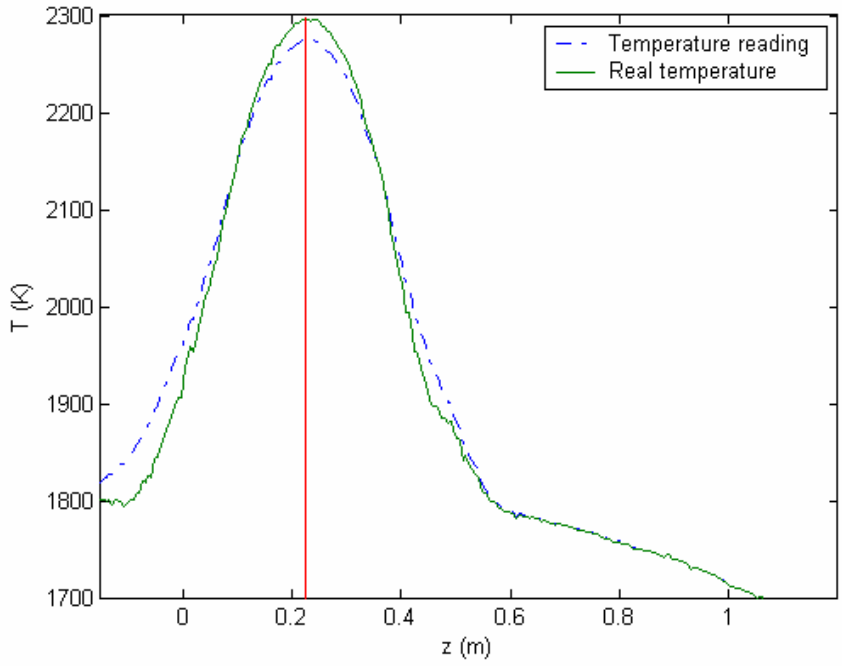

Figure A-1 Furnace temperature distribution (thermometer output and corrected value)

APPENDIX B

RADIATIVE PROPERTIES AND BAND MODEL

The accuracy of the solution to the RTE depends significantly on the knowledge of the radiative properties. Specifically, care must be exercised to appropriately quantify the absorption coefficient of the glass and the reflectivity at the glass surfaces at the operating temperature.

B.1 Band Model and Absorption Coefficient

Due to the spectral dependence of the radiative properties of the glass media, the total spectrum is divided into three bands and average properties are used on each band as shown in Table B-1.

Table B-1 Band model for the absorption coefficients

	Glass media (n_1 = 1.42) λ_1 (um)	Frequency (x 10^{13} Hz)	Air media (n_2 = 1.) λ_2 (um)
Band 1	0.2 ~ 2.8	105.6 ~ 7.545	0.284 ~ 3.976
Band 2	2.8 ~ 4.8	7.545 ~ 4.401	3.976 ~ 6.816
Band 3	4.8 ~ ∞	4.401 ~ 0	6.816 ~ ∞

When the electromagnetic waves of radiation travel from one media to another, the frequencies do not change since the energy of the photon, which is $h\upsilon$ (h is the Planck's constant; ν is the frequency), must be conserved. The wavelength of an electromagnetic wave can be calculated from

$$\lambda = \frac{c}{\nu} = \frac{c_0}{n\nu} \tag{B-1}$$

where λ is the wavelength, c and c_0 is the speed of light in the media and the vacuum, n is the index of the refraction of the media. So the wavelength changes when it travels from one media to another since the indexes of refraction of the media are different. The relationship of the wavelengths of the same wave in two different media is given by

$$\lambda_1 n_1 = \lambda_2 n_2 \tag{B-2}$$

In the furnace draw problem, the furnace wall is bounded by air whose index of refraction is about 1. But n is equal to 1.42 for the glass media. Thus, the wavelength ranges for each band in the two media are different as shown in Table B-1. Care should be taken in the evaluation of the blackbody emissive power for each wavelength band at different media (in our case, glass medium and furnace wall).

The spectral radiative energy is negligible at wavelengths $\lambda < 0.2\mu m$ in the operating temperature range (around 2000K). In the range of $0.2\mu m \le \lambda < 2.8\mu m$, taking the multiple reflections into account, the average internal transmitivity τ_i of a silica glass slab can be calculated from the tabulated data of the apparent slab reflectivity and transmissivity in (Touloukian *et al.*, 1973). With the approximation of

$$\tau_{i,\lambda} = e^{-\kappa_\lambda d} \tag{B-3}$$

where d is the thickness of the slab, the average absorption coefficient for $0.2\mu m \le \lambda < 2.8\mu m$ is determined to be 0.0243 cm^{-1}.

The absorption coefficients of typical glasses near the melting temperature were measured experimentally by Endrys (1999) and Nijnatten, *et al.* (1999); both published data suggest that the absorption coefficient in the $2.8\mu m \le \lambda < 4.8\mu m$ band near melting

temperature is generally 10~25% lower than that at a room temperature of 25°C. In this study, we estimate the absorption coefficient in the $2.8\mu m \le \lambda < 4.8\mu m$ band to be 3.4 cm^{-1}, which is 15% lower than the 4.0 cm^{-1} that has been used by Myers (1989).

For $\lambda > 4.8\mu m$, the absorption coefficient is large and the spectral radiative flux is relatively small. Thus, the glass is considered opaque for that band. The band model is shown in Figure B-1. The optical thicknesses δ_λ for each band based on a rod radius of 4.5cm are given by

$\delta_\lambda = 0.1094$, $0.2\mu m < \lambda \le 2.8\mu m$;

$\delta_\lambda = 15.3$, $2.8\mu m < \lambda \le 4.8\mu m$;

$\delta_\lambda \to \infty$, $4.8\mu m < \lambda$;

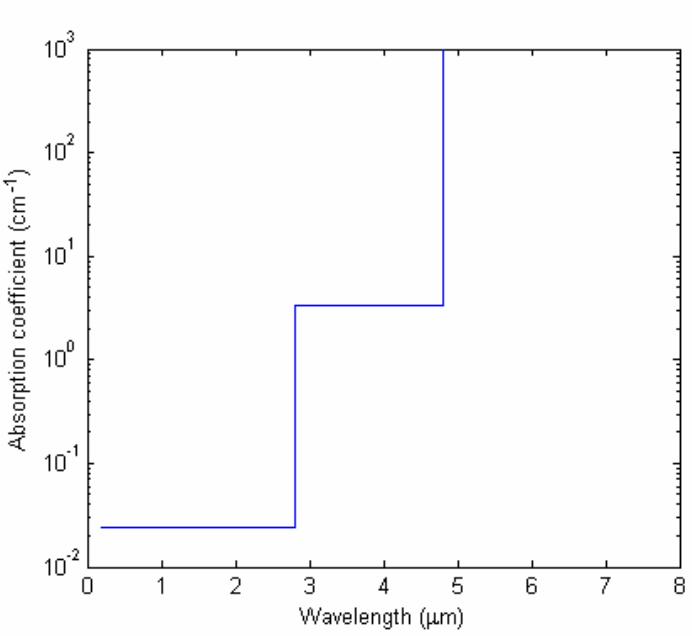

Figure B-1 Band model for absorption coefficient

B.2 Surface Reflectivity

The outer surface reflectivity at the glass free interface can be calculated from the experimentally tabulated data for the air-to-media interface by the following curve fit (Egan and Hilgeman, 1979):

$$\rho^{+} = -0.4399 + 0.7099 \times n_m - 0.3319 \times n_m^2 + 0.0636 \times n_m^3 \tag{B-4}$$

The corresponding inner surface reflectivity for any diffuse media-to-air interface is given by

$$\rho^{-} = 1 - \frac{\left(1 - \rho^{+}\right)}{n_m^2} \tag{B-5}$$

where n_m is the index of refraction of the medium. In this study, an average refractive index over the whole spectrum is used (n_m = 1.42). The consequent reflectivity and transmitivity of the outer surface are 0.08 and 0.92, respectively. Those for the inner surface are 0.54 and 0.46.

APPENDIX C

TURBULENCE MODEL FOR THE AIR CONVECTION

In most part of the post-chamber, the glass moves with a high speed between 5m/s and 25m/s. A boundary layer of the air develops around the continuously moving glass cylinder. The air inside the boundary layer moves in the same direction as the glass. There are few available experimental or theoretical results on the determination of the transition from laminar to turbulent flow in the boundary layer around continuously moving slim cylinders. The critical Reynolds number used for flat plate flow can not be used for this problem since the diameter of the cylinder is small (125μm). Hence, the turbulence transition location has to be assumed in the simulation.

The algebraic mixing-length turbulence model with the empirical correlation of eddy viscosity is used to account for the increased heat transfer due to the turbulence effect. The classical van Driest damping function (van Driest, 1956) is used for the "law-of-the-wall" inner region, while in the "wake-like" log-law zone, the following empirical eddy viscosity (Lueptow and Leehey, 1986) is used

$$\mu_T = c\rho\delta U_\tau \tag{C-1}$$

where δ is the local boundary layer thickness. The friction velocity U_τ is calculated by substituting the experimental velocity profile U into the momentum integral relation for an axisymmetric boundary layer (Lueptow, *et al.* 1985),

$$\left(\frac{U_\tau}{U_\infty}\right)^2 = \frac{d}{dx}\int_R^{R+\delta}\left[\frac{U}{U_\infty}\left(1-\frac{U}{U_\infty}\right)\left(\frac{r}{R}\right)\right]dr \tag{C-2}$$

where U_∞ is the glass moving speed. The empirical coefficient c is close to a constant at 0.0274 by measuring the Reynolds stress and mean velocity profile on a suspended slim cylinder. The eddy conductivity k_T for heat transfer can be obtained by using the above eddy viscosity and the following turbulent *Prandtl* number:

$$\mathrm{Pr}_T = \frac{\mu_T C_p}{k_T} \approx 1 \tag{C-3}$$

The eddy viscosity and eddy conductivity are added to the laminar viscosity and conductivity, respectively, in the fluid dynamic equations to account for the turbulence effects.

APPENDIX D

CURVILINEAR COORDINATES TRANSFORMATION

In the curvilinear coordinates transformation, the physical cylindrical domain with a neck-down free interface is transformed into a computational rectangular domain as shown in Figure D-1. The physical coordinates (*r, z*) are mapped into the curvilinear coordinates (η, ξ). The detailed method of transformation can be found in Tchikanda (2001). Here we only present the transformed equations.

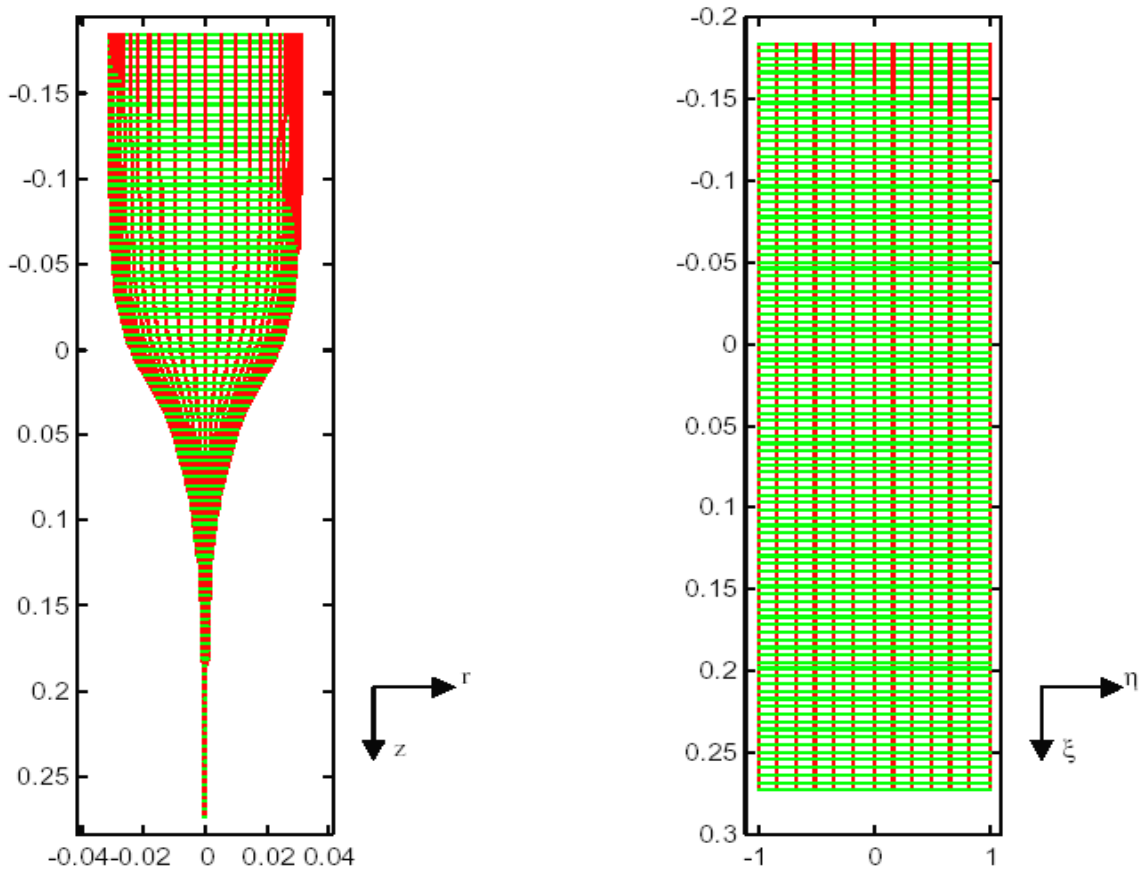

(a) Physical domain (b) Computational domain

Figure D-1 Projection of the physical geometry onto the computational domain

D.1 Glass Domain

The continuity, momentum and energy equations for the glass domain given by Equation (3-7) ~ (3-10) are cast into the fully conservative form in a general curvilinear coordinate system (η, ξ) as follows:

$$\frac{\partial}{\partial \eta}\left(\frac{U}{J}\right)+\frac{\partial}{\partial \xi}\left(\frac{V}{J}\right)=S_p \tag{D-1}$$

$$\begin{aligned}&\frac{\partial}{\partial t}\left(\frac{u}{J}\right)+\frac{\partial}{\partial \eta}\left[\frac{(U+\eta_t)u}{J}\right]+\frac{\partial}{\partial \xi}\left[\frac{(V+\xi_t)u}{J}\right]=-\left[\frac{\partial}{\partial \eta}\left(\frac{\eta_r}{J}p\right)+\frac{\partial}{\partial \xi}\left(\frac{\xi_r}{J}p\right)\right]\\&+\frac{1}{\mathrm{Re}}\left\{\frac{\partial}{\partial \eta}\left[\frac{\mu}{J}\left(g^{11}\frac{\partial u}{\partial \eta}+g^{12}\frac{\partial u}{\partial \xi}\right)\right]+\frac{\partial}{\partial \xi}\left[\frac{\mu}{J}\left(g^{12}\frac{\partial u}{\partial \eta}+g^{22}\frac{\partial u}{\partial \xi}\right)\right]\right\}+S_u\end{aligned} \tag{D-2}$$

$$\begin{aligned}&\frac{\partial}{\partial t}\left(\frac{v}{J}\right)+\frac{\partial}{\partial \eta}\left[\frac{(U+\eta_t)v}{J}\right]+\frac{\partial}{\partial \xi}\left[\frac{(V+\xi_t)v}{J}\right]=-\left[\frac{\partial}{\partial \eta}\left(\frac{\eta_z}{J}p\right)+\frac{\partial}{\partial \xi}\left(\frac{\xi_z}{J}p\right)\right]\\&+\frac{1}{\mathrm{Re}}\left\{\frac{\partial}{\partial \eta}\left[\frac{\mu}{J}\left(g^{11}\frac{\partial v}{\partial \eta}+g^{12}\frac{\partial v}{\partial \xi}\right)\right]+\frac{\partial}{\partial \xi}\left[\frac{\mu}{J}\left(g^{12}\frac{\partial v}{\partial \eta}+g^{22}\frac{\partial v}{\partial \xi}\right)\right]\right\}+S_v\end{aligned} \tag{D-3}$$

$$\begin{aligned}&C_p\left\{\frac{\partial}{\partial t}\left(\frac{T}{J}\right)+\frac{\partial}{\partial \eta}\left[\frac{(U+\eta_t)T}{J}\right]+\frac{\partial}{\partial \xi}\left[\frac{(V+\xi_t)T}{J}\right]\right\}=\\&\frac{1}{Pe}\left\{\frac{\partial}{\partial \eta}\left[\frac{k}{J}\left(g^{11}\frac{\partial T}{\partial \eta}+g^{12}\frac{\partial T}{\partial \xi}\right)\right]+\frac{\partial}{\partial \xi}\left[\frac{k}{J}\left(g^{12}\frac{\partial T}{\partial \eta}+g^{22}\frac{\partial T}{\partial \xi}\right)\right]\right\}+S_T\end{aligned} \tag{D-4}$$

where the source terms are given by

$$S_p=-\frac{1}{J}\frac{u}{r} \tag{D-5}$$

$$S_u=\frac{1}{J\,\mathrm{Re}}\left[\left(\frac{\mu}{r}+\frac{\partial \mu}{\partial r}\right)\left(\eta_r\frac{\partial u}{\partial \eta}+\xi_r\frac{\partial u}{\partial \xi}\right)-\frac{\mu u}{r^2}+\frac{\partial \mu}{\partial z}\left(\eta_r\frac{\partial v}{\partial \eta}+\xi_r\frac{\partial v}{\partial \xi}\right)\right]-\frac{u^2}{rJ} \tag{D-6}$$

$$S_v = \frac{1}{J\,\mathrm{Re}}\left[\frac{\partial \mu}{\partial r}\left(\eta_z \frac{\partial u}{\partial \eta} + \xi_z \frac{\partial u}{\partial \xi}\right) + \frac{\mu}{r}\left(\eta_r \frac{\partial v}{\partial \eta} + \xi_r \frac{\partial v}{\partial \xi}\right) + \frac{\partial \mu}{\partial z}\left(\eta_z \frac{\partial v}{\partial \eta} + \xi_z \frac{\partial v}{\partial \xi}\right)\right] - \frac{uv}{rJ} + \frac{1}{JFr} \tag{D-7}$$

$$S_T = \frac{k}{rJPe}\left(\eta_r \frac{\partial T}{\partial \eta} + \xi_r \frac{\partial T}{\partial \xi}\right) - C_p \frac{uT}{rJ} - \frac{\nabla \cdot q_R}{J} + \frac{Ec}{J\,\mathrm{Re}}\mu\Phi \tag{D-8}$$

and where the contravariant velocity components U and V are given by

$$U = \eta_r u + \eta_z v \tag{D-9}$$

$$V = \xi_r u + \xi_z v \tag{D-10}$$

and the components of the contravariant metric tensor g^{11}, g^{12} and g^{22} are given by

$$\begin{aligned} g^{11} &= \eta_r^2 + \eta_z^2 \\ g^{12} &= \eta_r \xi_r + \eta_z \xi_z \\ g^{22} &= \xi_r^2 + \xi_z^2 \end{aligned} \tag{D-11}$$

The free surface boundary conditions given by Equations (3-18) ~ (3-20) involve several spatial differentiations. Hence, they also need to be transformed into curvilinear coordinate system.

The normal and tangential components of the velocity at the free surface can be defined as

$$V_n = \mathbf{v} \cdot \mathbf{n} = u\frac{\eta_r}{\sqrt{g^{11}}} + v\frac{\eta_z}{\sqrt{g^{11}}} \tag{D-12}$$

$$V_t = \mathbf{v} \cdot \mathbf{t} = -u\frac{\eta_z}{\sqrt{g^{11}}} + v\frac{\eta_r}{\sqrt{g^{11}}} \tag{D-13}$$

where the normal and tangential unit vectors at the free surface are given by

$$\mathbf{n} = \begin{pmatrix} n_r & n_z \end{pmatrix}^T = \left(\frac{\eta_r}{\sqrt{g^{11}}} \quad \frac{\eta_z}{\sqrt{g^{11}}} \right)^T \tag{D-14}$$

$$\mathbf{t} = \begin{pmatrix} t_r & t_z \end{pmatrix}^T = \left(-\frac{\eta_z}{\sqrt{g^{11}}} \quad \frac{\eta_r}{\sqrt{g^{11}}} \right)^T \tag{D-15}$$

Substituting Equations (D-12) ~ (D-15) into Equations (3-18) ~ (3-20), and transforming them into the (η, ξ) coordinate system, the following expressions can be derived

$$\begin{aligned} &\frac{1}{\mathrm{Re}} \frac{2\mu}{\sqrt{g^{11}}} \left[g^{11} \frac{\partial}{\partial \eta} \left(n_r u + n_z v \right) + g^{12} \frac{\partial}{\partial \xi} \left(n_r u + n_z v \right) - B^n u - C^n v \right] \\ &\qquad = p_g + \frac{1}{\mathrm{Re}\, Ca} \zeta \kappa \end{aligned} \tag{D-16}$$

$$g^{11} \frac{\partial}{\partial \eta} \left(- n_z u + n_r v \right) + g^{12} \frac{\partial}{\partial \xi} \left(- n_z u + n_r v \right) + G \frac{\partial}{\partial \xi} \left(n_r u + n_z v \right) - B^t u - C^t v = 0 \tag{D-17}$$

$$\frac{-k}{\sqrt{g^{11}}} \left(g^{11} \frac{\partial T}{\partial \eta} + g^{12} \frac{\partial T}{\partial \xi} \right) = \frac{1}{q_m} \left(q_{rad,opa} + q_{conv} \right) \tag{D-18}$$

where

$$B^n = g^{11} \frac{\partial}{\partial \eta} \left(n_r \right) + g^{12} \frac{\partial}{\partial \xi} \left(n_r \right), \tag{D-19}$$

$$C^n = g^{11} \frac{\partial}{\partial \eta} \left(n_z \right) + g^{12} \frac{\partial}{\partial \xi} \left(n_z \right), \tag{D-20}$$

$$B^t = g^{11} \frac{\partial}{\partial \eta} \left(- n_z \right) + g^{12} \frac{\partial}{\partial \xi} \left(- n_z \right) + G \frac{\partial}{\partial \xi} \left(n_r \right), \tag{D-21}$$

$$C^t = g^{11} \frac{\partial}{\partial \eta} \left(n_r \right) + g^{12} \frac{\partial}{\partial \xi} \left(n_r \right) + G \frac{\partial}{\partial \xi} \left(n_z \right) \tag{D-22}$$

D.2 Air Domain

The governing equations for the air domain given by Equation (3-13) ~ (3-16) are cast into the fully conservative form in a general curvilinear coordinate system (η, ξ) as follows:

$$\frac{\partial}{\partial \eta}\left(\frac{\rho U}{J}\right)+\frac{\partial}{\partial \xi}\left(\frac{\rho V}{J}\right)=S_p \tag{D-23}$$

$$\begin{aligned}\rho\left\{\frac{\partial}{\partial t}\left(\frac{u}{J}\right)+\frac{\partial}{\partial \eta}\left[\frac{(U+\eta_t)u}{J}\right]+\frac{\partial}{\partial \xi}\left[\frac{(V+\xi_t)u}{J}\right]\right\}=-\left[\frac{\partial}{\partial \eta}\left(\frac{\eta_r}{J}p\right)+\frac{\partial}{\partial \xi}\left(\frac{\xi_r}{J}p\right)\right]\\ +\Pr\left\{\frac{\partial}{\partial \eta}\left[\frac{\mu}{J}\left(g^{11}\frac{\partial u}{\partial \eta}+g^{12}\frac{\partial u}{\partial \xi}\right)\right]+\frac{\partial}{\partial \xi}\left[\frac{\mu}{J}\left(g^{12}\frac{\partial u}{\partial \eta}+g^{22}\frac{\partial u}{\partial \xi}\right)\right]\right\}+S_u\end{aligned} \tag{D-24}$$

$$\begin{aligned}\rho\left\{\frac{\partial}{\partial t}\left(\frac{v}{J}\right)+\frac{\partial}{\partial \eta}\left[\frac{(U+\eta_t)v}{J}\right]+\frac{\partial}{\partial \xi}\left[\frac{(V+\xi_t)v}{J}\right]\right\}=-\left[\frac{\partial}{\partial \eta}\left(\frac{\eta_z}{J}p\right)+\frac{\partial}{\partial \xi}\left(\frac{\xi_z}{J}p\right)\right]\\ +\Pr\left\{\frac{\partial}{\partial \eta}\left[\frac{\mu}{J}\left(g^{11}\frac{\partial v}{\partial \eta}+g^{12}\frac{\partial v}{\partial \xi}\right)\right]+\frac{\partial}{\partial \xi}\left[\frac{\mu}{J}\left(g^{12}\frac{\partial v}{\partial \eta}+g^{22}\frac{\partial v}{\partial \xi}\right)\right]\right\}+S_v\end{aligned} \tag{D-25}$$

$$\begin{aligned}&\rho C_p\left\{\frac{\partial}{\partial t}\left(\frac{T}{J}\right)+\frac{\partial}{\partial \eta}\left[\frac{(U+\eta_t)T}{J}\right]+\frac{\partial}{\partial \xi}\left[\frac{(V+\xi_t)T}{J}\right]\right\}=\\ &\frac{\partial}{\partial \eta}\left[\frac{k}{J}\left(g^{11}\frac{\partial T}{\partial \eta}+g^{12}\frac{\partial T}{\partial \xi}\right)\right]+\frac{\partial}{\partial \xi}\left[\frac{k}{J}\left(g^{12}\frac{\partial T}{\partial \eta}+g^{22}\frac{\partial T}{\partial \xi}\right)\right]+S_u\end{aligned} \tag{D-26}$$

where the source terms are given by

$$S_p=-\frac{1}{J}\left(\frac{\partial \rho}{\partial t}+\frac{\rho u}{r}\right) \tag{D-27}$$

$$S_u=\frac{\Pr}{J}\left[\left(\frac{\mu}{r}+\frac{\partial \mu}{\partial r}\right)\left(\eta_r\frac{\partial u}{\partial \eta}+\xi_r\frac{\partial u}{\partial \xi}\right)-\frac{\mu u}{r^2}+\frac{\partial \mu}{\partial z}\left(\eta_r\frac{\partial v}{\partial \eta}+\xi_r\frac{\partial v}{\partial \xi}\right)\right]-\frac{\rho u^2}{rJ} \tag{D-28}$$

$$S_v = \frac{\mathrm{Pr}}{J}\left[\frac{\partial \mu}{\partial r}\left(\eta_z \frac{\partial u}{\partial \eta} + \xi_z \frac{\partial u}{\partial \xi}\right) + \frac{\mu}{r}\left(\eta_r \frac{\partial v}{\partial \eta} + \xi_r \frac{\partial v}{\partial \xi}\right) + \frac{\partial \mu}{\partial z}\left(\eta_z \frac{\partial v}{\partial \eta} + \xi_z \frac{\partial v}{\partial \xi}\right)\right] - \frac{\rho u v}{rJ} + \frac{\rho}{JFr} \tag{D-29}$$

$$S_T = \frac{k}{rJ}\left(\eta_r \frac{\partial T}{\partial \eta} + \xi_r \frac{\partial T}{\partial \xi}\right) - \rho C_p \frac{uT}{rJ} \tag{D-30}$$

Note that in order to put the continuity equation in a standard form that is ready to apply the pressure correction algorithm which is presented in the Chapter III, the time derivative of density term is put in the source term.

REFERENCES

Baek, S.W. and Kim, M.Y., 1997, "Modification of the Discrete-Ordinates Method in an Axisymmetric Cylindrical Geometry," *Numerical Heat Transfer*, Part B, Vol. 31, pp. 313-326.

Baek, S.W. and M.Y. Kim, 1997, "Modification of the Discrete-Ordinates Method in an Axisymmetric Cylindrical Geometry," *Numerical Heat Transfer*, Part B, Vol. 31, pp. 313-326.

Baker, J. and P.D. Christofides, 2000, "Finite-dimensional approximation and control of non-linear parabolic PDE systems," *Int. J. Control*, Vol. 73, No. 5, pp439-456

Banerjee, S., J.V. Cole and K.F. Jensen, 1998, "Nonlinear Model Reduction of Rapid Thermal Processing Systems," *IEEE Transactions on Semiconductor Manufacturing*, Vol. 11, pp. 266-275.

Bansal, N.P. and Doremus, R.H., 1986, Handbook of Glass Properties, Academic Press, Inc., New York.

Bernstein, D.S. and W.M. Haddad, 1995, Control-System Synthesis: the Fixed-Structure Approach, Lecture notes for the Robust Control graduate course in Georgia Tech.

Carlson, B.G. and Lathrop, K.D., 1968, "Transport Theory - the Method of Discrete Ordinates," in Greenspan, H., Kelber, C.N., and Okrent, D. (Eds.), *Computing Methods in Reactor Physics*, pp. 165-266, Gordon & Breach, New York.

Chai, J.C., H.S. Lee and S.V. Patankar, 1994, "Finite Volume Method for Radiative Heat Transfer," *J. of Thermophysics and Heat Transfer*, Vol. 8, No. 3, pp. 419-425.

Cheng, X. and Jaluria, Y., 2002, "Effect of Draw Furnace Geometry on High-Speed Optical Fiber Manufacturing," *Numerical Heat Transfer*, Part A, Vol. 41, pp. 757-781.

Chorin, A.J., 1967, "A Numerical Method for Solving Incompressible Viscous Flow Problems," J. Comput. Phys., Vol. 2.

Choudhury, S. R., Jaluria, Y., and Lee, S. H.-K., 1999, "A Computational Method for Generating the Free-surface Neck-down Profile for Glass Flow in Optical Fiber Drawing," *Numerical Heat Transfer*, Part A, Vol. 35, pp. 1-24.

Choudhury, S.R. and Y. Jaluria, 1998, "Thermal Transport Due to Material and Gas Flow in a Furnace for Drawing an Optical Fiber," *J. Mater. Res.*, Vol. 13, No. 2, pp. 494-503.

Donnelly, G.J. and Weinberger, C.B., 1975, "Stability of Isothermal Fiber Spinning of a Newtonian Fluid," *Ind. Eng. Chemistry Fund.*, Vol. 14, No. 4, pp. 334-337.

Egan, W.G. and Hilgeman, T.W., 1979, "Optical Properties of inhomogeneous materials: applications to geology, astronomy, chemistry and engineering, " Academic Press, New York.

Endrys, Jiri, 1999, "Measurement of Radiative and Effective Thermal Conductivity of Glass," *Proc. of the 5th ESG Conf.*, A5 10-17.

Endrys, Jiri, 1999, "Measurement of Radiative and Effective Thermal Conductivity of Glass, " *Proc. of the 5th ESG Conf.*, A5 10-17.

Fleming, J.D., 1964, "Fused Silica Manual," Final Report for the U.S. Atomic Energy Commission, Oak Ridge, Tennessee, Project No. B-153.

Fletcher, C.A.J., 1984, *Computational Galerkin Methods*, New York: Springer-Verlag.

Garner, H., 2000, "An Experimental Procedure for Measuring Furnace Temperature Profiles in Optical Fiber Drawing," Bell Labs/Optic Fiber Solutions, Internal Report.

Geyling, F.T. and G.M. Homsy, 1980, "Extensional Instabilities of the Glass Fiber Drawing Process," *Glass Technology*, Vol. 21, No. 2, pp. 95-102.

Homsy, G. M. and Walker, K., 1979, "Heat Transfer in Laser Drawing of Optical Fibers," *Glass Technology,* Vol. 20, No. 1, pp. 20-26.

Imoto, K., M. Sumi, G. Toda and T. Suganuma, 1989, "Optical Fiber Drawing Method with Gas Flow Controlling System," *J. Lightwave Technol.*, Vol. 7, pp. 115-121.

Issa, R.I., 1985, "Solution of the Implicitly Discretized Fluid Flow Equations by Operator-Splitting," *Journal of Computational Physics*, Vol. 62, pp. 40-65.

Jamaluddin, A. S. and Smith, P. J., 1988, "Predicting Radiative Transfer in Axisymmetric Cylindrical Enclosures Using the Discrete Ordinates Method, " *Combust. Sci. and Tech.*, Vol. 62, pp. 173-186.

Kesten, A.S., 1968, "Radiant heat flux distribution in a cylindrically-symmetric nonisothermal gas with temperature-dependent absorption coefficient," *J. Quant. Spectrosc. Radiat. Transfer*., Vol. 8, pp. 419-434.

Lee, K. H. and Viskanta, R., 1997, "Prediction of Spectral Radiative Transfer in A Condensed Cylindrical Medium Using Discrete Ordinates Method, " *J. Quant. Spectrosc. Radiat. Transfer,* Vol. 58, pp. 329-345.

Lee, K. H. and Viskanta, R., 1999, "Comparison of the diffusion approximation and the discrete ordinates method for the investigation of heat transfer in glass," *Glass Science and Technology-Glastechnische Berichte*, Vol 72, No. 8, pp. 254-265.

Lee, K.-M., and Z. Zhou, 1997, "Modeling and Optimal Control of High-Speed High-Strength Precision Optical Fibers Drawing, " Proposal to Lucent Technologies.

Lee, S.H.-K. and Jaluria Y., 1997, "Simulation of the Transport Processes in the Neck-Down Region of a Furnace Drawn Optical Fiber," *Int. J. Heat Mass Transfer*, Vol. 40, pp. 843-856.

Liu, J., H.M. Shang and Y. S. Chen, "Prediction of Radiative transfer in General Body-Fitted Coordinates," *Numerical Heat Transfer*, Vol. 31, Part B, pp. 423-439, 1997.

Lueptow, R.M. and Leehey, P., 1986, "The Eddy Viscosity in a Turbulent Boundary Layer on a Cylinder," *Physics of Fluids*, Vol. 29(12), pp. 4232-4233.

Lueptow, R.M., Leehey, P., and Stellinger, T., 1985, "The Thick, Turbulent Boundary Layer on a Cylinder: Mean and Fluctuation Velocities," *Physics of Fluids*, Vol. 28(12), pp. 3495-3505.

Matovich, M.A. and Pearson, J.R.A., 1969, "Spinning a Molten Threadline," *Ind. Eng. Chemistry Fund.*, Vol. 8, No. 3, pp. 512-520.

Mhaskar, R.D. and Shah, Y.T., 1977, "Stability Analysis of Glass Fiber Spinning," *Glass Technology*, Vol. 18, pp.152-158.

Modest, M. F., 1993, Radiative Heat Transfer, McGraw-Hill, NY.

Mulpur, A. and C. Thompson, 1993, "Modal diameter control of Linear Isothermal Optical Fibers," in *Proc. 2nd IEEE Conf. Contr. Appl.,* Vancouver, Canada, pp. 433-438.

Mulpur, A. and C. Thompson, 1996, "Nonlinear Control of Optical Fiber Diameter Variations," *IEEE Tran. On Control Systems Technology*, Vol. 4, No. 2, pp. 152-162.

Myers, M. R., 1989, "A Model for Unsteady Analysis of Preform Drawing," *AIChE Journal,* Vol. 35, No. 4, pp. 592-602.

Nakahara, M., S. Sakagauchi and T. Miyashita, 1978, *Rev. Electr. Commun. Lab.,* Vol. 26, pp. 476-483.

Nijnatten, P. A. and Broekhuijse, J. T., 1999, "A High-Temperature Optical Test Facility for Determining the Absorption of Glass at Melting Temperatures," *Proc. of the 5th ESG Conf.*, A5 51-58.

Nijnatten, P. A. and Broekhuijse, J. T., 1999, "A High-Temperature Optical Test Facility for Determining the Absorption of Glass at Melting Temperatures, " *Proc. of the 5th ESG Conf.*, A5 51-58.

Nijnatten, P. A., Broekhuijse J. T. and Faber, A. J., 1999, "Spectral Photon Conductivity of Glass at Forming and Melting Temperatures," *Proceedings of the 5th ESG Conference*, A5 2-9.

Nijnatten, P. A., Broekhuijse, J. T. and Faber, A. J., 1999, "Spectral Photon Conductivity of Glass at Forming and Melting Temperatures, " *Proceedings of the 5th ESG Conference,* A5 2-9.

Paek, U. C., and Runk, R. B., 1978, "Physical Behavior of the Neck-Down Region during Furnace Drawing of Silica Fibers," *Journal of Applied Physics*, Vol. 49, pp. 4417-4422.

Paek, U. C., and Runk, R. B., 1978, "Physical Behavior of the Neck-Down Region during Furnace Drawing of Silica Fibers," *Journal of Applied Physics*, Vol. 49, pp. 4417-4422.

Park, H.M. and Cho, D.H., 1996, "The Use of the Karhunen-Loeve Decomposition for the Modeling of Distributed Parameter Systems," *Chem. Eng. Sci.*, Vol. 51, pp. 81-98.

Park, H.M. and Lee, M.W., 2000, "Boundary Control of the Navier-Stokes Equation by Empirical Reduction of Modes," *Comput. Methods Appl. Mech. Engrg.*, Vol. 188, pp. 165-186.

Patankar, S.V., *Numerical Heat Transfer and Fluid Flow*, Taylor & Francis, 1980.

Pearson, J.R.A., Shah, Y.T., and Mhaskar, R.D., "On the Stability of Fiber Spinning of Freezing Fluids," *Ind. Eng. Chem. Fund.*, Vol. 15, pp.31-37.

Schlichting, H. and Gersten, K., 2000, *Boundary Layer Theory*, 8th Edition, New York: Springer-Verlag.

Schultz, W.W., A.F. Zebib, S.H. Davis and Y. Lee, 1984, "Nonlinear Stability of Newtonian Fibers," *J. Fluid Mechanics*, Vol. 149, pp. 455-475.

Shyy, W., Computational Modeling for Fluid Flow and Interfacial Transport, Amsterdam, New York : Elsevier, 1994.

Sirovich, L. and Park, H., 1990, "Turbulent Thermal Convection in a Finite Domain, Part I: Theory," *Physics of Fluids A*, Vol. 2, pp. 1649-1658.

Sirovich, L., 1987, "Turbulence and the Dynamics of Coherent Structures," Parts I-III, *Quart. Appl. Math*., XLV(3), 561-571, 573-582, 583-590.

Smithgall, D.H., 1979, "Application of Optimization Theory to the Control of Optical Fiber Drawing Process," *The Bell System Technical Journal*, Vol. 58, No. 6, pp. 1425-1435.

Tchikanda, S. and K.M. Lee, 2002, "State Space Modeling of Optical Fiber Drawing Process," *Proc. of 2002 ACC*, May 8-10, Anchorage, Alaska.

Tchikanda, S.W., 2001, *Modeling for High-Speed High-Strength Precision Optical Fiber Drawing*, Ph. D. Thesis, Georgia Institute of Technology.

Temam, R., 1988, Infinite-Dimensional Dynamical Systems in Mechanics and Physics, Springer-Verlag, New York.

Theodoropoulou, A., R.A. Adomaitis and E. Zafiriou, 1998, "Model Reduction for Optimization of Rapid Thermal Chemical Vapor Deposition System," *IEEE Transactions on Semiconductor Manufacturing*, Vol. 11, pp. 85-98.

Touloukian, Y.S., DeWitt, D.P. and Hernicz, R.S. (eds.): Thermal Radiative Properties: Nonmetallic Solids, Vol. 8 (pp. 1569-1576) of Thermophysical Properties of Matter, Plenum Press, New York, 1973.

Van Driest, E.R., 1956, "On Turbulent Flow Near a Wall," *Journal of Aeronautical Science*, Vol. 23, pp. 1007-1011.

Vasiljev, V.N., Dulnev, G.N. and Naumchic, V.D. 1989, "the Flow of a Highly Viscous Liquid with a Free Surface," *Glass Technology,* Vol. 30, No. 2, pp. 83-90.

Viskanta, R., and Anderson, E.E., 1975, "Heat transfer in Semitransparent Solids," *Advances in Heat Transfer*, Vol. 11, pp.317-441.

Yin, Z. and Jaluria, Y., 1997, "Zonal Method to Model Radiative Transfer in an Optical Fiber Drawing Furnace, " *Journal of Heat Transfer*, Vol. 119, pp. 597-603.

Yin, Z. and Jaluria, Y., 2000, "Neck Down and Thermally Induced Defects in High-Speed Optical Fiber Drawing," *Journal of Heat Transfer*, Vol. 122, pp. 351-362.